Synthesis and Characterization of Water-Soluble Silicon Quantum Dots for Photothermal Therapy and Fluorescence Imaging of Cancer Cells

がん細胞の蛍光イメージングと光温熱治療を指向した
水溶性シリコン量子ドットの合成と分析

İrem Nur Gamze ÖZBİLGİN

Graduate School of Chemical Sciences and Engineering
Hokkaido University
2022

Table of Contents

Table of Figures

List of Tables

Abstract

Quantum dots (QDs) are seen as a strong candidate as theranostic agents, which require to perform simultaneous imaging and therapy, due to their efficient interaction with incident excitations. Current QDs for theranostic applications have some challenges especially by means of toxicity. Silicon QDs (SiQDs), on the other hand, are intrinsically non-toxic thus they are promising candidate for bioapplications. So far, utilization of SiQDs were mostly focused on its photophysical properties. Whereas, controlling the nonradiative incidents in the structure remain scarce. In this work, we aim to investigate the use of SiQDs for theranostic applications. For this purpose, we conducted set of experiments to understand the mechanism of its photothermal response, its optical and photothermal properties in vitro.

Chapter 1 includes introductory information on target application area, theranostics and requirements for this field were addressed. Together with this, basic understanding to SiQDs were introduced Finally, current situation of quantum dots as fluorescence guided photothermal therapy and recent developments in SiQDs as theranostic agents were explained.

In Chapter 2, synthesis of stable, water soluble SiQDs that was used for these experiments was explained. Water-soluble SiQDs were prepared by thermal hydrosilylation of 10-undecenoic acid on their hydrogen-terminated surfaces, which are provided by thermal disproportionation of triethoxysilane hydrolyzed and subsequent hydrofluoric etching. SiQDs were characterized in terms of XRD, FTIR, TGA, zeta potential, UV-visible absorption, PL and PLQY. Prepared SiQDs were observed to have good surface properties also evidenced by enabling preparation of clear solutions up to 4 mg/mL. The 10-undecanoic acid functionalized SiQDs showed a long-term photostability when compared to commercial staining dye DAPI. Synthesis parameters were examined based on the PLQY and PL peak position values. It was seen that water soluble SiQDs with good PLQY could be obtained by at least 45minutes of hydrosilylation and 160 °C. Findings from this chapter will contribute to the realization of stable water soluble SiQDs which is one of the main challenges for bioapplications.

In Chapter 3, photothermal effect of freestanding SiQDs were investigated. Hydrogen terminated SiQDs were prepared so as to be in three different sizes under Bohr exciton radius. Photothermal response was measured by irradiation of SiQDs with 532 nm Raman laser at three different powers. In Raman laser experiments, temperature of large sized QDs could be increased up to the temperatures as high as 275 °C. This behavior is correlated with increasing defect amount in the structure of larger particles. To explain defects structure of each SiQD, temperature dependent photoluminescence (PL) spectroscopy was conducted. 10-fold, 70-fold and 440-fold PL intensity decrease for small, medium and large particle size, respectively, was observed by increasing temperature. This behavior is due to the amount of nonradiative channels increased with increasing particle size. Calculated activation energies by Arrhenius plots show decreasing trend with increasing particle size which implies the presence of high density of defect states for large particles. Exciton-phonon interaction in the structure was examined by corresponding from temperature dependent broadening of peak linewidths were fitted by Bose-Einstein equation. Results show that exciton-phonon coupling increased with particle size which may lead photothermal heating. It is concluded that temperature of SiQDs can be strictly controlled by particle size and tuning the laser power. This behaviour of SiQDs could be used for bioapplications where local heating in nanoscale is crucial.

In Chapter 4, photothermal performance of SiQD aqueous solutions were evaluated by calculating their photothermal conversion efficiencies. Photothermal conversion efficiency of SiQDs were seen to be size dependent, for instance, 25.6% and 37.1% for small and large particles, respectively, as confirmed by previous chapter. Obtained photothermal conversion efficiencies were comparable with counterpart materials for photothermal therapy applications. Furthermore, laser irradiation of HeLa cells with 50 and 400 μg/mL SiQDs were demonstrated and cell death depending on concentration was provided. It is concluded that water soluble SiQDs are potential candidates for theranostics with their good optical properties enabling imaging for more than 18 days and photothermal response having 25.6 % photothermal conversion efficiency together with the direct evidence on cell death by laser irradiation.

In Chapter 5, interaction of water soluble SiQDs with live cells were investigated by using HeLa cell lines. Confocal microscopy analyses showed successful uptake of SiQDs by cell lines. Also, long term imaging studies show that SiQDs can be traced in HeLa cells for more than 18 days. Then, short term and long-term cytotoxic effects of water soluble SiQDs were investigated. No significant toxicity was observed for 1 day experiments up to 400 μg/mL. In the long term, cytotoxicity of SiQDs were at acceptable level for 14 days incubation of 50 μg/mL SiQD concentration. It was seen that prepared SiQDs have sufficient properties for bioimaging with low toxicity.

In Chapter 6, overall summary of this work was presented. This thesis conducted a systematic study on applicability of SiQDs as theranostic biomarkers. This thesis reveals the utilization of photonic and phononic properties of SiQDs, together with investigating their long term stability in practical use. Deeper understanding on the photothermal heating mechanism was investigated. Furthermore, photothermal heating of aqueous SiQDs was performed and effectiveness of their photothermal response was demonstrated in vitro. With the findings of this thesis, merits for using SiQDs as theranostic agents were highlighted.

Chapter 1: Introduction

1.1. Quantum Dots

Confinement of electrons have shown noticeable effects when the diameter of nanostructure is comparable to the electron wavefunction wavelength. In such case, confining dimension is very strict and electron behaves like a free particle among the energy spectrum that starts to dissociate. Therefore, bandgap becomes size dependent (Figure 1.1). Semiconductor QDs are the nanostructures that aforementioned phenomenon could be observed by characterization techniques or even naked eye. They are oftenly called "artificial atoms" although they consist of 10^3 to 10^5 atoms, corresponding to the 1-10 nm size range.[1]

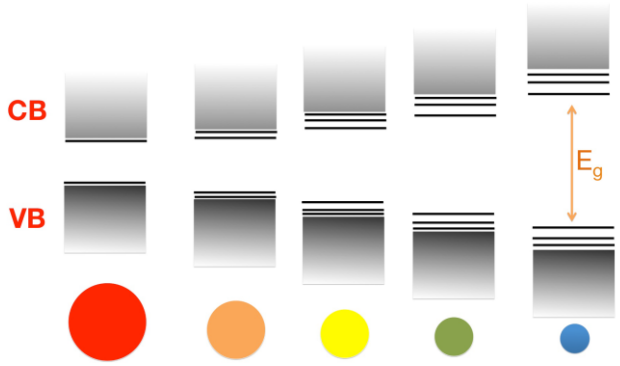

Figure 1.1. Size depended bandgap change in QDs[2]

Size dependent behavior is observed if only the radius of a QD becomes smaller than or close to the Bohr exciton radius, r_B. This behavior is explained by following equation[3]:

$$r_B = \frac{4\pi\varepsilon_0\varepsilon_r\hbar^2}{e^2 m_0}\left(\frac{1}{m_e^*}+\frac{1}{m_h^*}\right) \qquad \textbf{(1.1)}$$

where ε_0 and ε_r are the permittivity of vacuum and the relative dielectric constant of the semiconductor, respectively. $\hbar = h/(2\pi - h)$ is the Planck's constant, e is the electron charge, m_0 is the electron mass, and m_e^* and m_h^* are the electron and hole relative effective masses, respectively.

Due to their electronic structure, they show high photoluminescence quantum yield (PLQY, indicator of the radiative recombination rate by the ratio of emitted atoms to the

absorbed atoms) and size dependent photoemission properties which have led them extend the application areas of semiconductor materials. QDs allow wide variety of surface functionalizations.

1.2. Quantum Dots for Cancer Therapy and Diagnosis

Being one of the most common reasons of human death, cancer related studies are needed to be performed not only by medicine-based field but also by physics, chemistry and materials science to understand and find better solutions for its diagnosis and treatment. Current treatment for cancer includes surgery, chemotherapy, radiotherapy and immunotherapy are often considered as causing broad collateral damage and many side effects.[4] For instance, to fully eliminate cancer cells, chemotherapy and radiotherapy are usually required after surgery which effects the life quality of the patient. In chemotherapy, used drugs may affect other healthy organs due to lack of tumor specificity. When compared with chemotherapy, radiotherapy is more local but it still gives damage to the healthy tissue on which it is applied and may cause radiodermatitis. Therefore, design of new strategies to treat cancer without/no healthy tissue damage has become a very essential topic for the last decades.[5]

Photothermal therapy (PTT) is one of the newly developing strategies that treats/contributes to the treatment of cancer by hyperthermia. It is considered as an effective technique where drugs for chemotherapy is not efficiently delivered due to the low vascular structure of the tumors and detrimental effects of radiotherapy.[6]

Depending on the temperature range, increasing temperature may decelerate, deactivate or deteriorate the cells (Figure 1.2). In diathermia range (37-41 °C), there is no change in cellular level, this range is used in physiotherapies for muscle relaxing and pain relief.[7] Between 48-60 °C, irreversible damage to the cells may provide death of cancer cells. However, there is no selectivity in this range, meaning that healthy tissue is also damaged.[7] Whereas, hyperthermia range (41-48 °C) is considered ideal for cancer treatment by different aspects. First, cancer cells may be deactivated and they may become sensitive to radiation and chemotherapy.[8] On the other hand, irreversible damage could be done under certain

parameters like long exposures.[6] Also, reports on hyperthermia studies performed between 45-48 C show rapid cell death.[9-11]

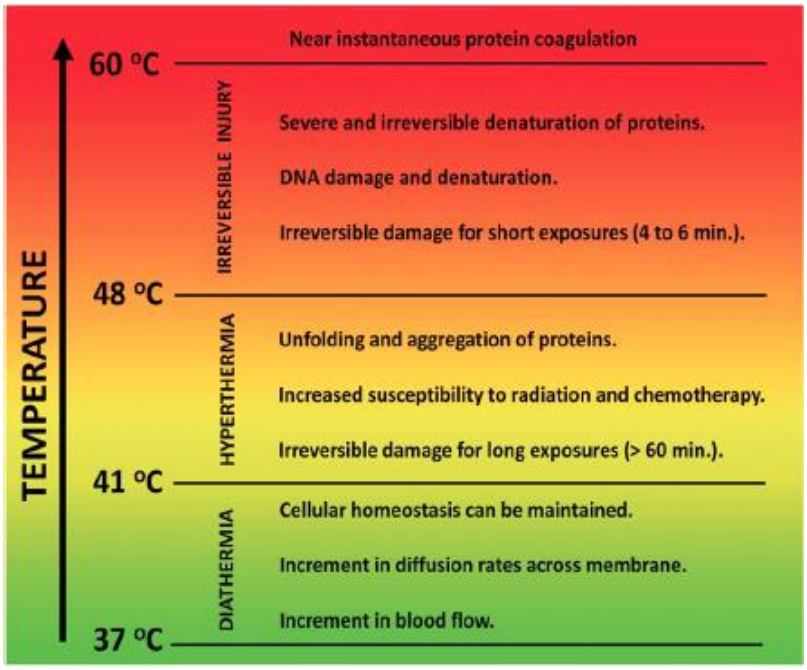

Figure 1.2. Effects of increasing temperature in cellular level[6]

Here, the most crucial requirement to minimize damage is to localize heat strictly to the tumor area. While doing this, low laser light intensities should be used to reduce undesired light absorption by healthy tissue. For bioapplications, available laser wavelengths are defined considering the absorption, emission and scattering occurred by bodily fluids and tissues. First and second biological windows are spectral ranges where tissues are transparent when compared to UV and visible light (Figure 1.3a,b). In second biological window which corresponds to NIR-II region, imaging/treatment with could be achieved not only by deepest tissue penetration (Figure 1.3c), but also with suppressed autofluorescence. Since most of the available nanostructures absorb light up to NIR-I region, new technologies like two-photon imaging also have very exciting outcomes to utilize these particles for effective imaging/treatment with deep tissue penetration.[11]

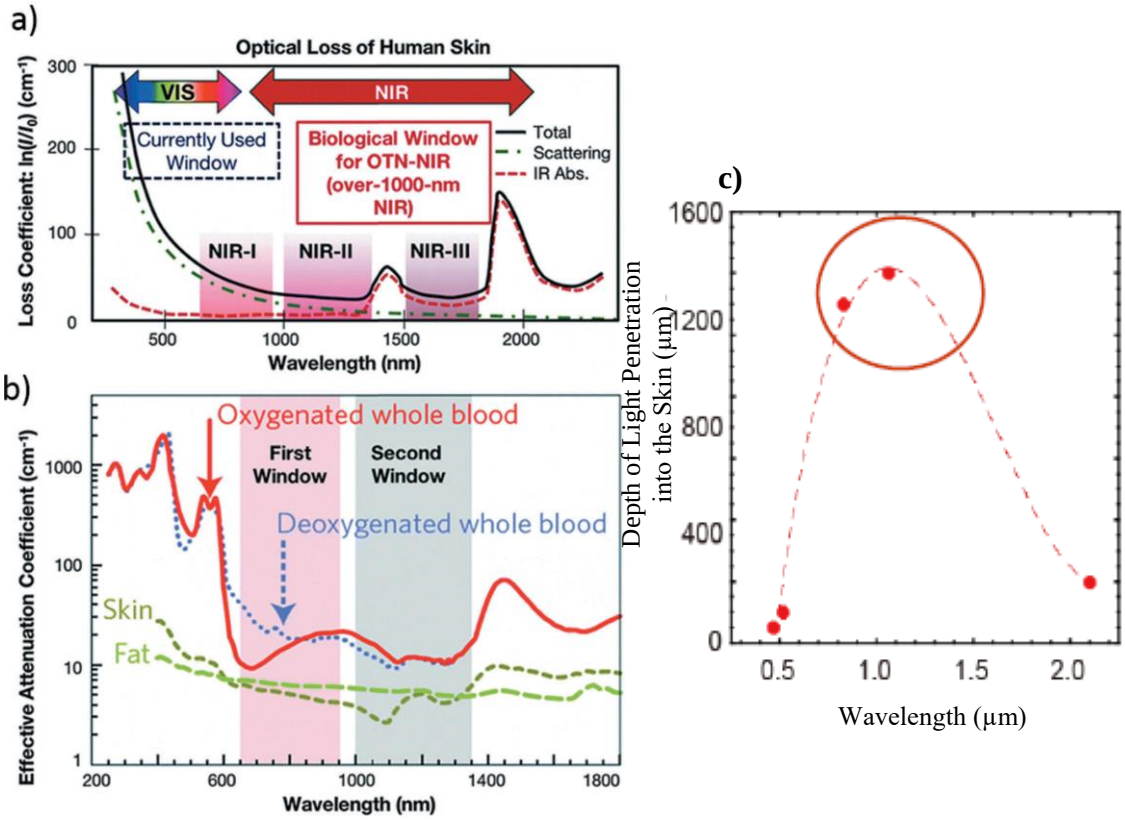

Figure 1.3. a) Human skin absorption spectra in the of NIR-I, NIR-II, and NIR-III regions. b) Absorption and scattering spectra from oxygenated blood, deoxygenated blood, skin, and fatty tissue,[12] c) wavelength dependent light penetration to human skin

For bioimaging, currently used fluorescence dyes suffer from drawbacks such as instability and photobleaching, emission in visible region which autofluorescence occurs, being easily affected by environmental conditions, narrow excitation range, broad emission spectra with a long tail in red wavelength region. On the other hand, with large absorption coefficient, size tunable emission, high PLQYs, photostability and resistance to photobleaching, broad excitation with narrow emission peaks, QDs are excellent candidates for bioimaging.[13]

Recent development in bioimaging techniques have emerged the concept of theranostics that has been interest of intense research due to realization of simultaneous diagnosis and treatment of cancer tissues in a time saving manner.[14] Therapeutic agents in

this field are expected to have excellent optical properties that enable usage of non-invasive imaging techniques such as fluorescence and two-photon imaging together with drug delivery,[15] treatment of the tumors by their ability to interact with photons,[16] and/or magnetic field.[17,18] This requirement makes semiconductor QDs promising candidates due to their excellent optical and electrical properties, diverse possibility for surface functionalization, size tunability and photostability.[19] Furthermore, size is also an important factor for designing such agent. Using small size (1-10 nm) is desired due to being compatible with biomolecule's mobility and ability to interact with its environment[20] and it was also shown that QDs with hydrodynamic diameter smaller than 5.5 nm could rapidly undergo renal clearance[21] while using larger sizes (>20 nm) provides photophysical properties higher resolution and accuracy. Therefore, QDs with enhanced photophysical properties would be ideal agents for bioimaging and therapy. Overall comparision of QDs with organic dye counterparts is given in Table 1.1.[22]

Table 1.1. Comparision of QDs with organic counterparts

Property	**QDs**	**Organic dyes**
Size	Tunable (2-10 nm)	<0.5 nm
Absorption Spectra	Broad	Narrow
Emission Spectra	Narrow	Broad
PLQY	High (Vis: 0.8, NIR: 0.7 max)	Low (Vis: 1.0, NIR: 0.25 max)
Fluorescence Excited State Lifetime	Long (10 to 100 nanoseconds with multi-exponential decay)	Short (< 10 nanoseconds with mono-exponential decay)
Two-photon Cross Section	Large (typically 0.2 to 5 $\times 10^{-46}$ cm^4 sec $photon^{-1}$)	Small(1×10^{-49} cm^4 sec $photon^{-1}$)
Detection Sensitivity	High	Low
Resistance to Photobleaching	High	Low
Tissue Penetration Depth	Medium (size dependent)	High
Toxicity		
Key Strengths	Ease of spectra tunability	Typically stable, water soluble materials
	Quantum yield (up to 100 times brighter)	Ease of bioconjugation
	High photostability	Deep tissue penetration
Key Challenges	Potential toxicity *in vivo*	Lack of tunability
	Poor aqueous solubility and stability	Prone to photo-bleaching

Nanostructures that can be used for therapy and imaging of cancer must have following main properties:

- They must be smaller than 100 nm to allow long circulating times and effective incorporation with the cells.
- They must be stable and dispersible in biocompatible fluids.
- They must have low toxicity during and after treatment.
- For phototherapy, they must efficiently produce heat when excited externally.

Considering these properties, QDs are very attractive due to their potential to provide these properties by fulfilling following requirements:

- High absorption or two-photon cross section properties for first and second biological windows: Design of a QD meets this requirement will provide efficient absorption of incident laser thus efficient light to light and/or light to heat conversion.
- Easy functionalization: Since QDs allow functionalization in a wide range, it has become a big advantage for cancer therapy and diagnosis application by means of effective selectivity. Also, good solubility via proper functionalization will provide easy circulation in the bloodstream.
- Low toxicity: To ensure minimum side effects, QDs must be non-toxic and/or have very low toxicity. Furthermore, it is ideal that QDs show toxic effect only when irradiated by laser. Due to their excellent optical properties and working in the biological windows, QDs containing toxic elements are studied so as to decrease their toxic effects, on the other hand, there are non-toxic options that have potential to use as agents for cancer diagnosis and therapy.

1.2.1. Current Situation of Quantum Dots for Fluorescence Imaging and Photothermal Therapy

With their superior properties over organic counterparts, QDs as bioimaging agents have been an intense focus of work. Currently reported QDs having potential for bioimaging applications due to their PLQY approaching to unity are summarized depending on their emission wavelength range in Figure 1.1. Especially in the range corresponds to NIR-II

window, candidate QDs include inherently toxic elements. Achievable emission range by SiQDs that can cover NIR-I and NIR-II Windows are also shown on Figure 1/4 with dashed lines.

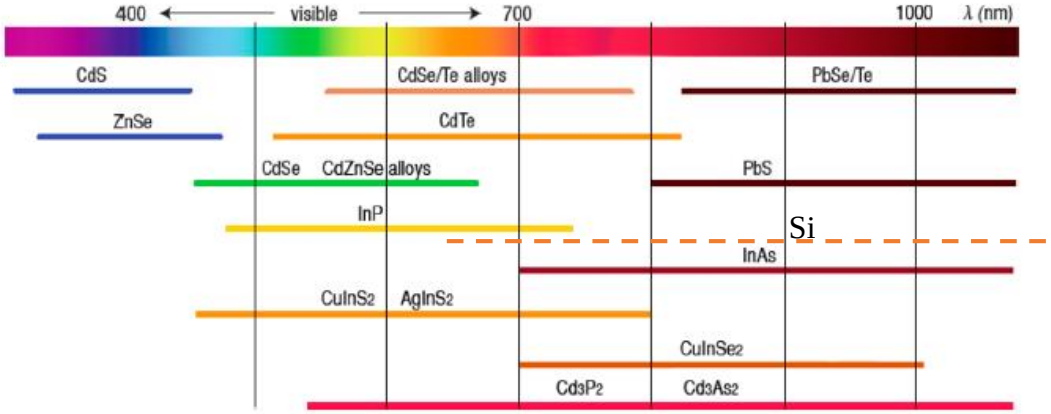

Figure 1.4. Spectral range of emission for the most widely studied types of semiconductor NCs[1]

Among the QDs, so far, research on applicability of QDs on theranostics is reported for CdSe/ZnS,[23] CuInS/ZnS,[24] $CuInS_2$,[25] PbSe,[26] InP,[27] and graphene.[28] In particular, PbSe QDs are attractive due to their strong photoemission with narrow peak in near-infrared (NIR) region. Whereas, there are concerns on their toxicity, photostability and long-term cytotoxicity. Table 1.2 shows the example QDs for bioapplications together with size and PLQY values. For QD size range, number of studies is limited by means of photothermal therapy. Also, intrinsically nontoxic quantum dots in this field still remains unexplored.

Table 1.2. QDs for bioapplications

QDs	Size (nm)	PLQY (%)	Bioimaging	PTT	Ref
CdTe	10	15-20	✓		5
	3		✓	✓	11
CdS	2-5		✓		13
PbS	3.5	26	✓		3
	7.5	8	✓		8
PbS/CdS	17.1		✓		10
$CuInS_2$/ZnS		30*	✓		9
Ag_2S	5.4	15.5	✓		4
Si	2-8	5-10	✓		29
C	2-5	6	✓		2
	25	5		✓	7

1.3. Silicon

1.3.1. Crystal structure of Silicon

Silicon is Group IV semiconductor element with 14 atomic number. It has diamond cubic crystal structure with a=0.543 nm where a is the edge of the conventional cubic cell. This structure can also be defined as two face centered cubic sublattices interpenetrating with $a\sqrt{3}/4$ displacement. Therefore, the two sets of atoms in sublattices are different from each other by means of crystal structure point of view, specifically, if a corner atom has one neighboring atom in one diagonal direction, it does not have this neighboring atom in reverse direction. From another aspect, unit cell of diamond cubic structure of Si contains a tetrahedron of which each atom has four equidistant neighboring atoms that lie on the corners (Figure 1.5).[30]

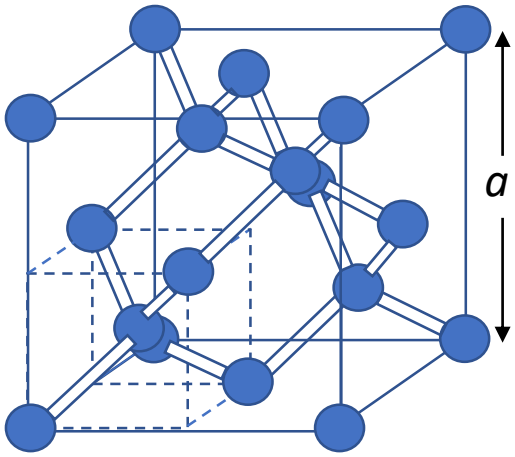

Figure 1.5. Crystal structure of Si[30]

1.3.2. Bandstructure of Silicon

Si has 14 electrons with $1s^2 2s^2 2p^6 3s^2 3p^2$ electron shell configuration. As a Group IV element, the 3rd energy level of Si is only filled with 4 electrons (conduction band), meaning that 4 orbitals with high energy level remains empty, forming the conduction band. Under specific circumstances, electrons in valance band could be excited to upper energy level, forming excitons, then excited electron may go back to lower energy band and emit light (radiative recombination) at the bandgap size of Si, which is Eg=1.12 eV at T=300 K.

Si is an indirect bandgap element. For radiative recombination in such band structure, phonon absorption or emission is required in order to preserve crystal momentum (Figure 1.2a). With the decrease of size, free carriers are confined in a quantum structure due to the limitation by Heisenberg's uncertainty principle. Position of free carriers are not defined precisely, meaning that wavefunction of free carriers are broadened (Figure 1.6). This behavior increases the possibility to recombine without loss as phonons. Thus, Si behaves as direct bandgap semiconductor at sufficiently small particle sizes.

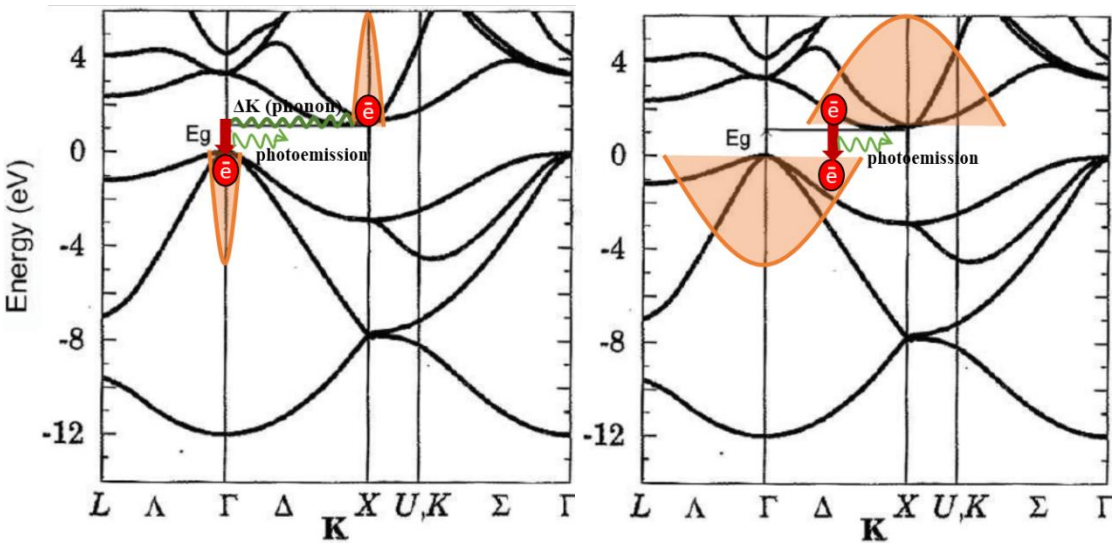

Figure 1.6. Bandgap structure of Si, radiative recombination of indirect bandgap Si in a) large sized and b) small size

1.3.3. Silicon Quantum Dots

Silicon Quantum Dots (SiQDs) have found their way in many application areas due to the substantial effect of quantum confinement that determines their properties such as PL and PLQY. Studies address tunability of its PL from visible to NIR range. PLQY of SiQDs can also be tailored by the engineering of radiative channels via surface modifications. For utilization, PLQY of QDs should be close to unity, for the case of SiQDs, highest PLQY achieved is 65-70%. Despite PLQY being close to unity, SiQDs are still attractive due to its versatility, abundancy, low toxicity and cost effectiveness.[31]

*1.3.3.1. **Phonons in Silicon Quantum Dots***

Making use of radiative processes in SiQDs have led to utilize them in a wide range of applications such as lasers, diodes, energy storage, photocatalysts, and so on. The less focused yet the more challenging side of the light-SiQD interaction is the nonradiative processes.

The photothermal effect refers to the ability to convert photon energy of light absorption into heat. Heat conversion is done by photoexcited nanostructrures can occur by different mechanisms depending on the material's nature.[32] For metallic nanoparticles, photothermal

conversion is explained by surface plasmon resonances. In this case, particle size and shape play decisive role on generation of surface plasmons providing heat should match with the excitation frequency of irradiating laser. For semiconductor nanostructures, photothermal conversion is explained by excess carriers undergone nonradiative recombination and it can be strengthened by maximizing the nonradiative decay rates and manipulating nonradiative channels.[33] Controlling the heat of the NPs expands their availability for applications such as phototheranostics,[33] fast evaporation,[34] optical printing,[35] and photocatalytic growth of semiconductor nanowires.[36, 37] Theoretical modeling to generate heat in a nanoscale area and subsequent heat conduction is established for quantum dots (QDs) of semiconductors,[38] but experimental control remains scarce.

For semiconductor nanostructures, heating mechanism for photothermal heat generation differs from metallic ones due to not having free electrons on the surface. Here, defects and trap sites in the band structure is responsible from photothermal heating, therefore, control of heat generation is mostly challenging. When light is irradiated on the semiconductor, electrons on the valance band goes to the valance band and create excitons are responsible from photoemission. Some of the excitons does not generate light and stay in the structure, especially on the conduction band. These nonradiative excitons diffuse to the places with a smaller number of excitons. During this movement, heat is generated. (Figure 1.7)

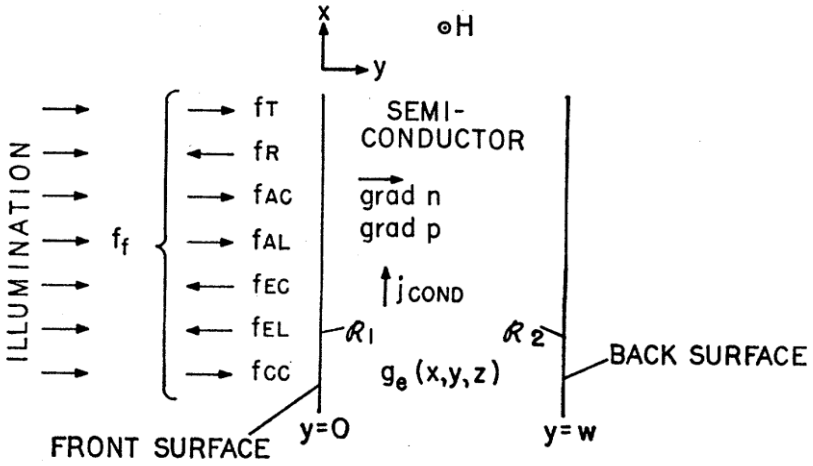

Figure 1.7. Analysis of photothermal effect[32]

1.4. Motivation: Silicon Quantum Dots as Theranostic Agents for Fluorescence Guided Photothermal Therapy

SiQDs are shown as potential candidates for bioimaging due to its optical properties, photostability and low toxicity.[39-41] On the other hand, SiQDs have photothermal response of which generated heat could be tuned by their size, together with conversion efficiency being comparable to their counterparts.[42, 43] These two aspects imply that SiQDs can be great alternative for theranostics by enabling imaging in second biological window and killing the cancer cells by hyperthermia. It is reported that porous Si can generate enough heat to kill cancer with producing less amount of reactive oxygen species when compared to their carbon nanotube counterparts.[44] Other studies have shown that using porous Si[45] and Si nanowires[46, 47] enhance photothermal performance of Au nanoparticles on the death of cancer cells in-vitro and in-vivo environments. There is still intensive work necessary for the realization of SiQDs as theranostic agents. Here, we aim to investigate realization of SiQDs with good photophysical properties so as to be used for bioimaging applications and controllable photothermal response for photothermal therapy applications.

1.5. References

(1) Chen, O.; Wei, H.; Maurice, A.; Bawendi, M.; Reiss, P. Pure colors from core–shell quantum dots. *MRS Bulletin* **2013**, *38* (9), 696-702. DOI: 10.1557/mrs.2013.179.

(2) Tao, H.; Yang, K.; Ma, Z.; Wan, J.; Zhang, Y.; Kang, Z.; Liu, Z. In vivo NIR fluorescence imaging, biodistribution, and toxicology of photoluminescent carbon dots produced from carbon nanotubes and graphite. *Small* **2012**, *8* (2), 281-290. DOI: 10.1002/smll.201101706.

(3) Nakane, Y.; Tsukasaki, Y.; Sakata, T.; Yasuda, H.; Jin, T. Aqueous synthesis of glutathione-coated PbS quantum dots with tunable emission for non-invasive fluorescence imaging in the second near-infrared biological window (1000–1400 nm). *Chemical Communications* **2013**, *49* (69), 7584-7586, 10.1039/C3CC44000A. DOI: 10.1039/C3CC44000A.

(4) Zhang, Y.; Hong, G.; Zhang, Y.; Chen, G.; Li, F.; Dai, H.; Wang, Q. Ag2S Quantum Dot: A Bright and Biocompatible Fluorescent Nanoprobe in the Second Near-Infrared Window. *ACS Nano* **2012**, *6* (5), 3695-3702. DOI: 10.1021/nn301218z.

(5) He, Y.; Zhong, Y.; Su, Y.; Lu, Y.; Jiang, Z.; Peng, F.; Xu, T.; Su, S.; Huang, Q.; Fan, C.; et al. Water-Dispersed Near-Infrared-Emitting Quantum Dots of Ultrasmall Sizes for In Vitro and In Vivo Imaging. *Angewandte Chemie International Edition* **2011**, *50* (25), 5695-5698. DOI: https://doi.org/10.1002/anie.201004398.

(6) Wang, J.; Liu, Y.; Peng, F.; Chen, C.; He, Y.; Ma, H.; Cao, L.; Sun, S. A General Route to Efficient Functionalization of Silicon Quantum Dots for High-Performance Fluorescent Probes. *Small* **2012**, *8* (15), 2430-2435. DOI: https://doi.org/10.1002/smll.201102627.

(7) Bai, Y.; Zhang, B.; Chen, L.; Lin, Z.; Zhang, X.; Ge, D.; Shi, W.; Sun, Y. Facile One-Pot Synthesis of Polydopamine Carbon Dots for Photothermal Therapy. *Nanoscale Res Lett* **2018**, *13* (1), 287-287. DOI: 10.1186/s11671-018-2711-2 PubMed.

(8) Imamura, Y.; Yamada, S.; Tsuboi, S.; Nakane, Y.; Tsukasaki, Y.; Komatsuzaki, A.; Jin, T. Near-Infrared Emitting PbS Quantum Dots for in Vivo Fluorescence Imaging of the Thrombotic State in Septic Mouse Brain. *Molecules* **2016**, *21* (8), 1080.

(9) Xie, R.; Rutherford, M.; Peng, X. Formation of High-Quality I−III−VI Semiconductor Nanocrystals by Tuning Relative Reactivity of Cationic Precursors. *Journal of the American Chemical Society* **2009**, *131* (15), 5691-5697. DOI: 10.1021/ja9005767.

(10) Tian, R.; Ma, H.; Zhu, S.; Lau, J.; Ma, R.; Liu, Y.; Lin, L.; Chandra, S.; Wang, S.; Zhu, X.; et al. Multiplexed NIR-II Probes for Lymph Node-Invaded Cancer Detection and Imaging-Guided Surgery. *Advanced Materials* **2020**, *32* (11), 1907365. DOI: https://doi.org/10.1002/adma.201907365.

(11) Chu, M.; Pan, X.; Zhang, D.; Wu, Q.; Peng, J.; Hai, W. The therapeutic efficacy of CdTe and CdSe quantum dots for photothermal cancer therapy. *Biomaterials* **2012**, *33* (29), 7071-7083. DOI: https://doi.org/10.1016/j.biomaterials.2012.06.062.

(12) Hemmer, E.; Benayas, A.; Légaré, F.; Vetrone, F. Exploiting the biological windows: current perspectives on fluorescent bioprobes emitting above 1000 nm. *Nanoscale Horizons* **2016**, *1* (3), 168-184, 10.1039/C5NH00073D. DOI: 10.1039/C5NH00073D.

(13) Shivaji, K.; Mani, S.; Ponmurugan, P.; De Castro, C. S.; Lloyd Davies, M.; Balasubramanian, M. G.; Pitchaimuthu, S. Green-Synthesis-Derived CdS Quantum Dots Using Tea Leaf Extract: Antimicrobial, Bioimaging, and Therapeutic Applications in Lung Cancer Cells. *ACS Applied Nano Materials* **2018**, *1* (4), 1683-1693. DOI: 10.1021/acsanm.8b00147.

(14) Evangelopoulos, M.; Parodi, A.; Martinez, J. O.; Tasciotti, E. Trends towards Biomimicry in Theranostics. *Nanomaterials* **2018**, *8* (9), 637.

(15) Muthu, M. S.; Leong, D. T.; Mei, L.; Feng, S.-S. Nanotheranostics ˗ Application and Further Development of Nanomedicine Strategies for Advanced Theranostics. *Theranostics* **2014**, *4* (6), 660-677, Review. DOI: 10.7150/thno.8698.

(16) Xu, G.; Zeng, S.; Zhang, B.; Swihart, M. T.; Yong, K.-T.; Prasad, P. N. New Generation Cadmium-Free Quantum Dots for Biophotonics and Nanomedicine. *Chemical Reviews* **2016**, *116* (19), 12234-12327. DOI: 10.1021/acs.chemrev.6b00290.

(17) Singh, S. P. Multifunctional Magnetic Quantum Dots for Cancer Theranostics. *Journal of Biomedical Nanotechnology* **2011**, *7* (1), 95-97. DOI: 10.1166/jbn.2011.1219.

(18) Mody, V. V.; Nounou, M. I.; Bikram, M. Novel nanomedicine-based MRI contrast agents for gynecological malignancies. *Advanced Drug Delivery Reviews* **2009**, *61* (10), 795-807. DOI: https://doi.org/10.1016/j.addr.2009.04.020.

(19) Montalti, M.; Cantelli, A.; Battistelli, G. Nanodiamonds and silicon quantum dots: ultrastable and biocompatible luminescent nanoprobes for long-term bioimaging. *Chemical Society Reviews* **2015**, *44* (14), 4853-4921, 10.1039/C4CS00486H. DOI: 10.1039/C4CS00486H.

(20) Valenta, J.; Greben, M.; Remeš, Z.; Gutsch, S.; Hiller, D.; Zacharias, M. Determination of absorption cross-section of Si nanocrystals by two independent methods based on either absorption or luminescence. *Applied Physics Letters* **2016**, *108* (2), 023102. DOI: 10.1063/1.4939699.

(21) Kim, M.; Lee, J.-H.; Nam, J.-M. Plasmonic Photothermal Nanoparticles for Biomedical Applications. *Advanced Science* **2019**, *6* (17), 1900471. DOI: https://doi.org/10.1002/advs.201900471.

(22) Wagner, A. M.; Knipe, J. M.; Orive, G.; Peppas, N. A. Quantum dots in biomedical applications. *Acta biomaterialia* **2019**, *94*, 44-63. DOI: 10.1016/j.actbio.2019.05.022 From Nlm.

(23) Dey, N. S. Quantum Dot: Novel Carrier for Drug Delivery. 2011.

(24) Lv, G.; Guo, W.; Zhang, W.; Zhang, T.; Li, S.; Chen, S.; Eltahan, A. S.; Wang, D.; Wang, Y.; Zhang, J.; et al. Near-Infrared Emission CuInS/ZnS Quantum Dots: All-in-One Theranostic Nanomedicines with Intrinsic Fluorescence/Photoacoustic Imaging for Tumor Phototherapy. *ACS Nano* **2016**, *10* (10), 9637-9645. DOI: 10.1021/acsnano.6b05419.

(25) Speranskaya, E. S.; Beloglazova, N. V.; Abé, S.; Aubert, T.; Smet, P. F.; Poelman, D.; Goryacheva, I. Y.; De Saeger, S.; Hens, Z. Hydrophilic, Bright CuInS2 Quantum Dots as Cd-Free Fluorescent Labels in Quantitative Immunoassay. *Langmuir* **2014**, *30* (25), 7567-7575. DOI: 10.1021/la501268b.

(26) Bae, W. K.; Joo, J.; Padilha, L. A.; Won, J.; Lee, D. C.; Lin, Q.; Koh, W. K.; Luo, H.; Klimov, V. I.; Pietryga, J. M. Highly effective surface passivation of PbSe quantum dots

through reaction with molecular chlorine. *J Am Chem Soc* **2012**, *134* (49), 20160-20168. DOI: 10.1021/ja309783v From NLM.

(27) Bharali, D. J.; Lucey, D. W.; Jayakumar, H.; Pudavar, H. E.; Prasad, P. N. Folate-Receptor-Mediated Delivery of InP Quantum Dots for Bioimaging Using Confocal and Two-Photon Microscopy. *Journal of the American Chemical Society* **2005**, *127* (32), 11364-11371. DOI: 10.1021/ja051455x.

(28) Shen, J.; Zhu, Y.; Yang, X.; Li, C. Graphene quantum dots: emergent nanolights for bioimaging, sensors, catalysis and photovoltaic devices. *Chemical Communications* **2012**, *48* (31), 3686-3699, 10.1039/C2CC00110A. DOI: 10.1039/C2CC00110A.

(29) Erogbogbo, F.; Yong, K.-T.; Roy, I.; Hu, R.; Law, W.-C.; Zhao, W.; Ding, H.; Wu, F.; Kumar, R.; Swihart, M. T.; et al. In Vivo Targeted Cancer Imaging, Sentinel Lymph Node Mapping and Multi-Channel Imaging with Biocompatible Silicon Nanocrystals. *ACS Nano* **2011**, *5* (1), 413-423. DOI: 10.1021/nn1018945.

(30) Sze, S. M. *Physics of Semiconductor Devices*; Wiley, N.Y., 1985.

(31) de Mello Donegá, C.; Bode, M.; Meijerink, A. Size- and temperature-dependence of exciton lifetimes in CdSe quantum dots. *Physical Review B* **2006**, *74* (8), 085320. DOI: 10.1103/PhysRevB.74.085320.

(32) Gärtner, W. W. Photothermal Effect in Semiconductors. *Physical Review* **1961**, *122* (2), 419-424. DOI: 10.1103/PhysRev.122.419.

(33) Robinson, J. T.; Tabakman, S. M.; Liang, Y.; Wang, H.; Sanchez Casalongue, H.; Vinh, D.; Dai, H. Ultrasmall Reduced Graphene Oxide with High Near-Infrared Absorbance for Photothermal Therapy. *Journal of the American Chemical Society* **2011**, *133* (17), 6825-6831. DOI: 10.1021/ja2010175.

(34) Ishii, S.; Sugavaneshwar, R. P.; Chen, K.; Dao, T. D.; Nagao, T. Solar water heating and vaporization with silicon nanoparticles at mie resonances. *Opt. Mater. Express* **2016**, *6* (2), 640-648. DOI: 10.1364/OME.6.000640.

(35) Wang, S.; Lin, J.; Huang, P. Advances on the Use of Biodegradable Proteins/Peptides in Photothermal Theranostics. *Journal of Nanomaterials* **2016**, *2016*. DOI: Artn 5810952 10.1155/2016/5810952.

(36) Chen, X.-M.; Mao, J.; Zhou, Y.-Z.; Yang, J.; Du, X.-W.; Qiao, S.-Z. Laser-driven absorption/desorption of catalysts for producing nanowire arrays in solution. *Journal of Materials Chemistry A* **2016**, *4* (2), 379-383, 10.1039/C5TA09325B. DOI: 10.1039/C5TA09325B.

(37) Hwang, D. J.; Ryu, S.-G.; Grigoropoulos, C. P. Multi-parametric growth of silicon nanowires in a single platform by laser-induced localized heat sources. *Nanotechnology* **2011**, *22* (38), 385303. DOI: 10.1088/0957-4484/22/38/385303.

(38) Crane, M. J.; Zhou, X.; Davis, E. J.; Pauzauskie, P. J. Photothermal Heating and Cooling of Nanostructures. *Chemistry – An Asian Journal* **2018**, *13* (18), 2575-2586. DOI: 10.1002/asia.201800251.

(39) Li, Z. F.; Ruckenstein, E. Water-Soluble Poly(acrylic acid) Grafted Luminescent Silicon Nanoparticles and Their Use as Fluorescent Biological Staining Labels. *Nano Letters* **2004**, *4* (8), 1463-1467. DOI: 10.1021/nl0492436.

(40) Mastronardi, M. L.; Henderson, E. J.; Puzzo, D. P.; Ozin, G. A. Small silicon, big opportunities: the development and future of colloidally-stable monodisperse silicon nanocrystals. *Advanced materials (Deerfield Beach, Fla.)* **2012**, *24* (43), 5890-5898. DOI: 10.1002/adma.201202846 From NLM.

(41) Chen, Y.; Sun, L.; Liao, F.; Dang, Q.; Shao, M. Fluorescent-stable and water-soluble two-component-modified silicon quantum dots and their application for bioimaging. *Journal of Luminescence* **2019**, *215*, 116644. DOI: https://doi.org/10.1016/j.jlumin.2019.116644.

(42) Özbilgin, İ. N. G.; Ghosh, B.; Yamada, H.; Shirahata, N. Size-Dependent Photothermal Performance of Silicon Quantum Dots. *The Journal of Physical Chemistry C* **2021**, *125* (6), 3421-3431. DOI: 10.1021/acs.jpcc.0c10027.

(43) Regli, S.; Kelly, J. A.; Shukaliak, A. M.; Veinot, J. G. C. Photothermal Response of Photoluminescent Silicon Nanocrystals. *The Journal of Physical Chemistry Letters* **2012**, *3* (13), 1793-1797. DOI: 10.1021/jz3004766.

(44) Lee, C.; Kim, H.; Cho, Y.; Lee, W. I. The properties of porous silicon as a therapeutic agent via the new photodynamic therapy. *Journal of Materials Chemistry* **2007**, *17* (25), 2648-2653, 10.1039/B700892A. DOI: 10.1039/B700892A.

(45) Shen, H.; You, J.; Zhang, G.; Ziemys, A.; Li, Q.; Bai, L.; Deng, X.; Erm, D. R.; Liu, X.; Li, C.; et al. Cooperative, nanoparticle-enabled thermal therapy of breast cancer. *Advanced healthcare materials* **2012**, *1* (1), 84-89. DOI: 10.1002/adhm.201100005 From NLM.

(46) Park, G.-S.; Kwon, H.; Kwak, D. W.; Park, S. Y.; Kim, M.; Lee, J.-H.; Han, H.; Heo, S.; Li, X. S.; Lee, J. H.; et al. Full Surface Embedding of Gold Clusters on Silicon Nanowires for Efficient Capture and Photothermal Therapy of Circulating Tumor Cells. *Nano Letters* **2012**, *12* (3), 1638-1642. DOI: 10.1021/nl2045759.

(47) Su, Y.; Wei, X.; Peng, F.; Zhong, Y.; Lu, Y.; Su, S.; Xu, T.; Lee, S.-T.; He, Y. Gold Nanoparticles-Decorated Silicon Nanowires as Highly Efficient Near-Infrared Hyperthermia Agents for Cancer Cells Destruction. *Nano Letters* **2012**, *12* (4), 1845-1850. DOI: 10.1021/nl204203t.

Chapter 2: Synthesis and Characterization of Water-Soluble Silicon Quantum Dots

2.1. Introduction

Surface modification of SiQDs is essential to provide their utilizability in various application areas. However, surface structure of SiQDs is complex and inhomogenous. Due to the small size, it has high surface area, therefore, surface is prone to oxygen and water. On the other hand, surface modification of SiQDs effects its photoemission properties. Also, surface modification of SiQDs may provide chemical durability, solubility in various solvents and prevention of undesired oxidation. Therefore, tailoring the surface properties of SiQDs has become crucial to actualize their potential applications.

Surface modification of SiQDs have started with oxide shell covering on core SiQDs. Despite its versatility, decreasing PL after shell formation limited its further use. Ligand exchange process is commonly used method to give SiQDs functionalization in a wide range. In this process, chemically active SiQDs terminated by halides or hydrides as surfactant molecules are required to realize replacement with ligands such as thiols, polymers or certain inorganic ligands.[1] Figure 2.1 shows the common routes for preparation of halide and hydride terminated SiQDs and modification of their surface by different moieties.

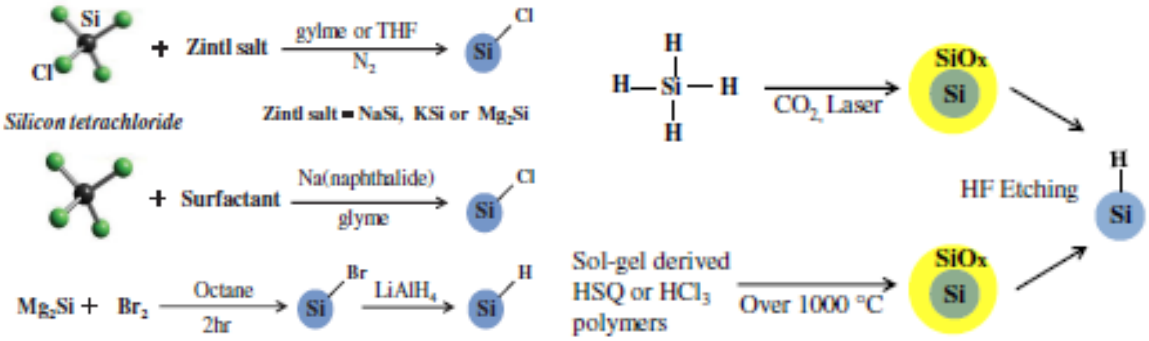

Figure 2.1. Common preparation routes for hydride and halide terminated SiQDs

Theoretical studies on the effect of surface modification on the band properties of SiQDs were performed and verified by many experimental studies. For instance, direct

bandgap behavior in ultrasmall SiQDs was first suggested by Brus et. al. then experimentally proved by data obtained from different methods.[2-4] It was shown by density functional theory calculations that optical properties of hydrogen terminated SiQDs has minimally changed after modification of their surface by alkyl group[5] and carbon chain length did not affect the band structure (Figure 2.2).[6] Whereas, modification with long chain molecules yield more stable SiQDs while preventing agglomeration and ligand exchange process is more challenging. Modification with oxygen species does not significantly effect absorption behavior while redshifts the emission wavelength.[7] Experimentally, modification by water soluble moieties and changing SiQD media to aqueous show decrease in PL intensity and PLQY. This behavior is attributed to be originated from emergence of non-radiative oxide-related states during the process.[8]

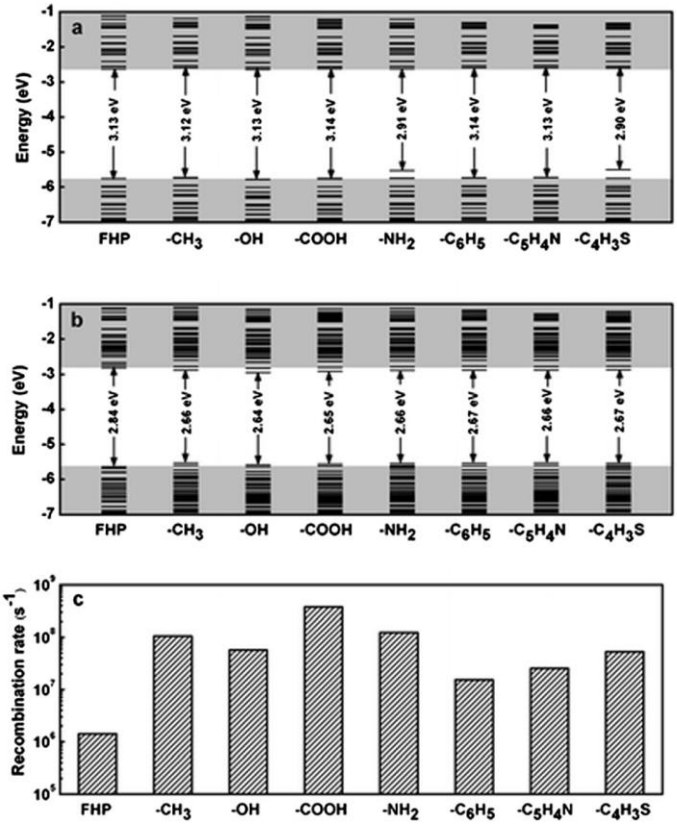

Figure 2.2. Energy-level diagrams of a Si NC with varying functional groups at the distal end of an alkene-derived ligand attached to the NC surface at the distal end of an alkene derived ligand attached to the QD surface. Alkenes with functional groups are in the form of H_2C=CHX (X=OH, COOH, NH_2, C_6H_5, C_5H_4N, and C_4H_3S). Full hydrogen passivation (FHP) and hydrosilylation with one H_2C=CH−CH_3 molecule are also included for comparison.

When considered the number of studies made on Si, realization of 'perfect' SiQDs suitable for wide variety of applications is still challenging by means of reproducibility, size dispersibility and stability. Also, their performance should be detailly evaluated to integrate them to applications. For bioapplications, synthesis of water soluble SiQDs with substantial stability and PLQY is crucial. Modification of SiQD surface via Si-C bond is attractive due to its thermodynamic and kinetic stability originating from high bonding strength and low polarity.[9] Water solubility can be provided by a convenient hydrosilylation method which

involves Si-C bonding through thermal inducement of unsaturated C=C groups. In this chapter, synthesis of undecanoic acid functionalized water soluble SiQDs were investigated.

2.2. Experimental Procedure

In this section, preparation of H-SiQDs, hydrosilylation and then characterization studies is presented. Undecanoic acid terminated SiQDs were prepared via hydrosilylation of H-SiQDs. Crystal structure of prepared SiQDs were characterized by X-Ray powder diffraction (XRD) method. Surface characterization was done by FTIR, Zeta potential and TGA. Optimization of synthesis parameters were made by considering PLQY values.

2.2.1. Reagents and Chemicals

All reagents were used without further purification. Triethoxysilane (TES) and 10-undecenoic acid were purchased from Tokyo Chemical Industry (TCI) Co., Ltd. Hydrochloric acid (HCl, 49% aqueous solution, electronic grade), hydrofluoric acid (HF; 46−51% aqueous solution, metal impurity <100 ppm) and methyl n-decanoate were purchased from Kanto Reagents. Ethanol, acetonitrile and dichloromethane were purchased from Wako Chemicals. Milli-Q Water (18 MΩ cm resistivity) was obtained from Sartorius Arium 611UV water purification system.

2.2.2. Preparation of Hydrogen Terminated SiQDs

16 mL of TES was hydrolyzed by using HCl solution of pH 3 under Ar flow. Solution was filtrated and obtained white precipitate was washed with deionized water until its pH becomes 7. Washed precipitate was left to dry overnight under vacuum. Particle size of final powder was tuned by heat treatment to white precipitate according to following equation:[10]

$$4HSi(OCH_2CH_3)_3 + 6H_2O \rightarrow 4HSiO_{1.5} + 12CH_3CH_2OH \quad (1)$$

Dried powder was put to a vacuum furnace in a quartz crucible. Thermal disproportionation of hydrogen silsesquioxane, i.e., $(HSiO_{1.5})_n$, was done at the temperatures between 1050–1190 °C. for 2 hours, under 5%-H_2/95%-Ar gas. Thus, $(HSiO_{1.5})_n$ was disproportionated into two oxidation states of Si (Si^0 and Si^{4+}) according to following equation:[10]

$$4HSiO_{1.5} \rightarrow Si + 3SiO_2 + 2H_2 \quad (2)$$

This heat treatment yielded brown powder composed of SiQDs dispersed in SiO_2 matrix. Next, 300 mg of the powder was grinded in agate mortar and then oxide part of the fine powder was removed by stirring in 24 mL acidic solution of HF with ethanol in the volume ratio of 1:2. Etching time is dependent on heat treatment. For sample having smallest QD diameter (2.2 nm) it is 30 minutes while the others are 60 minutes.

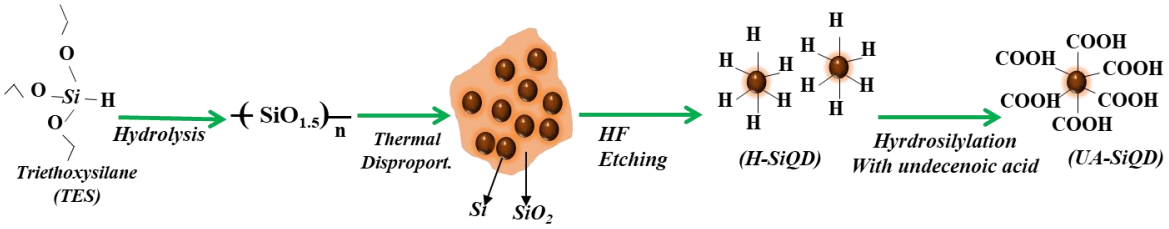

Figure 2.3. Synthesis route for undecanoic acid terminated SiQDs

After etching, solution was centrifuged at 15,000 rpm for 5 minutes at 10 °C by using ethanol and acetonitrile, respectively. Collected powder was dried under vacuum and characterized by XRD by means of crystal structure and QD size.

2.2.3. Preparation of Water-Soluble Si QDs

To give a water solubility, undecanoic acid was bonded covalently to the surface of SiQDs by thermal hydrosilylation of 10-undecenoic acid. Typically, 10 mL of 10-undecenoic acid was degassed at 90 °C for 4 h under vacuum conditions (~100 Pa). Then, the H-SiQDs collected by 2 mL of dichloromethane were added to the degassed solution. The obtained suspension was sonicated for 10 min and then heated to 160, 180 and 200 °C and kept for different durations from 0 to 180 minutes under Ar atmosphere and kept. After the reaction, 70 mL of ethanol was added to the suspension and sonicated for 15 min at 25 °C. The sonicated suspension was split into four centrifuge tubes and centrifuged at 8000 rpm for 15 min at 25 °C. The precipitated SiQDs were resuspended in two centrifuge tubes with a minimum amount of ethanol, and the rest was filled with hexane. Second centrifugation was performed at 15,000 rpm for 5 min at 25 °C. After decanting, SiQDs were dispersed in ethanol. Gradual switch from ethanol to water was carried out. First of all, same amount of

water was added to the ethanol solution of SiQDs. Then, thanol was removed by vacuum drying. Samples prepared for this thesis is summarized in Table 2.1.

Table 2.1. Synthesis conditions of prepared samples

Chapter #	Annotation	Si/SiOx heat treatment parameters			Hydrosilylation parameters	
		T(°C)	t_{HT} (min)	$t_{etching}$ (min)	T(°C)	Duration (min)
2	No annotation	1050	120	30	160	0, 15, 30, 45, 60, 75, 90, 105, 120, 135, 150, 165, 180
					180	0, 15, 30, 45, 60, 75, 90, 105, 120, 135, 150, 165
					200	0, 15, 30, 45, 60, 75, 90, 105, 120, 135
3	UA-SiQD S	1050	120	30	160	60
4	SiQD S	1050	120	30	X	X
	SiQD M	1100		60		
	SiQD L	1190		90		
5	UA-SiQD S	1050	120	30	160	60
	UA-SiQD-L	1190		90		

2.2.4. Characterization

Crystal structure of SiQDs were analyzed by XRD (HT-XRD, RINT-TTR II and Reactor X, Rigaku, Japan) with $Cu_{K\alpha}$ radiation at 40 kV voltage and 15 mA current. Measurements were done with dropcast samples of ethanol-SiQD solutions from 10 to 65 ° with 2 degrees/min scan speed and 0.02 degrees step size.

Surface properties of samples were examined by attenuated total reflectance Fourier transform infrared spectroscopy (ATR-FTIR) measurements in 750-2300 cm^{-1} frequency range by JASCO FTIR 4100 spectrometer. Zeta potential of UV:SiQDs dispersed in water was also measured by using Malvern Zetasizer Nano-Z zeta potential analyzer. Surface coverage of the UA:SiQDs was calculated from the measured mass loss by

Thermogravimetric Analysis (TGA) measurement. For the measurement, 4 mg SiQDs in powder form was put in alumina crucibles. The sample chamber was purged with Ar gas in several times to remove oxygen for precise measurement. Sample was heated with 10 °C min^{-1} rate up to 650 °C under Ar atmosphere. Surface coverage was calculated by the method reported by J. Mock *et al*.[11] The specific procedure was shown below. The diameter of UA-SiQD was ~1.8 nm determined from the relationship between PL peak wavelength and QD size which is established in the 1.7-5.0 nm diameter range.[12, 13] According to S. Niaz *et al*., 1.836 nm T_d symmetry SiQD has the molecular formula of $Si_{147}H_{100}$.[14] The total amount of 100 SiH surface groups per SiQD expressed n_{SiH}, is determined by the ratio of the sample weight at the end temperature m_{end} to the molecular weight of the Si core M_{Si}. (Equation 2.1):

$$n_{SiH}[mol] = \frac{m_{end}}{M_{Si}}.100 \qquad \textbf{(2.1)}$$

The amount of surface ligands n_{Ligand} is determined by the ratio of the mass loss Δm of the sample to the molar weight of the ligand M_{Ligand}. (Equation 2.2):

$$n_{Ligand}[mol] = \frac{\Delta m}{M_{Ligand}} \qquad \textbf{(2.2)}$$

Finally, from equations (1) and (2), surface coverage can be obtained by Equation 2.3.

$$Surface\ coverage\ [\%] = \frac{n_{Ligand}}{n_{SiH}} \qquad \textbf{(2.3)}$$

Photoluminescence (PL) properties of water-UA:SiQD and MEM-UA:SiQD solutions were measured by a modular double grating Czerny-Turner monochromator and an iHR 320 emission monochromator (1200 lines/mm of gratings) coupled to a photodetector on NanoLog Horiba Jobin Yvon spectrofluorometer with 450 W Xe arc lamp. For observation of PL stability, aqueous solution of SiQD at 37 °C was measured at 1st, 6th, 10th and 18th days of the synthesis. PL quenching behavior of SiQDs with 680 nm PL emission was

observed comparably with commercial DAPI 580 nm PL emission for nucleic acid staining by 5 hours recorded time-resolved PL decay curves were acquired with the same spectrofluorometer, using a pulsed spectral LED of 350 nm emission. The absolute PLQYs were measured at room temperature using the QY measurement system C9920-02 from Hamamatsu Photonics Co., Ltd. with a 150 W Xenon lamp coupled to a monochromator for wavelength discrimination, an integrating sphere as a sample chamber, and a multichannel analyzer for signal detection. The solution-form samples of the QDs were used for PLQYs. Corresponding PL peaks were extracted from PLQY analysis were used to observe dependence of synthesis parameters.

2.3. Results and Discussion

Figure 2.4a shows a typical XRD pattern of UA:SiQDs. Characteristic diffraction peaks of Si belonging to (111), (220) and (311) planes of diamond cubic structure at 2θ= 28, 47 and 56°, respectively were observed.

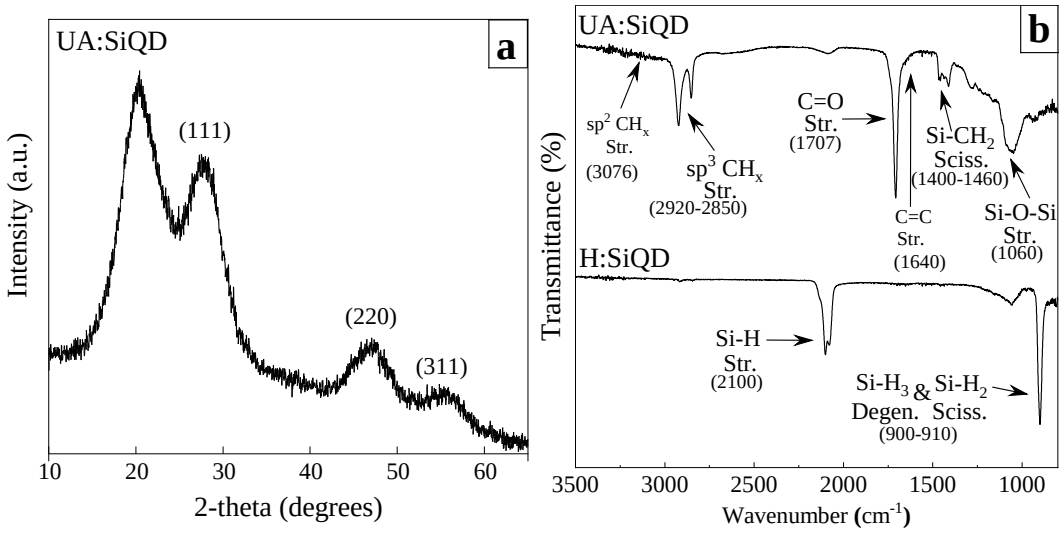

Figure 2.4. Structural characterization results of a) XRD profile of UA:SiQDs, b)ATR-FTIR spectra of H:SiQDs and UA:SiQDs

In Figure 2.4b, surface characteristics obtained by FTIR showed the decrease in the intensity of peak positioned at 2100 cm^{-1} belongs to Si-H bonds which refers to formation of new bondings by Si. Yet, signals from Si-H bonds are still observed as a small peak after

hydrosilylation. Together with these peaks belonging to non-polar vinyl groups such as sp^2 CH_x stretching mode at 3076 cm^{-1} and C=C stretching mode at 1640 cm^{-1} of 10-undecenoic acid show low intensity or disappearance. Peaks belonging to Si-CH_2 scissoring mode at 1400-1450 cm^{-1}, sp^3 CH_x at 2852 and 2920 cm^{-1}, C=O stretching mode at 1707 cm^{-1} and evidence of C-O stretching mode (in the range of 1210-1320 cm^{-1}) confirms the successful attachment and polarity of the SiQD surface. Findings are similar to that of previously reported Si-10-undecenoic acid studies.[9, 15, 16] Surface capping by water soluble moieties are confirmed by highly stable, clear solutions of SiQDs with –55.3±1.74 mV zeta potential. This value is at the upper limits of the reported zeta potential range of carboxylic acid coated nanoparticles.[17] When reported zeta potential of carboxyl monolayers on gold[13] substrate, which is about -70 mV[18], is considered, obtained value is reasonable due to the oxidation of unmodified area included in UA:SiQDs, which was also evidenced by FTIR.

The solubility of H:SiQDs into water is given by hydrosilylation of ω-functionalized 1-alkene in which one end with carbon−carbon double bond while the other distal end with hydrophilic polar groups, such as carboxylic acid. Unlike 1-alkenes which give high coverage monolayers grafted to the SiQD surface, there is only a few papers on this kind of monolayers. To estimate the molecular packing density of undecanoic acid giving a transparent and aqueous solution, TG measurement was performed. Results of TGA measurements show 48% mass loss between 450 and 550 °C can be seen in Figure 2.5. Surface coverage was determined by ratio of surface ligands obtained from mass loss data to SiH surface groups[11]. The undecanoic acid has shown 22% coverage on SiQDs.

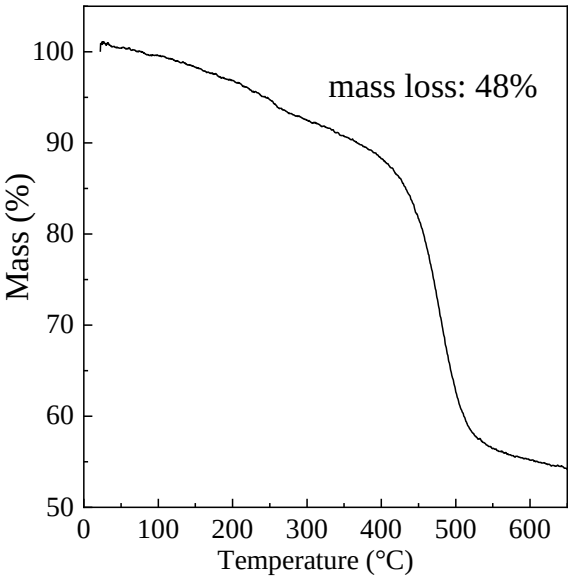

Figure 2.5. TG measurement result of UA:SiQDs

Due to good crystallinity and surface termination properties, clear aqueous solutions of SiQDs up to concentrations as high as 4 mg/mL could be prepared. PL emission from prepared solutions vary from 680 nm to 720 nm. The samples that have PL peak under 700 nm have 14-16% PLQY while samples with PL peak above 700 nm have 20% or more. Therefore, detailed investigation on latter-mentioned samples was carried out. The reason for lower PLQY of SiQDs having shorter PL wavelength may be due to agglomeration due to long surface chains that may affect radiative recombination. Figure 2.6 shows prepared solutions at different concentration under white light and UV light. Due to high PLQY, red emission could be seen clearly even when irradiated by UV light under white light.

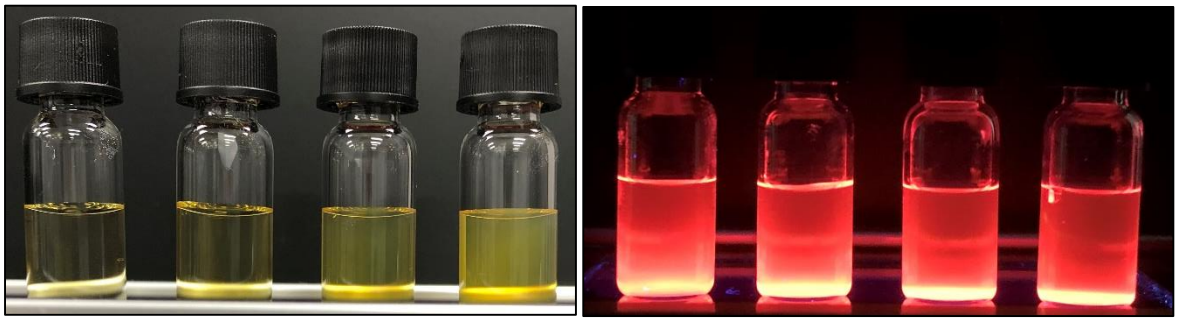

Figure 2.6. Aqueous SiQD solutions under a) white light and b) UV light

Stability of SiQDs in biological environment is one of the most important requirements for practical use. To observe their optical performance, PL measurement of solutions at 37 C at different times after synthesis was performed together with PL lifetime studies to observe their photostability. In Figure 2.7a, normalized PL peaks on the 1^{st}, 6^{th}, 10^{th} and 15^{th} day of synthesis are shown. It is seen that peak shape haven't changed during exposure. PL peak has blueshifted 13 nm. This could be due to decrease of Si core with time dependent oxidation, provoking an increase in the fundamental energy gap based on the quantum confinement effect.[19] Figure 2.7b shows time resolved PL decay curves were obtained by irradiation of UA:SiQDs and commercial DAPI staining dye at 680 nm and 580 nm, respectively. Excitation of DAPI was done for both 365 nm and 405 nm which is near its excitation maxima.[20] Constantly gradual decrease in intensity from DAPI excited at 365 nm was obtained. At 405 nm excitation, before fixing, obtained intensity decreased until 1 hour. When intensity decrease after 1 hour for UA:SiQDs and DAPI at their excitation maxima, it is seen that decrease of obtained intensity for UA:SiQDs is only 14%. After 5 hours, loss of the obtained intensity increased to 29%. For DAPI, this decrease amounts are 34% and 40%, respectively. This result shows that SiQDs are more resistant to long exposures of irradiation.

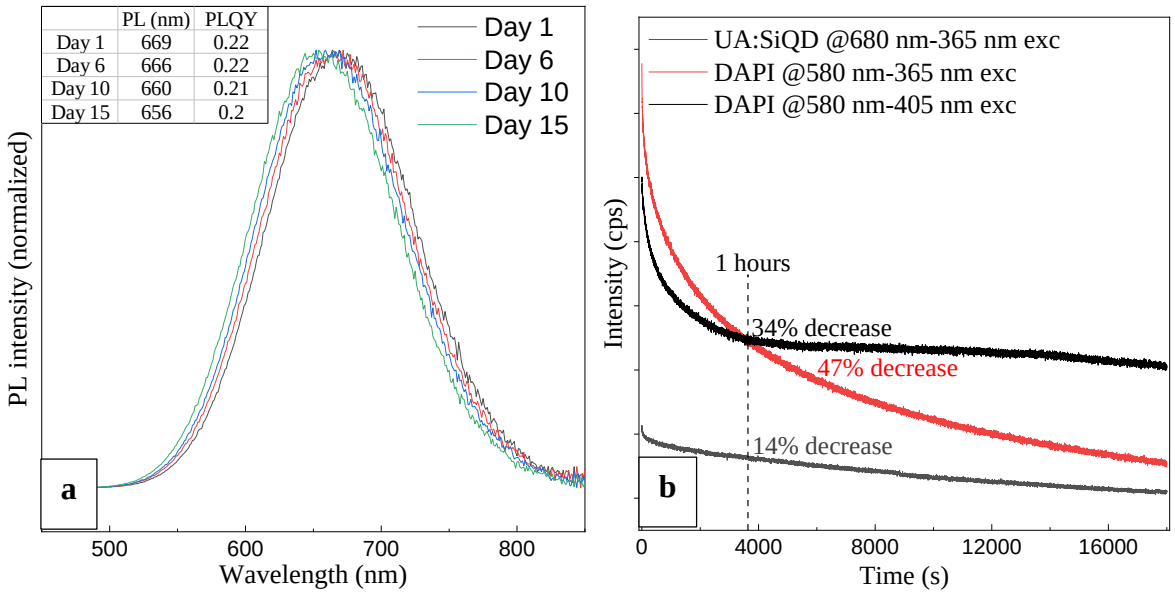

Figure 2.7. a) normalized PL peaks on the 1st, 6th, 10th and 15th day of synthesis, b) time resolved PL decay curves of UA:SiQDs and commercial DAPI staining dye at 680 nm and 580 nm, respectively.

Optimization of reaction temperature and duration was performed. Figure 2.8 shows PLQY and PL peak position change depending on synthesis duration at three different temperatures. For each determined temperature, similar PLQY and PL changing trend was observed. Sharp increase of PLQY occurs in shorter times for 180 and 200 °C. Effect of synthesis duration is not significant after 45 minutes. Similarly, PL peak position also stays within about 5 nm fluctuation. Considering PL peak positions, it can be seen that particle size increased with increasing temperature but then decrease with further increase to 200 °C, together with overall PLQY. It implies that QD degradation may occur when synthesis was carried out at high temperature.

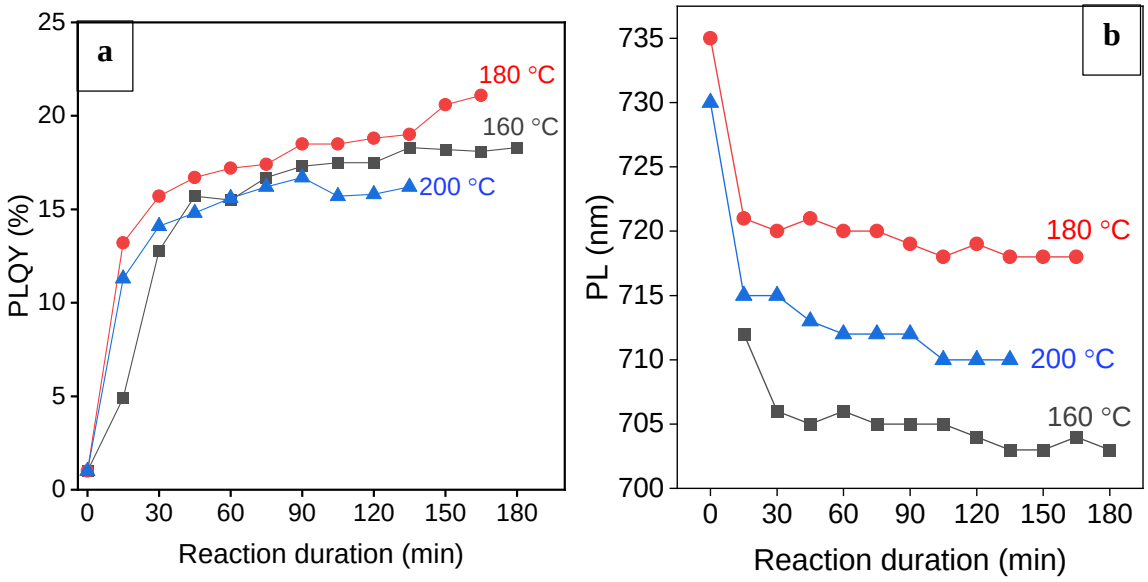

Figure 2.8. a) PLQY and b) PL peak position change depending on synthesis duration at three different temperatures

2.4. Conclusion

In this chapter, synthesis of stable, water soluble SiQDs was achieved. H:SiQDs were successfully terminated by long undecanoic acid chains with 22% surface coverage. For synthesis, no significant change in PL and PLQY was observed after 60 minutes and high temperature causes decrease in PL. optical properties of UA:SiQDs imply that SiQDs are stable with small amount of oxidation at basal temperatures even after 15 days. PL quenching behaviour of SiQDs were observed to be superior to commercially available dye.

2.5. References

(1) Estelrich, J.; Busquets, M. A. Iron Oxide Nanoparticles in Photothermal Therapy. *Molecules* **2018**, *23* (7), 1567.

(2) Vines, J. B.; Yoon, J.-H.; Ryu, N.-E.; Lim, D.-J.; Park, H. Gold Nanoparticles for Photothermal Cancer Therapy. *Frontiers in Chemistry* **2019**, *7* (167), Review. DOI: 10.3389/fchem.2019.00167.

(3) Moustaoui, H.; Saber, J.; Djeddi, I.; Liu, Q.; Diallo, A. T.; Spadavecchia, J.; Lamy de la Chapelle, M.; Djaker, N. Shape and Size Effect on Photothermal Heat Elevation of Gold Nanoparticles: Absorption Coefficient Experimental Measurement of Spherical and Urchin-Shaped Gold Nanoparticles. *The Journal of Physical Chemistry C* **2019**, *123* (28), 17548-17554. DOI: 10.1021/acs.jpcc.9b03122.

(4) Wang, X.; Li, G.; Ding, Y.; Sun, S. Understanding the photothermal effect of gold nanostars and nanorods for biomedical applications. *RSC Advances* **2014**, *4* (57), 30375-30383, 10.1039/C4RA02978J. DOI: 10.1039/C4RA02978J.

(5) Özbilgin, İ. N. G.; Ghosh, B.; Yamada, H.; Shirahata, N. Size-Dependent Photothermal Performance of Silicon Quantum Dots. *The Journal of Physical Chemistry C* **2021**, *125* (6), 3421-3431. DOI: 10.1021/acs.jpcc.0c10027.

(6) Hessel, C. M.; Reid, D.; Panthani, M. G.; Rasch, M. R.; Goodfellow, B. W.; Wei, J.; Fujii, H.; Akhavan, V.; Korgel, B. A. Synthesis of Ligand-Stabilized Silicon Nanocrystals with Size-Dependent Photoluminescence Spanning Visible to Near-Infrared Wavelengths. *Chemistry of Materials* **2012**, *24* (2), 393-401. DOI: 10.1021/cm2032866.

(7) Shirahata, N.; Nakamura, J.; Inoue, J.-i.; Ghosh, B.; Nemoto, K.; Nemoto, Y.; Takeguchi, M.; Masuda, Y.; Tanaka, M.; Ozin, G. A. Emerging Atomic Energy Levels in Zero-Dimensional Silicon Quantum Dots. *Nano Letters* **2020**, *20* (3), 1491-1498. DOI: 10.1021/acs.nanolett.9b03157.

(8) Erogbogbo, F.; Yong, K.-T.; Roy, I.; Xu, G.; Prasad, P. N.; Swihart, M. T. Biocompatible Luminescent Silicon Quantum Dots for Imaging of Cancer Cells. *ACS Nano* **2008**, *2* (5), 873-878. DOI: 10.1021/nn700319z.

(9) Wang, J.; Liu, Y.; Peng, F.; Chen, C.; He, Y.; Ma, H.; Cao, L.; Sun, S. A General Route to Efficient Functionalization of Silicon Quantum Dots for High-Performance Fluorescent Probes. *Small* **2012**, *8* (15), 2430-2435. DOI: https://doi.org/10.1002/smll.201102627.

(10) Ghosh, B.; Masuda, Y.; Wakayama, Y.; Imanaka, Y.; Inoue, J.; Hashi, K.; Deguchi, K.; Yamada, H.; Sakka, Y.; Ohki, S.; et al. Hybrid White Light Emitting Diode Based on Silicon Nanocrystals. *Advanced Functional Materials* **2014**, *24* (45), 7151-7160. DOI: 10.1002/adfm.201401795.

(11) Mock, J.; Groß, E.; Kloberg, M. J.; Rieger, B.; Becherer, M. Surface Engineering of Silicon Quantum Dots: Does the Ligand Length Impact the Optoelectronic Properties of Light-Emitting Diodes? *Advanced Photonics Research n/a* (n/a), 2100083. DOI: https://doi.org/10.1002/adpr.202100083.

(12) Hemmer, E.; Benayas, A.; Légaré, F.; Vetrone, F. Exploiting the biological windows: current perspectives on fluorescent bioprobes emitting above 1000 nm. *Nanoscale Horizons* **2016**, *1* (3), 168-184, 10.1039/C5NH00073D. DOI: 10.1039/C5NH00073D.

(13) Chandra, S.; Ghosh, B.; Beaune, G.; Nagarajan, U.; Yasui, T.; Nakamura, J.; Tsuruoka, T.; Baba, Y.; Shirahata, N.; Winnik, F. M. Functional double-shelled silicon nanocrystals for two-photon fluorescence cell imaging: spectral evolution and tuning. *Nanoscale* **2016**, *8* (16), 9009-9019, 10.1039/C6NR01437B. DOI: 10.1039/C6NR01437B.

(14) Suzuki, K. Quantaurus-QY: Absolute photoluminescence quantum yield spectrometer. *Nature Photonics* **2011**, *5* (5), 247-247. DOI: 10.1038/nphoton.an.2011.1.

(15) Yu, Y.; Hessel, C. M.; Bogart, T. D.; Panthani, M. G.; Rasch, M. R.; Korgel, B. A. Room Temperature Hydrosilylation of Silicon Nanocrystals with Bifunctional Terminal Alkenes. *Langmuir* **2013**, *29* (5), 1533-1540. DOI: 10.1021/la304874y.

(16) Clark, R. J.; Dang, M. K. M.; Veinot, J. G. C. Exploration of Organic Acid Chain Length on Water-Soluble Silicon Quantum Dot Surfaces. *Langmuir* **2010**, *26* (19), 15657-15664. DOI: 10.1021/la102983c.

(17) Mahalingam, V.; Onclin, S.; Péter, M.; Ravoo, B. J.; Huskens, J.; Reinhoudt, D. N. Directed Self-Assembly of Functionalized Silica Nanoparticles on Molecular Printboards

through Multivalent Supramolecular Interactions. *Langmuir* **2004**, *20* (26), 11756-11762. DOI: 10.1021/la047982w.

(18) Schweiss, R.; Pleul, D.; Simon, F.; Janke, A.; Welzel, P. B.; Voit, B.; Knoll, W.; Werner, C. Electrokinetic Potentials of Binary Self-Assembled Monolayers on Gold: Acid−Base Reactions and Double Layer Structure. *The Journal of Physical Chemistry B* **2004**, *108* (9), 2910-2917. DOI: 10.1021/jp035724m.

(19) Regli, S.; Kelly, J. A.; Shukaliak, A. M.; Veinot, J. G. C. Photothermal Response of Photoluminescent Silicon Nanocrystals. *The Journal of Physical Chemistry Letters* **2012**, *3* (13), 1793-1797. DOI: 10.1021/jz3004766.

(20) Hua, F.; Swihart, M. T.; Ruckenstein, E. Efficient Surface Grafting of Luminescent Silicon Quantum Dots by Photoinitiated Hydrosilylation. *Langmuir* **2005**, *21* (13), 6054-6062. DOI: 10.1021/la0509394.

Chapter 3: Photothermal Effect in Silicon Quantum Dots

3.1. Introduction

The photothermal responses of crystalline Si have been investigated for various forms, including nanoribbons,[1] nanowires,[2-4] films,[5] porous particles,[6] and NPs.[7-10] Multiple structural parameter such as size, shape, and surface configuration may affect the photothermal responses. As for NPs, photothermal responses have been studied for different diameter ranges of 30–110 nm,[7] 27–41 nm,[10] and 4.2–7.8 nm,[8] which are mostly larger in size than the bulk exciton Bohr radius for crystalline Si (d = ~5 nm). In such a big size regime (d >5 nm), the heat is enhanced as the NP size increases.[5, 8, 10] This temperature trend for larger NPs can be explained by the Mie resonances.[7]

In this study, we investigate the photothermal responses for Si QDs with varying diameters between 2 and 5 nm. It is known that the difference in surface chemistry of QDs influences on the photogenerated carrier transition. To avoid the unpredictable influence of the surface chemical configuration on photothermal performance, the QD surface was terminated with hydrogen atoms (H-SiQD). A hydrogen-terminated surface is not only nonpolar but also has the highest coverage of capping agents. Additionally, it prevents the presence of an unpassivated surface and is the starting stage for further functionalization on biocompatibility.[11-14]

3.2. Experimental procedure

3.2.1. Characterization

H-SiQDs having three different sizes under 5 nm were prepared by the method explained in Chapter 2. Particle size was calculated by using XRD data with Halder-Wagner method. SiQDs were examined to investigate the size distribution by HR-TEM. Surface oxides were investigated by FTIR (Section 2).

Absorption measurement was done for decane-terminated QDs in order to provide solubility in organic solvent and capping does not affect the absorption profile. The samples

having different concentrations in chloroform was analyzed using JASCO V-650 UV-Visible spectrometer.

Raman spectroscopy (RAMANplus, Nanophoton Co. Ltd., Japan) was used to investigate photothermal response. For this purpose, the samples of SiQD were dried and kept under argon or vacuum prior to the characterization in order to avoid possible oxidation of the hydrogen-terminated surfaces that are sensitive exposure to ambient air. The samples of H-SiQD (< 1mg) was put on a glass slide and gently grinded by a thinner glass slide on top. 532.32 nm monochromatic Raman laser was used at 100x magnification with 1200 gr/mm grating. These values were constant for all measurements. Two different experiments were conducted to observe photothermal response of H-SiQDs. Firstly, Raman laser was exposed to one point subsequently by increment in the range of 0.11 to 10 mW for 1 second and Stokes shift was observed. Other experiment was done to estimate temperature generated in the H-SiQDs. In this experiment, anti-Stokes to Stokes intensity ratio is necessary to calculate the temperature. In our case, we used an edge notch filter that blocks a 532-nm laser line (blocking range of ±300 cm^{-1}). Local temperature of irradiated point can be calculated by following Equation 3.1:[9]

$$T = \frac{h\vartheta_K}{k\left[-ln\left(\frac{\sigma[\alpha\vartheta_K]_S}{\sigma[\alpha\vartheta_K]_A}\right)\left(\frac{I_A[\vartheta_K]}{I_S[\vartheta_K]}\right)\left(\frac{\vartheta_0-\vartheta_K}{\vartheta_0+\vartheta_K}\right)^4\right]} \qquad \textbf{(3.1)}$$

where h and k are Planck and Boltzmann constants, respectively, ϑ_0 is the frequency of excitation laser source, $I_A[\vartheta_K]$ and $I_S[\vartheta_K]$ are anti-Stokes and Stokes Raman intensities, respectively, at the Raman scattering mode of interest ϑ_K, $\sigma[\alpha\vartheta_K]_S$ and $\sigma[\alpha\vartheta_K]_A$ are Stokes and anti-Stokes cross sections at the scattering mode of interest. $\frac{\sigma[\alpha\vartheta_K]_S}{\sigma[\alpha\vartheta_K]_A}$ value for each sample was calculated separately by using the data from lowest laser power with the assumption that temperature is 300 K at that point. For accuracy, our analyses were done from the different points for each exposure sequence. Three measurement data was used to get the lowest standard deviation. Raman peak measurement conditions were adjusted so as to get good signal to noise ratio. Adapting from the work by Sun *et al.*[9], we used the parameters listed in Table 3.1.

Table 3.1. Parameters for photothermal response observation by Raman spectroscopy

Power (mW)	Power Density (mW/cm^2)	Exposure Duration (s)	Repeats
0.11	26.94	100	20
2.90	712.74	10	15
5.95	1457.33	10	15
9.75	2388.05	3	30

To measure the PL spectra as a function of temperature, the samples were placed into cryostat holder connected to Gifford-McMahon cooler and controlled by Mercury iTC temperature controller. The temperature was precisely controlled in the range of 4.2 K to 300 K with 10 K steps.

3.3. Results and Discussion

Since the crystal momentum is not conserved in the quantum confined state of Si, the size greatly influences the fate of free-charge-carriers generated in QDs through the sequential absorption of photons at photoexcited conditions based on the assumption that individual QDs have a similar surface chemistry. Therefore, the determination of size should be indispensable to control the photothermal effect. Korgel and co-workers compared the size distribution estimated by TEM with the results obtained from complementary characterization techniques of XRD and small-angle X-ray scattering (SAXS).[15] The average diameters determined from SAXS are similar to those determined by Scherrer analysis of XRD peak broadening, but are slightly smaller than those estimated from TEM images. The overestimated diameters might be due to the presence of smaller QDs, which readily collapse under electron-beam irradiation of TEM.[4] It is noted that the diameters determined by the Scherrer analysis almost correspond to the values estimated from SAXS studies in the 1–5 nm diameter range.[15, 16]

Figure 3.1a shows the XRD patterns of the three H-SiQD samples. The diffraction peaks at 2θ=28°, 47°, and 56° are indexed to the (111), (220), and (311) planes of the diamond cubic lattice structure of Si. The diffraction lines broaden due to the smaller sizes and

distorted lattice structures of QDs. Their diameters were determined by theHalder-Wagner method, supported by Rigaku PDXL software by using the following Equation 3.2:

$$\left(\frac{\beta}{tan\,\theta}\right)^2 = \frac{K\lambda}{D}\cdot\frac{\beta}{tan\,\theta\,sin\,\theta} + 16\varepsilon^2 \qquad \textbf{(3.2)}$$

where β is the integral breadth, θ is the Bragg angle, K is the shape factor, D is the crystallite size, λ is the wavelength of the X-ray beam, ε is the isotropic microstrain. Determined particle sizes are 2.2±0.5 nm, 3.8±0.3 nm, and 4.7±0.5 nm. The effective mass approximation (EMA) is often used to study the relationship between the PL peak energy and size. For Si, an increasing trend of the PL peak energy is reproduced by EMA when the effective masses of the electron (m_e^*) and hole (m_h^*) are equal to $0.19m_0$ and $0.286m_0$ in the QD diameter range between 1.7 nm and 5 nm, respectively.[15, 16] The PL spectra H-SiQDs with 2.2, 3.8, and 4.7-nm diameters peak at 720, 985, and 1035 nm, respectively. The diameter of 4.7 nm is close to the bulk exciton radius for Si (~5 nm) (see Figure 3.1b). The two other relationships also agree with the theoretical ones. Hereafter, the samples are denoted as small (S), medium (M), and large (L).

Figure 3.1c shows the ATR-FTIR spectra of the (S), (M), and (L) samples. A weak absorption peak centered at 1060 cm^{-1} indicates the presence of a small amount of surface oxides, as evidenced by the O-Si-O stretching. The region near 2100 cm^{-1} is attributed to the SiH_x stretching mode.[17, 18] The absorption range at 900–910 cm^{-1} represents SiH_3 degenerate deformation and SiH_2 scissoring modes.[18] The integrated absorption intensity ratio of the Si-H vibration to the O-Si-O vibration observed in the 2.0–3.0 range suggests that most of the outermost Si atoms are terminated by hydrogen atoms.[16]

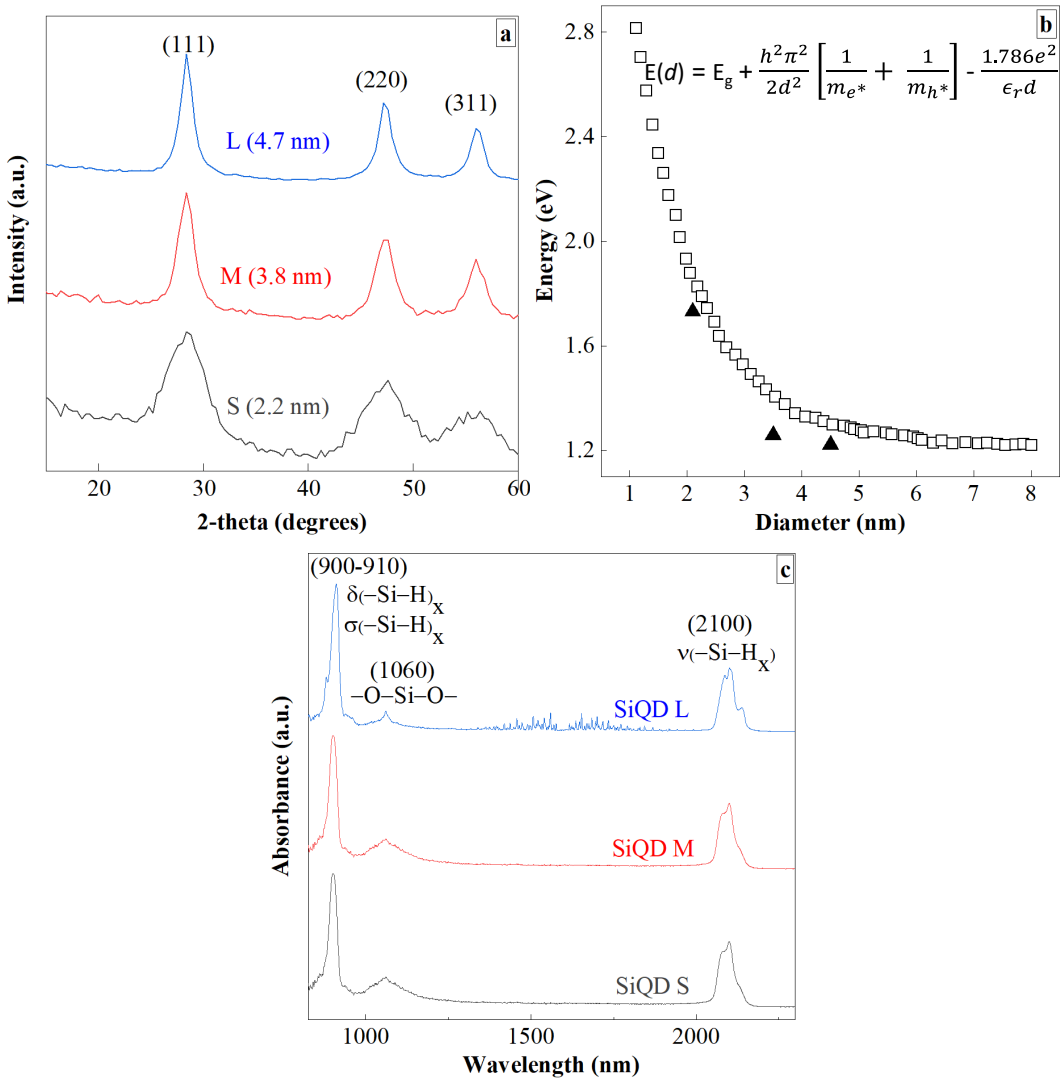

Figure 3.1. A summary of physical structures and PL properties of the samples (S), (M) and (L): a) XRD patterns. b) Peak PL energies plotted versus the QD diameter, in which the open-squares depict the theoretical relationship between the values of photon energy c calculated using the EMA and the diameters of QDs. c) ATR-FTIR spectra.

The optical absorption exhibited featureless and monotonic increasing behavior with wavelength at room temperature (Figure 3.2a). This is consistent with the theoretical prediction due to the smaller exciton binding energy than K_BT (~25 meV). Using the UV-vis spectra, the molar absorption coefficients ε of our QDs were estimated (Figure 3.2b) using the Beer-Lambert law (Equation 3.3):

$$A = \varepsilon cl \qquad \textbf{(3.3)}$$

where A is the measured absorbance at 420 nm, c denotes the molar concentration of QD, and l is the optical path length. For the measurement, the (S) sample was subjected to thermal hydrosilylation of 1-decene at 170 ºC for 5 min in an Ar atmosphere, yielding decane-terminated SiQDs, which are soluble in hydrophobic solvents such as toluene or hexane. The QD concentration varied from 0.04 to 0.1 mg/mL, yielding an estimated molar absorption coefficient of 1.98–3.83×10^5 M^{-1}·cm^{-1} at 425 nm. This value is as high as those measured for QDs of other semiconductors such as $CuInS_2$,[19, 20] InAs,[21] carbon,[22] and CdTe.[23]

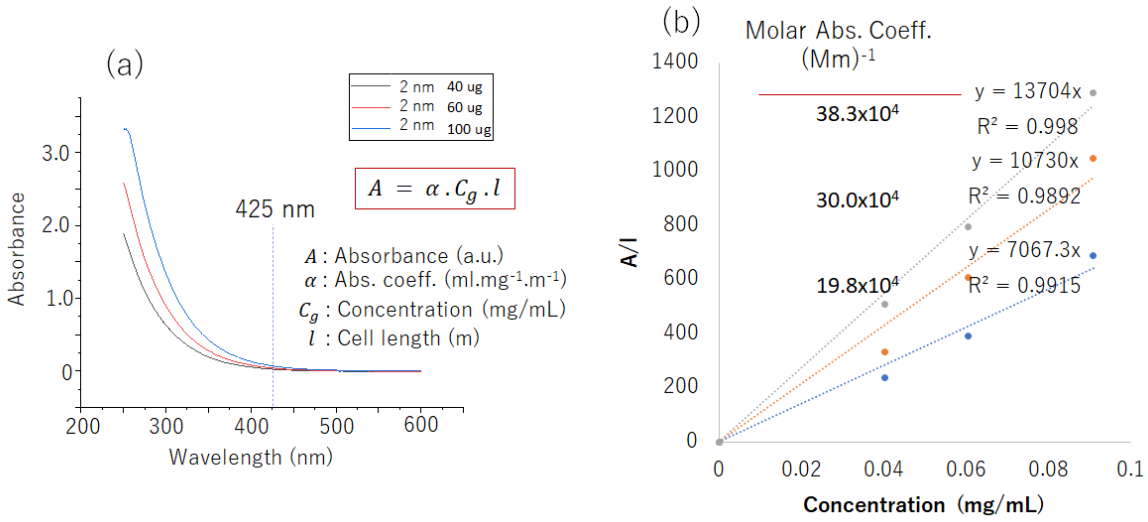

Figure 3.2. (a) UV-vis spectra of samples of 2 nm SiQDs terminated with decane monolayers, which are completely dispersed in toluene, at three different concentrations. Film forms of 40 µg, 60 µg and 100 µg of SiQDs with decane monolayers were used for measurement, giving the enhanced absorption with increasing weight of the QDs. (b) Absorbance normalized with respect to the cell length are plotted as a function of concentration of toluene solution of SiQD terminated with decane monolayers. The plots show linear relationships for each sample. R2 shows a good of fit for each concentration.

For crystalline Si, the Raman peak centered at 520 cm^{-1} is influenced by the strain, crystal size, and heating in the localized irradiation area with the incident light. Figure 3.3a shows the excitation-power dependence of the Raman shift for the (S), (M), and (L) samples.

A spectral redshift occurs as the laser power increases. A spectral downshift of the Raman bands is generally associated with heating by laser absorption, which induces tensile stress-induced effects.[6, 10] A significant downshift is observed for SiQD S and SiQD M sample, but SiQD L has relatively smaller downshift.

Raman heating occurs during illumination with a 532 nm laser. This wavelength corresponds to 1064 nm in two-photon excitation microscopy that enables an enhanced penetration depth, reduced background fluorescence, and reduced toxicity in a biological window.[24] Therefore, the heating experiment is thought to be representative for possible applications. The temperature rise traces as a function of the irradiation laser power density for the (S), (M), and (L) samples (see Figure 3.3b). It is noteworthy that the photothermal conversion performance clearly depends on the QD size even in the single nanometer range (i.e., 2–5 nm), and is enhanced for larger QDs. As predicted, gradually increasing trends of the steady-state temperature based on photothermal effect occur as the incident laser power density increases for all samples. The highest temperatures reached for (S), (M), and (L) samples are 220, 230, and 275 °C, respectively.

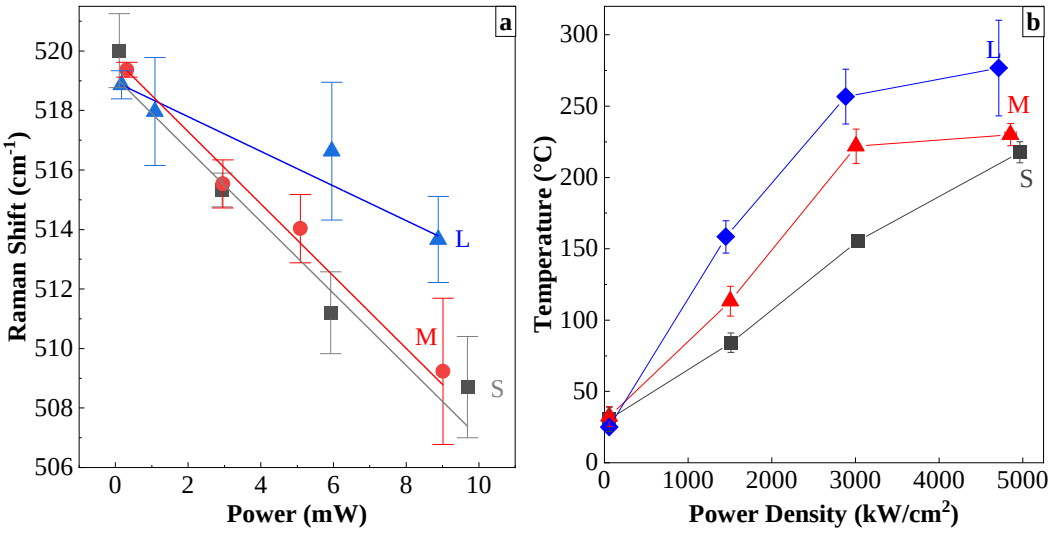

Figure 3.3. a) Change in Raman shift, and b) the estimated temperatures at different incident laser power for the samples (S), (M) and (L)

Most studies on the photothermal effect have investigated noble metals such as gold. Although the comparison is confined within a narrow limit of options for Si, we compare the photothermal performances of our samples with those reported in other studies in Figure 3.4. In general, the absorption coefficient becomes small with decreasing crystal size, resulting in a smaller size crystal that shows lesser heating performance than a bigger crystal,[25, 26] consistent with the plots displayed in Figure 3.2. In the QD size range, our results are consistent with those reported elsewhere. Compared to the increasing trend of temperature observed for a 3.5-nm SiQD encapsulated with SiO_2,[9] the estimated values of the temperature generated in the QD are slightly higher than those of the sample (M) over the whole incident laser power range. This might be due to the insulation effect of the oxide shell. In our work, the photothermal performance is enhanced for larger QDs. The radiative recombination between photoexcited electrons and holes in SiQDs is based on the uncertainty principle. With decreasing size of QDs, QC effects come into play, and for indirect band gap semiconductors such as Si as the size decreases, the more overlapping of the conduction band minimum and valance band maximum at the k = 0 point occurs, which increases the probability of radiative recombination. Because of this increasing quantum confinement, PLQY also increases as the size decreases. Whereas for larger QDs, the quantum confinement is weakened, which implies that more nonradiative pathways might contribute more in the photothermal effect as discussed later.

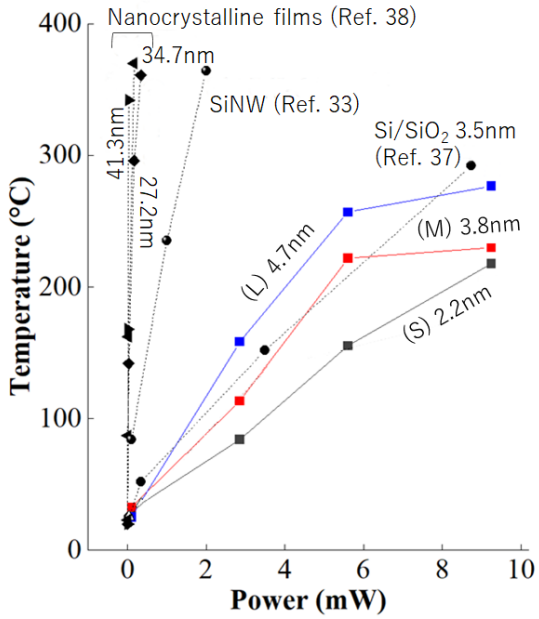

Figure 3.4. A summary of temperature rise traces of different sized and forms of Si nanomaterials as a function of incident laser power

Han et al. showed that 20−50 nm Si NPs could be heated to much higher temperatures,[10] when compared to our samples. In addition, their NPs exhibit a dramatic temperature increase based on the photothermal effect with a negligible increase in the incident laser power, suggesting that temperature control over heat is not straightforward in the lower temperature range (e.g., 200 °C or less). The comparison suggests that bigger NPs can be heated because heat transfer is ineffective because of the lack of physical interconnectedness, while a weak interconnection in QDs might be less effective on photothermal heating. Temperature dependence of the PL spectrum from room temperature to 433 K was also studied (Figure 3.5). The result is quite obvious as the temperature gradually increases from room temperature to 433 K the PL peak position has blue shifted and intensity decreased to nearly five times of the room-temperature PL at the highest temperature of 433 K. The blue shift of the PL peak may be due to a small amount of oxidation of the SiQD surface because the measurement was performed under an ambient atmosphere. However, it can be ignored for the photothermal applications. It might be mentioned that SiQDs are not structurally affected by changing temperature.

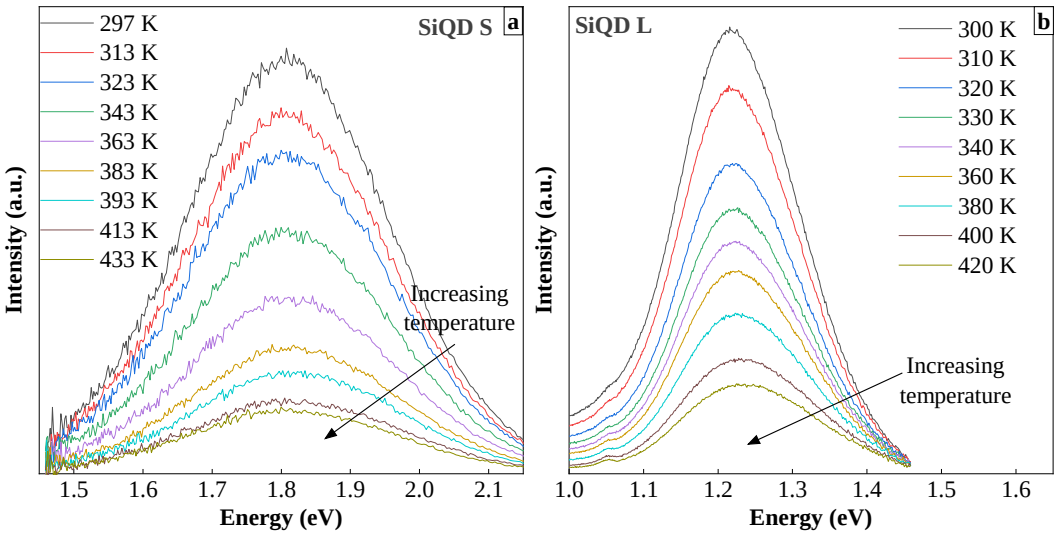

Figure 3.5. PL measurements of a) small sized, b) large sized SiQDs above room temperature

The photothermal effect in semiconductors might induce vibrational conduction of energy in the lattice via crystal structure defects and trap sites in the band structure.23 Depending on the QD size, the nonradiative channels in the structure must be considered to understand the mechanism of photothermal heating. Temperature-dependent PL spectroscopy is a conventional method to investigate the structural origin of photoexcited carrier recombination. In this study, three quartz glass substrates covered with thin films were prepared as specimens. The PL spectra were measured in the range 4.2–300 K with a strict temperature fluctuation control of ± 0.1 K. There was no apparent damage to the optical properties before and after the measurement. Figure 3.6 shows the temperature dependence of PL spectra excited at 390 nm for the three samples. Increasing the temperature induces a pronounced redshift and broadening of the PL linewidths in the PL spectra for every sample. The obtained dependencies agree well with those for QDs of semiconductors.[48-51] The integrated values of the PL intensity evolve differently between samples.

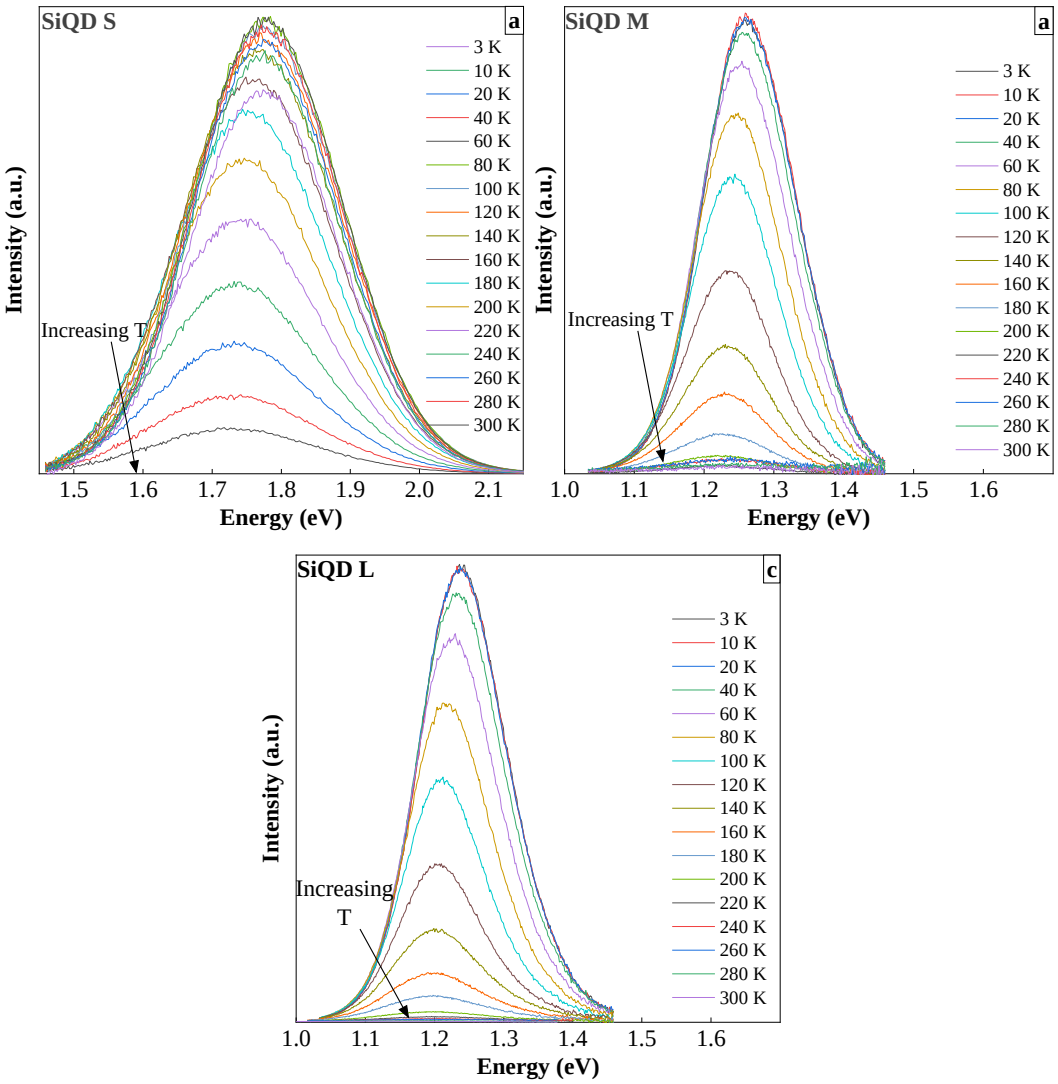

Figure 3.6. PL peak spectra observed at temperature range from 4 K to 300 K for the samples (S), (M) and (L). with a) 720 nm (S), b) 985 nm (M), c) 1035 nm room temperature PL emissions

Figure 3.7 plots the PL intensity at each monitoring temperature normalized with respect to the PL intensity value at 300 K. Clearly, all samples demonstrate a continuously decreasing trend as the temperature increases. Unlike a previous study reporting the temperature dependence of PL spectra for oxide-encapsulated SiQDs,[52] the PL intensity does not increase from 4.2 to 30 K. It has been recently established that this rise in the lowest temperature range might be due to amorphous silica on the surface of H-SiQD.[53] Thus, the

oxidation degree of our samples is too small to influence the PL properties, which is consistent with the ATR-FTIR study.

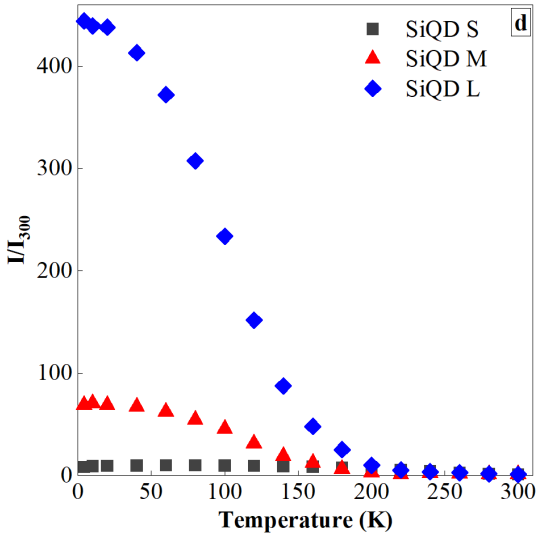

Figure 3.7. Integrated PL intensity of the samples as a function of temperature. All values of PL intensity were normalized to that of 300 K

Up to 300 K, the PL intensity decreases 10-fold, 70-fold, and 440-fold for the samples (S), (M), and (L), respectively. Such a decrease in the PL intensity is caused by the presence of nonradiative channels, which result in strong thermal quenching.[54] At low temperatures, nonradiative channels are not thermally activated. Increasing the temperature promotes nonradiative incidents such as trapping by the surface, defect or ionized impurity states as expressed by $\tau_{NR} = \tau_0 \exp(E_a/K_BT)$, where E_a is the activation energy and τ_{NR} is the nonradiative lifetime.[49] The successive decreasing behaviors of the PL intensity with the rise in temperature appear due to the thermal activation of nonradiative channels present in the H-SiQDs. The magnitude of τ_{NR} decreases with the rise in temperature as expressed by Equation 4.4:[49]

$$I(T) = I_0 / \left[1 + \alpha \times exp\left(-\frac{E_a}{kBT}\right)\right] \qquad \textbf{(3.4)}$$

where I_0 is the intensity at the lowest temperature, α is the radiative recombination rate, and k_B is the Boltzmann constant. The good fittings expressed by R^2 values higher than 0.97 (Figure 3.8) validate the curve fitting with Equation 4.4. The estimated values of the apparent

activation energy from the Arrhenius plots are 143±17, 51±5, and 42±4 meV for the samples (S), (M), and (L), respectively. The calculations suggest the presence of a relatively high density of defect states for nonradiative thermal dissipation in larger sized QDs.

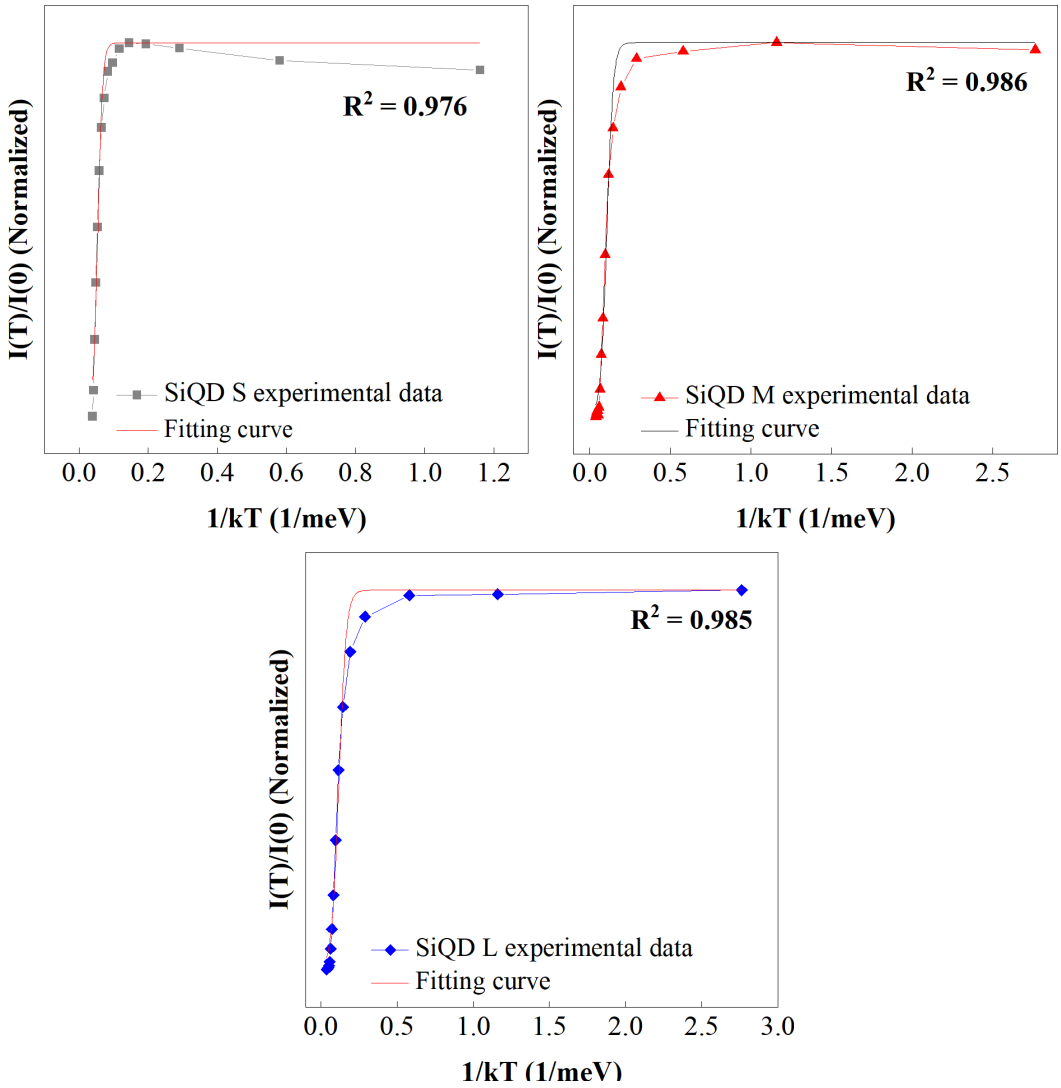

Figure 3.8. Arrhenius plot of the PL intensity for the samples (S), (M) and (L) and the fitted curves

Since the energy transfer from electrons to phonons involves the photothermal heating effect, it is unclear whether optical phonons are coupled with electrons for energy release that involves PL linewidth broadening. Figure 3.9 shows the values of full width at half-maximum (FWHM) of the PL spectra for the three different sizes as functions of temperature.

The experimental plots of the FWHM of PL spectra measured at each temperature are fitted with the relation given in Equation 4.5:[55]

$$\Gamma(T) = \Gamma_{inh} + \sigma T + \Gamma_{LO}\left\{exp\left(\frac{E_{LO}}{kBT}\right) - 1\right\}^{-1} \qquad \textbf{(3.5)}$$

where Γ_{inh} represents the inhomogeneous broadening, which is independent of temperature, σ is the acoustic phonon-electron interaction coefficient, Γ_{LO} indicates the strength of the exciton-LO-phonon coupling, and E_{LO} denotes the LO phonon energy. The spectra for all three samples tend to have narrower FWHM with decreasing temperature. For medium and large particles, FWHM starts to increase around 100–150 K and becomes saturated around 30–4.2 K. This behavior is not significant in the smallest size as the increment is small.

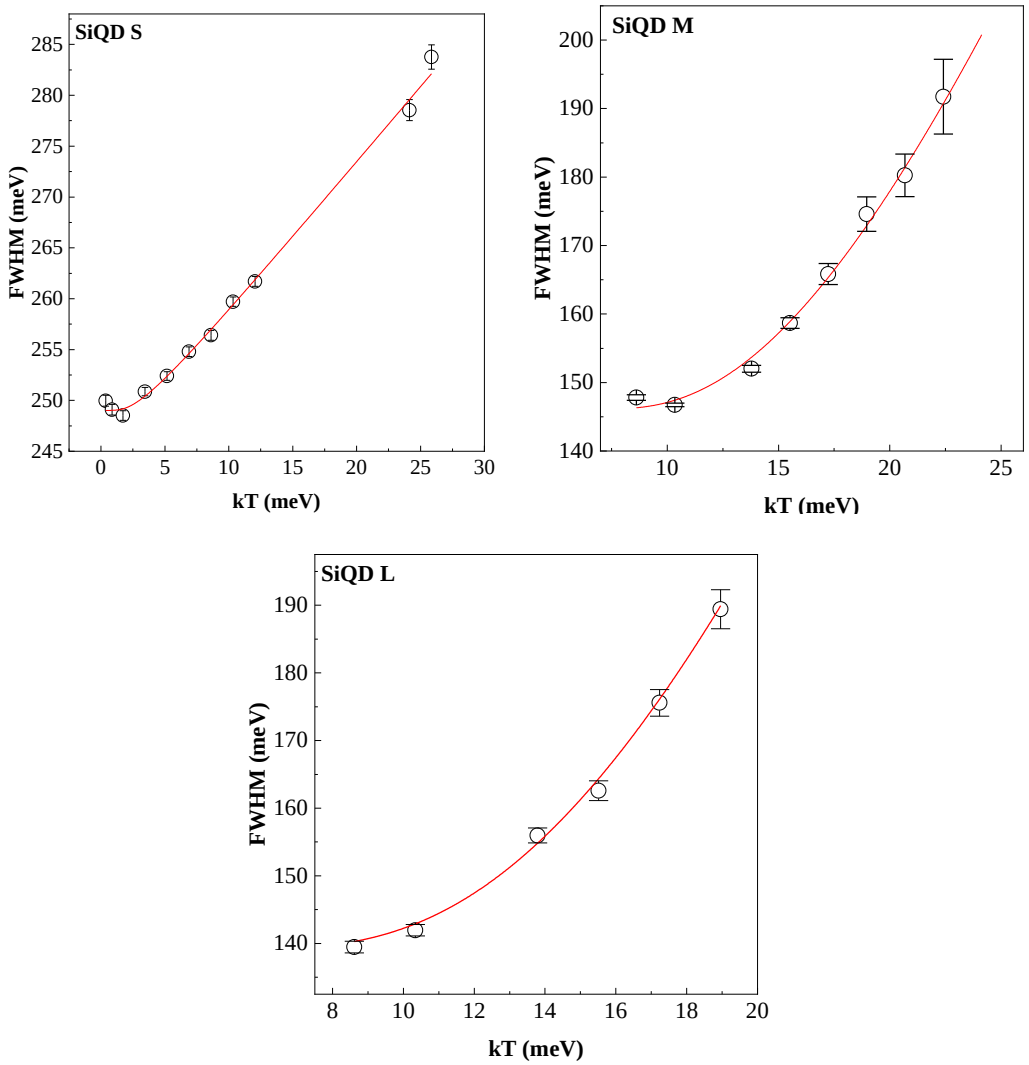

Figure 3.9. Integrated FWHM of the samples as a function of temperature

Other than this behavior, the PL spectra becomes narrower due to the restricted interaction as the temperature decreases. Table 3.2 summarizes the fitting parameters. The values obtained from the fitting for E_{LO} agree well with the reported LO phonon energy (63 meV for bulk), except that E_{LO} for the (S) sample differs from the bulk value. The numerical values suggest that the contribution to the PL linewidth broadening arises from the interaction with LO phonons for both samples (M) and (L), while there is less coupling of the carriers to acoustic phonons.

Table 3.2. Fitting parameters of temperature-dependent FWHM of the PL peaks shown in Figure 3.9

Parameter / Sample	**σ (meV/K)**	**Γ_{LO} (meV)**	**E_{LO} (meV)**	**Γ_{inh} (meV)**
H-SiQD (S)	0.012	13	9	249
H-SiQD (M)	0.001	753	65	148
H-SiQD (L)	0.01	1100	60	139

The values for Γ_{LO} increase as the QD size increases. This size-dependent behavior could be explained as follows. Photogenerated carriers such as electrons and holes are localized in a spatially limited, narrow space like a QD due to Coulombic interaction. The carriers might behave as excitons. Since the effective mass of a hole is larger than that of an electron, holes are more localized than electrons, helping the exciton produce a significant charge separation that results in a large local electric field. The electric field couples strongly to the optical phonon. The coupling is generally strengthened with an incremental size of QDs due to larger charge separation in a larger QD. The opposite might be observed for a smaller QD. Because of a better electron-hole wavefunction overlap in a smaller QD, the charge separation decreases, which weakens the exciton-phonon coupling.[56]

For more details about the large value of Γ_{LO}; the excitons and their recombination are affected by phonon (i.e., exciton-phonon interaction). The interaction is described in terms of deformation potential. Optical phonon creates the electric fields associated with thermally vibrating lattice atoms. These fields interact strongly with the electrons, holes and excitons, which in turn generate the population redistribution between vibrational sublevels of energy. This population redistribution of the carriers in the sublevels of energy induces the PL spectral broadening as well as more nonradiative pathways. In addition, the strength of the exciton-phonon coupling in phonons at various frequencies also increases the rates of nonradiative processes. The nonradiative processes may contain (i) the radiation less transitions between two energy states of the same spin state and (ii) cooling hot electrons and

holes within several picoseconds with the lattice through carrier cooling processes such as carrier–phonon scattering. For all the above processes, the excess carrier energy is dissipated into phonons.[57] According to the abovementioned scenario, the value of the exciton-LO phonon coupling is strengthened for larger QDs, increasing nonradiative recombination. Consequently, the photon energy acquired through the sequential absorption of photons under photoexcitation conditions might be converted into heat, enhancing the conversion energy for larger QDs.

To investigate about more detail of the radiative and nonradiative pathways, temperature dependence of decay dynamics of the samples were investigated (Figure 3.10a-d). Overall trends of the lifetime decay with the temperature are quite similar for all the particles. From the graph it is observed that, with decreasing temperature different nonradiative pathways activated at higher temperatures are closing down which increases the life time with decrease of temperature which is supported by the PL intensity increment with decreasing temperature. But with the careful investigation parallel with the PL intensity, difference between the three samples can be observed.

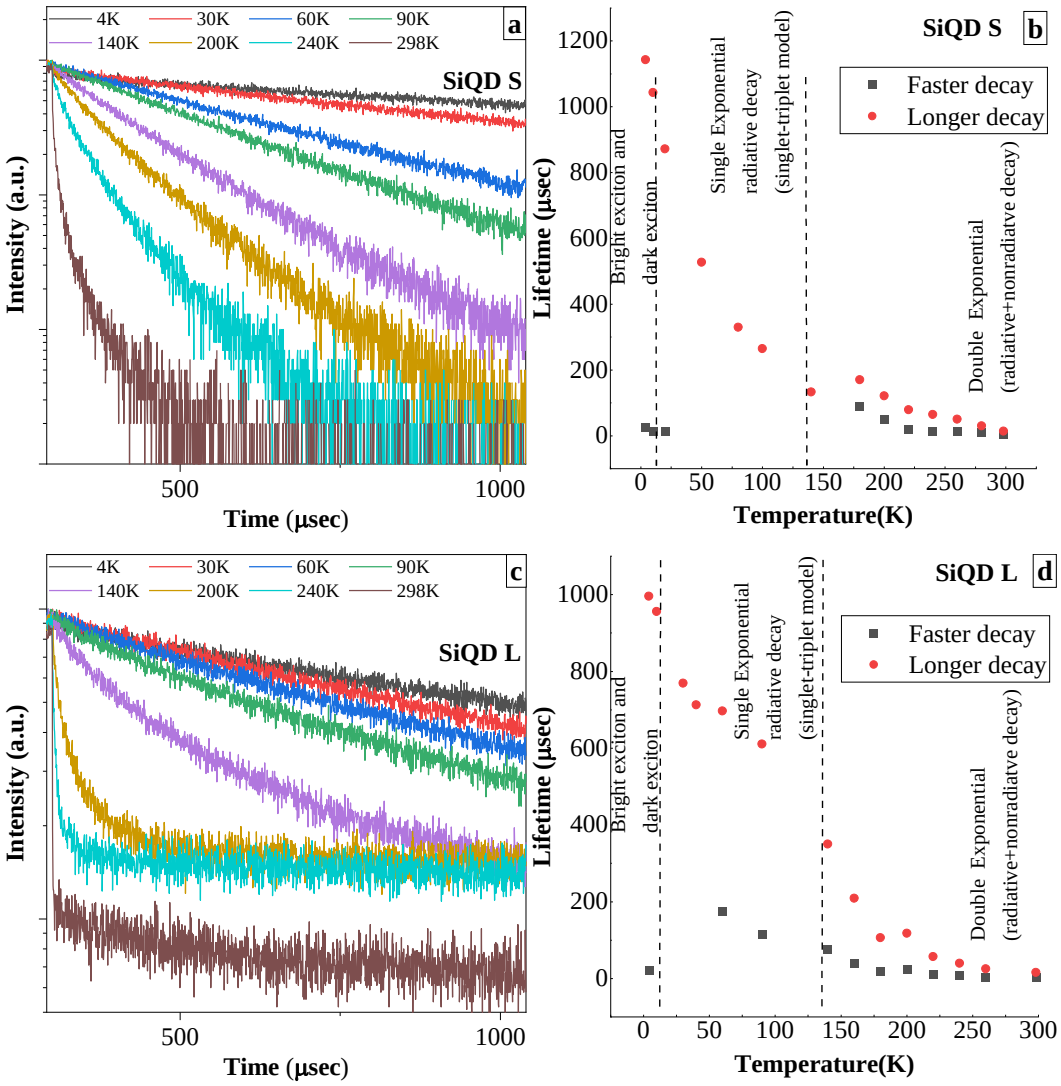

Figure 3.10. PL lifetime behavior of hydrogen terminated SiQDs with red and NIR emission

At the low temperature zone where the PL intensity is nearly constant, PL exponential decay is well fitted with single exponential decay implying the exciton decay rates corresponding to radiative decay in this temperature zone (radiative regime). The threshold temperature after which this radiative regime start (single exponential) varies with the size of the particles. For the larger particle radiative regime starts from around 60 K but as the size decreases this threshold temperature increases to around 140 K and 170 K respectively. This is quite obvious because for the larger particle quantum confinement is less so the

nonradiative pathways are more which actually quench the PL intensity at high temperature range. At really very low temperature range from 3K -10K PL decay curve is bi exponential which contains a very short lifetime decay (regardless of the size). This fast decay can be ascribed to decay between bright exciton (e-h pair with opposite spin) and dark exciton (e-h pair with parallel spin).[27] As the temperature increases to >10K, this faster component vanishes and decay becomes single exponential upto a threshold temperature which we describe as radiative regime. In this regime PL intensity do not increase, but the lifetime increases with decreasing the temperature. These phenomenon cannot be explained by nonradiative mechanism but can be explained by the singlet triplet splitting model.

According to that model, the ground state, split by energy Δ E, gives rise to an upper singlet excitonic state (spin allowed) and a lower triplet state (spin forbidden) because of the exchange interaction of electrons and holes. Triplet state is becoming populated more and more as the temperature goes down in this low temperature range. In this condition, an optical transition from the triplet state to ground state is ideally forbidden, but is slightly allowed in practice because of the spin-orbit interaction, leading to a long radiative lifetime. So in conclusion, lifetime behavior in the radiative regime can be explained by the singlet triplet model.[25, 28]

Above the threshold temperature PL intensity decreases rapidly with increasing temperature continuously up to room temperature. In this temperature regime along with the radiative relaxation process various nonradiative pathways are included and contribute in the decay dynamics. For that reason the lifetime decay cannot be fitted by single exponential but it is fitted with double exponential. Those non radiative pathways are created due to surface defects and other kind of defects. In Figure 3.10b and 9d, temperature dependence of the life time has been plotted showing the different regime for the two different size emitting red and NIR wavelength.

3.4. Conclusion

We investigated the photothermal conversion performances of three freestanding H-SiQDs with different sizes under laser illumination. The photothermal responses were

enhanced for the larger QDs. To elucidate a possible mechanism for the size dependence of the photothermal performance, we investigated the PL spectral properties as functions of temperature between 4.2 and 300 K. As the temperature increased, the emission peak energy red-shifted the PL intensity decreased, and the PL spectra became broader. Thermal activation of nonradiative channels realized decreasing trends in the PL intensity. Arrhenius plots with the fits for the PL reduction behaviors gave activation energies of 143±17, 51±5, and 42±4 meV, suggesting the presence of a relatively high density of defect states for nonradiative thermal dissipation for larger QDs. The temperature dependence of PL FWHM also supported that the phonon heat dissipation is enhanced for larger QDs. The broadening of the PL linewidth with temperature might be due to the coupling of the electron-hole pairs with optical phonons. Controlling the nonradiative channels allows surgeons and medical/healthcare professions to manipulate the photothermal heating in a relatively lower temperature range, contributing to the development of a therapeutic thermal-phononics.

3.5. References

(1) Cui, M.; Liu, S.; Song, B.; Guo, D.; Wang, J.; Hu, G.; Su, Y.; He, Y. Fluorescent Silicon Nanorods-Based Nanotheranostic Agents for Multimodal Imaging-Guided Photothermal Therapy. *Nano-Micro Letters* **2019**, *11* (1), 73. DOI: 10.1007/s40820-019-0306-9.

(2) Gupta, R.; Xiong, Q.; Adu, C. K.; Kim, U. J.; Eklund, P. C. Laser-Induced Fano Resonance Scattering in Silicon Nanowires. *Nano Letters* **2003**, *3* (5), 627-631. DOI: 10.1021/nl0341133.

(3) Wang, N.; Yao, B. D.; Chan, Y. F.; Zhang, X. Y. Enhanced Photothermal Effect in Si Nanowires. *Nano Letters* **2003**, *3* (4), 475-477. DOI: 10.1021/nl034019m.

(4) Roder, P. B.; Manandhar, S.; Smith, B. E.; Zhou, X.; Shutthanandan, V. S.; Pauzauskie, P. J. Photothermal Superheating of Water with Ion-Implanted Silicon Nanowires. *Advanced Optical Materials* **2015**, *3* (10), 1362-1367. DOI: 10.1002/adom.201500143 (acccessed 2020/04/20).

(5) Duan, Y.; Kong, J. F.; Shen, W. Z. Raman investigation of silicon nanocrystals: quantum confinement and laser-induced thermal effects. *Journal of Raman Spectroscopy* **2012**, *43* (6), 756-760. DOI: 10.1002/jrs.3094 (acccessed 2020/04/20).

(6) Adikaari, A. A. D. T.; Silva, S. R. P. Thickness dependence of properties of excimer laser crystallized nano-polycrystalline silicon. *Journal of Applied Physics* **2005**, *97* (11), 114305. DOI: 10.1063/1.1898444.

(7) Ishii, S.; Sugavaneshwar, R. P.; Chen, K.; Dao, T. D.; Nagao, T. Solar water heating and vaporization with silicon nanoparticles at mie resonances. *Opt. Mater. Express* **2016**, *6* (2), 640-648. DOI: 10.1364/OME.6.000640.

(8) Regli, S.; Kelly, J. A.; Shukaliak, A. M.; Veinot, J. G. C. Photothermal Response of Photoluminescent Silicon Nanocrystals. *The Journal of Physical Chemistry Letters* **2012**, *3* (13), 1793-1797. DOI: 10.1021/jz3004766.

(9) Sun, W.; Zhong, G.; Kübel, C.; Jelle, A. A.; Qian, C.; Wang, L.; Ebrahimi, M.; Reyes, L. M.; Helmy, A. S.; Ozin, G. A. Size-Tunable Photothermal Germanium Nanocrystals. *Angewandte Chemie International Edition* **2017**, *56* (22), 6329-6334. DOI: 10.1002/anie.201701321.

(10) Han, L.; Zeman, M.; Smets, A. H. M. Raman study of laser-induced heating effects in free-standing silicon nanocrystals. *Nanoscale* **2015**, *7* (18), 8389-8397, 10.1039/C5NR00468C. DOI: 10.1039/C5NR00468C.

(11) Chinnathambi, S.; Shirahata, N. Recent advances on fluorescent biomarkers of near-infrared quantum dots for in vitro and in vivo imaging. *Science and Technology of Advanced Materials* **2019**, *20* (1), 337-355. DOI: 10.1080/14686996.2019.1590731.

(12) Erogbogbo, F.; Chang, C.-W.; May, J. L.; Liu, L.; Kumar, R.; Law, W.-C.; Ding, H.; Yong, K. T.; Roy, I.; Sheshadri, M.; et al. Bioconjugation of luminescent silicon quantum dots to gadolinium ions for bioimaging applications. *Nanoscale* **2012**, *4* (17), 5483-5489, 10.1039/C2NR31002C. DOI: 10.1039/C2NR31002C.

(13) Dohnalová, K.; Poddubny, A. N.; Prokofiev, A. A.; de Boer, W. D. A. M.; Umesh, C. P.; Paulusse, J. M. J.; Zuilhof, H.; Gregorkiewicz, T. Surface brightens up Si quantum dots:

direct bandgap-like size-tunable emission. *Light: Science & Applications* **2013**, *2* (1), e47-e47. DOI: 10.1038/lsa.2013.3.

(14) Chinnathambi, S.; Karthikeyan, S.; Hanagata, N.; Shirahata, N. Molecular interaction of silicon quantum dot micelles with plasma proteins: hemoglobin and thrombin. *RSC Advances* **2019**, *9* (26), 14928-14936, 10.1039/C9RA02829C. DOI: 10.1039/C9RA02829C.

(15) Hessel, C. M.; Reid, D.; Panthani, M. G.; Rasch, M. R.; Goodfellow, B. W.; Wei, J.; Fujii, H.; Akhavan, V.; Korgel, B. A. Synthesis of Ligand-Stabilized Silicon Nanocrystals with Size-Dependent Photoluminescence Spanning Visible to Near-Infrared Wavelengths. *Chemistry of Materials* **2012**, *24* (2), 393-401. DOI: 10.1021/cm2032866.

(16) Hemmer, E.; Benayas, A.; Légaré, F.; Vetrone, F. Exploiting the biological windows: current perspectives on fluorescent bioprobes emitting above 1000 nm. *Nanoscale Horizons* **2016**, *1* (3), 168-184, 10.1039/C5NH00073D. DOI: 10.1039/C5NH00073D.

(17) Michalak, D. J.; Amy, S. R.; Aureau, D.; Dai, M.; Estève, A.; Chabal, Y. J. Nanopatterning Si(111) surfaces as a selective surface-chemistry route. *Nature Materials* **2010**, *9* (3), 266-271. DOI: 10.1038/nmat2611.

(18) Holm, J.; Roberts, J. T. Surface Chemistry of Aerosolized Silicon Nanoparticles: Evolution and Desorption of Hydrogen from 6-nm Diameter Particles. *Journal of the American Chemical Society* **2007**, *129* (9), 2496-2503. DOI: 10.1021/ja0658970.

(19) Booth, M.; Brown, A. P.; Evans, S. D.; Critchley, K. Determining the Concentration of CuInS2 Quantum Dots from the Size-Dependent Molar Extinction Coefficient. *Chemistry of Materials* **2012**, *24* (11), 2064-2070. DOI: 10.1021/cm300227b.

(20) Xia, C.; Wu, W.; Yu, T.; Xie, X.; van Oversteeg, C.; Gerritsen, H. C.; de Mello Donega, C. Size-Dependent Band-Gap and Molar Absorption Coefficients of Colloidal CuInS2 Quantum Dots. *ACS Nano* **2018**, *12* (8), 8350-8361. DOI: 10.1021/acsnano.8b03641.

(21) Xie, R.; Peng, X. Synthetic Scheme for High-Quality InAs Nanocrystals Based on Self-Focusing and One-Pot Synthesis of InAs-Based Core–Shell Nanocrystals. *Angewandte Chemie International Edition* **2008**, *47* (40), 7677-7680. DOI: https://doi.org/10.1002/anie.200802867.

(22) Castro, H. P. S.; Pereira, M. K.; Ferreira, V. C.; Hickmann, J. M.; Correia, R. R. B. Optical characterization of carbon quantum dots in colloidal suspensions. *Opt. Mater. Express* **2017**, *7* (2), 401-408. DOI: 10.1364/OME.7.000401.

(23) de Mello Donegá, C.; Koole, R. Size Dependence of the Spontaneous Emission Rate and Absorption Cross Section of CdSe and CdTe Quantum Dots. *The Journal of Physical Chemistry C* **2009**, *113* (16), 6511-6520. DOI: 10.1021/jp811329r.

(24) Chandra, S.; Ghosh, B.; Beaune, G.; Nagarajan, U.; Yasui, T.; Nakamura, J.; Tsuruoka, T.; Baba, Y.; Shirahata, N.; Winnik, F. M. Functional double-shelled silicon nanocrystals for two-photon fluorescence cell imaging: spectral evolution and tuning. *Nanoscale* **2016**, *8* (16), 9009-9019, 10.1039/C6NR01437B. DOI: 10.1039/C6NR01437B.

(25) Kovalev, D.; Heckler, H.; Polisski, G.; Koch, F. Optical Properties of Si Nanocrystals. *physica status solidi (b)* **1999**, *215* (2), 871-932. DOI: https://doi.org/10.1002/(SICI)1521-3951(199910)215:2<871::AID-PSSB871>3.0.CO;2-9.

(26) Valenta, J.; Greben, M.; Remeš, Z.; Gutsch, S.; Hiller, D.; Zacharias, M. Determination of absorption cross-section of Si nanocrystals by two independent methods based on either absorption or luminescence. *Applied Physics Letters* **2016**, *108* (2), 023102. DOI: 10.1063/1.4939699.

(27) de Mello Donegá, C.; Bode, M.; Meijerink, A. Size- and temperature-dependence of exciton lifetimes in CdSe quantum dots. *Physical Review B* **2006**, *74* (8), 085320. DOI: 10.1103/PhysRevB.74.085320.

(28) Ghosh, B.; Takeguchi, M.; Nakamura, J.; Nemoto, Y.; Hamaoka, T.; Chandra, S.; Shirahata, N. Origin of the Photoluminescence Quantum Yields Enhanced by Alkane-Termination of Freestanding Silicon Nanocrystals: Temperature-Dependence of Optical Properties. *Scientific Reports* **2016**, *6* (1), 36951. DOI: 10.1038/srep36951.

Chapter 4: Photothermal Performance of Silicon Quantum Dots in Aqueous Media and in-vitro

4.1. Introduction

Use of nanostructures as photothermal conversion agents for photothermal cancer therapy applications have gained great interest due to enabling minimal damage to healthy tissue with effective localized heating of tumor.[1] Currently used nanostructures as photothermal therapy agents are mostly metallic that has strong optical absorption in NIR region originating from surface plasmon resonance.[2, 3] Nonetheless, the concerns on their toxicity limits their use.[4] As shown experimentally in Chapter 4 and literature,[5, 6] Si has controllable photothermal effect When considered their good photostability, low toxicity and good PLQY, being able to correspond from photothermal response arising from their nonradiative nature may expand use of SiQDs to theranostics. It has been shown that porous Si can be used as photothermal therapy agent yet there is no report on SiQDs within our knowledge. Therefore, proven controllable photothermal response of SiQDs should be tracked to aqueous media to live cell environment.

In this chapter, photothermal effect of UA:SiQDs in aqueous media is investigated. Performance of photothermal conversion was evaluated by calculation of photothermal conversion efficiency and comparision with other QDs. Photothermal performance of UA:SiQDs was also demonstrated in vitro.

4.2. Experimental procedure

4.2.1. Photothermal performance of SiQDs in aqueous media

Photothermal warming of water was examined using UA:SiQD-S and UA:SiQD-L samples. The samples adjusted at the same concentration (3.1 mg/mL) were separately stirred in 10 mm standard quartz cuvettes of 2.5 mL Milli-Q water of pH 7. Temperature of the QD solution was measured using a K-type thermocouple with a datalogger. After the temperature of the QD solution becomes constant, the QD solution was irradiated for 20 min with the

Nd:YAG laser (Surelite II-10 SN, Amplitude Japan Co. Ltd). The laser operation conditions were a 532 nm laser beam with a diameter of Φ7 mm, a photon power of 960 mW, and a repetition rate of 10 Hz. The temperature was measured at every 10 s. Without QDs, the temperature of 2.5 mL Milli-Q water increased by 0.5 °C during 20 min under the same irradiation conditions. The photon power was measured with a thermal power/energy laser measurement sensor (10A-P, Ophir Optronics Solutions Ltd).

4.2.2. Calculation of photothermal conversion efficiency

Photothermal response of small and large sized UA:SiQDs in aqueous media was observed. 1.5 mL of 1 mg/mL SiQD-water solution was stirred in a quartz cuvette and temperature change was measured using a K-type thermocouple with a datalogger. After the temperature of solution no longer increases due to stirring, solution was irradiated by Nd:YAG laser (Surelite II-10 SN, Amplitude Japan Co. Ltd) with 532 nm laser beam with 7 mm diameter and 10 Hz repetition rate. Photon power absorbed by solution was determined by using thermal power/energy laser measurement sensor (10A-P, Ophir Optronics Solutions Ltd). After saturation of temperature value, laser irradiation was stopped and cooling was also recorded. Under same irradiation conditions, temperature change of water without SiQDs was recorded. Photothermal conversion efficiency, η, was calculated by using Equation 4:[7]

$$\eta = \frac{hA(T_{max} - T_{surr}) - Q_{dis}}{I(1 - 10^{-A_{532}})} \qquad \textbf{(4.1)}$$

where h is the heat transfer coefficient, A is the surface area of container, T_{max} is the maximum equilibrium temperature, T_{surr} is the surrounding temperature, I is the laser power, A_{532} is the absorbance value of solution at 532 nm.

4.2.3. In-vitro photothermal performance of UA:SiQDs

Photothermal performance of small sized UA:SiQDs inside the HeLa cells was also demonstrated. Scheme of the experimental setup can be found in Figure 4.1 below:

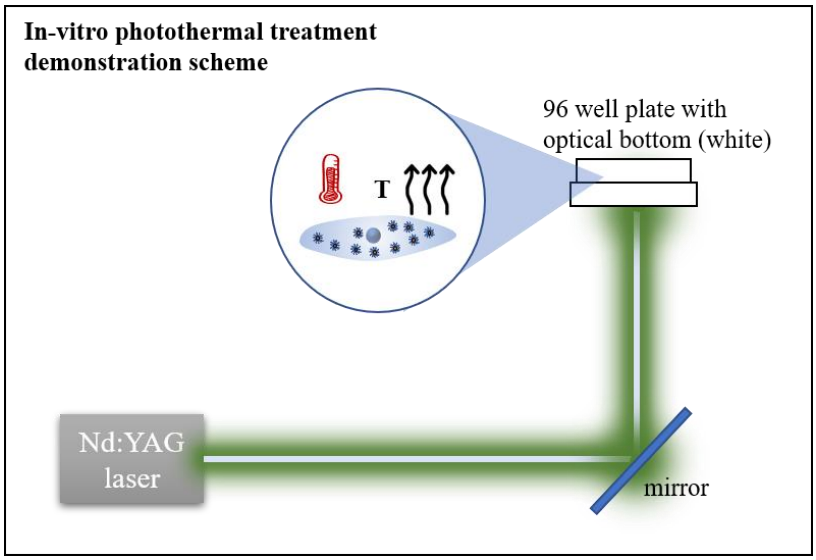

Figure 4.1. In-vitro photothermal treatment setup scheme

HeLa cells were seeded into optical glass bottom 96 well plates (Nunc™, Microwell™ with white superstructure) at a cell density 15,000 cells/well (150,000 cells/ml, 100 µL). After 24 hours incubation, media of part of the wells were changed to new medium containing 50 µg/mL of SiQD and then incubated for further 24 hours. Before irradiation, cells were washed with 200 µL of PBS for 4 times and 100 µL of MEM without phenol red supplemented with 10% FBS was added. Each well was observed under optical microscope. Cells with and without SiQDs were irradiated by Nd:YAG laser at 532 nm wavelength, 130 mW power and 12 mm diameter for 10 minutes. After irradiation, cells were observed under optical microscope and compared to previous observation.

4.3. Results and discussion

Photothermal response of SiQDs were investigated to prove our claim for their theranostic use. Firstly, 1 mg/mL aqueous solutions of water soluble SiQDs were irradiated by 532 nm laser and temperature change was recorded. Incident laser power 980 mW and power absorbed by solution was 450 mW. This experiment was done by using SiQDs with two different sizes. Figure 4.2 shows temperature change by irradiation of each sample.

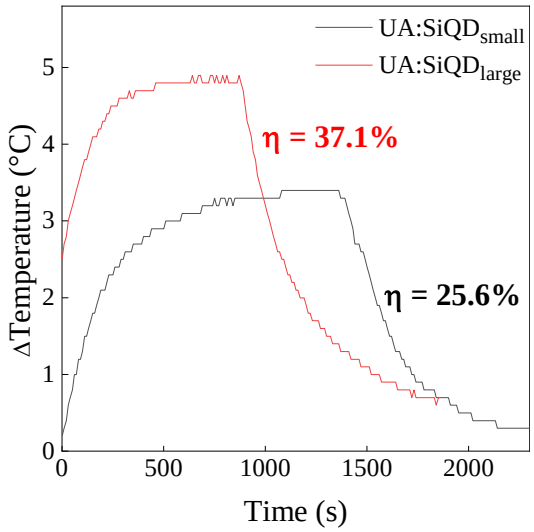

Figure 4.2. Temperature increment quantity (ΔT) of 2.5 mL of water containing UA-SiQD (S) and UA-SiQD(L) of 3.1 mg/mL under 532 nm Nd:YAG pulse laser irradiation.

Higher temperature increase was observed for large size SiQDs. Being different from metallic nanoparticles, photothermal conversion in semiconductor QDs are originated from defects and trap sites that undergo nonradiative recombination[8]. With increasing size, rate of nonradiative recombination occurs increases and therefore, higher temperature increase is observed[9]. In parallel with temperature changes, photothermal conversion efficiencies of small and large size UA:SiQDs were calculated as to be 25.1% and 37.1%, respectively. This result implies that sufficient photothermal conversion could be tuned by changing the particle size. In such a case, concentration dependent cytotoxicity of large sized SiQDs should be addressed. Obtained photothermal conversion efficiency value is comparable with other study on black phosphorus Si, 33.6%[10] and other nanostructures (Au nanoshell 13% and Au nanorod 21%[7], CuSe 21%[7], Fe/Fe_3O_4, 20.3%[11], black phosphorus QD 24.8%[12], Bi_2S_3 28.1%[13], CdTe 14%[14]) are considered to have potential as photothermal applications.

PL wavelength of water soluble SiQDs indicate that diameter of SiQD S and SiQD L decreased during hydrosilylation. Size dependent photothermal response of SiQDs was also demonstrated in aqueous media. PLQY of both sample remained the same after irradiation which indicates no laser ablation occurred (Table 4.1). Temperature of water could be increased by laser heating of SiQDs by 3.3 and 10.4 °C for undecanoic acid terminated SiQD

S and SiQD L (SiQD S-UA and SiQD L-UA), respectively (Figure 4). While it is known that surface properties and media is also effective on generated heat, similar study done with 1-dodecene terminated SiQDs in toluene obtained 25 °C heating by 2.9 mg/mL concentration for 4 nm particle size.[15]

Table 4.1. PL and PLQY of water soluble SiQDs after hydrosilylation and after irradiation

Sample	PL (nm)			PLQY (%)	
	Before hydrosilylation	After Hydrosilylation (before irradiation)	After irradiation	Before irradiation	After irradiation
UA-SiQD S	720	630	628	19	15
UA-SiQD L	1035	907	905	13	13

Table 4.2 shows similar studies done by using gold nanoparticles in water media. In this condition, similar temperature change can be obtained by gold nanoparticles that are as big as 25 nm and/or having nonspherical shapes which may have toxic effects in the body. We expect that Si QDs can be joined in a family of possible NPs for photothermal therapeutic applications because the necessary temperature increase could be achieved.[16-18]

Table 4.2. Comparision of results with gold nanoparticles

Material	Particle Size	ΔT	Ref
SiQD S	2.2	3	This work
SiQD L	4.8	10	
Au nanosphere	25	3	[19]
Au nanosphere	40	8	
Au nanourchin	25	8	
Au nanourchin	45	21	
Au nanorod	56.9/13.9 (length/diameter)	5	[20]

In Figure 4.3, optical microscopy images belong to control cells, cells with 50 μg/mL and 400 μg/mL SiQDs are shown. There is no significant change in cell morphology after UA:SiQD uptake. Images on the right column represent the situation of the wells after laser irradiation. Cells without SiQDs remained same after irradiation while a significantly noticeable decrease in the cell number observed for the irradiated cells with SiQDs in proportion with concentration. The Hela cells that uptake the UA:SiQDs detached from the glass substrate. A few cells remaining on the glass surface have also change their morphology to round and lost their adhesive ability.

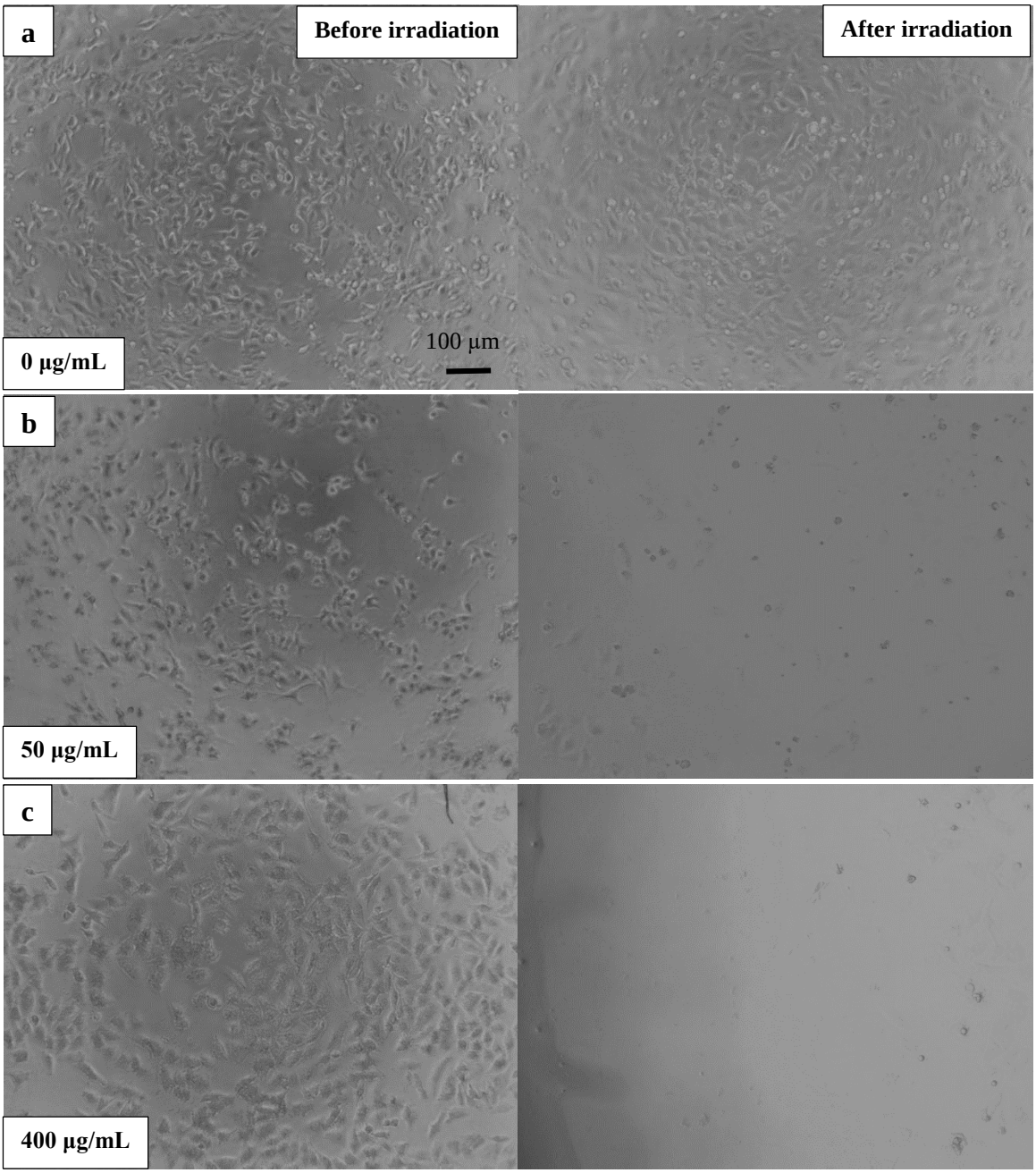

Figure 4.3. Observation of HeLa cells before and after laser irradiation: a) HeLa cells without UA:SiQDs, HeLa cells with b) 50 μg/mL and c) 400 μg/mL UA:SiQDs. Scale bar is same for each image.

This results indicate that UA:SiQDs can be effectively used for photothermal therapy. Similar study has been performed with PEGylated Au decorated Si nanowires

(AuNPs@SiNWs).[21] Although power and wavelength of applied laser is different due to PEGylation and including Au, it has been shown that cell death could be provided depending on the concentration and duration of laser exposure. As mentioned previously, in spite of limited number of studies on photothermal therapy applications of Si nanostructures, all of them reports the efficiency of using Si as phototherapy agents.[21-23]

4.4. Conclusion

In this chapter, prepared highly stable water soluble SiQDs with undecanoic acid functionalization were investigated by means of their photothermal performance. UA:SiQDs have PL emission that can be traced at least for 18 days. They show no acute toxicity and cells show about 50% viability at 50 μg/mL after 14 days. They show good photothermal performance in aqueous media with 25.1% photothermal conversion efficiency that can be tuned by SiQD size. Concentration dependent cell death caused by photothermal UA:SiQDs was observed by demonstration of laser heating in-vitro. As to summarize, we think that SiQDs may be used as photothermal therapy agents provide cell death by photothermal heating.

4.5. References

(1) Sieval, A.; Demirel, A.; Nissink, J.; Linford, M.; Van der Maas, J.; De Jeu, W.; Zuilhof, H.; Sudhölter, E. Highly stable Si− C linked functionalized monolayers on the silicon (100) surface. *Langmuir* **1998**, *14* (7), 1759-1768.

(2) Zharov, V. P.; Mercer, K. E.; Galitovskaya, E. N.; Smeltzer, M. S. Photothermal nanotherapeutics and nanodiagnostics for selective killing of bacteria targeted with gold nanoparticles. *Biophysical journal* **2006**, *90* (2), 619-627. DOI: 10.1529/biophysj.105.061895 From NLM.

(3) Jain, P. K.; Huang, X.; El-Sayed, I. H.; El-Sayed, M. A. Noble Metals on the Nanoscale: Optical and Photothermal Properties and Some Applications in Imaging, Sensing, Biology, and Medicine. *Accounts of Chemical Research* **2008**, *41* (12), 1578-1586. DOI: 10.1021/ar7002804.

(4) Alkilany, A. M.; Nagaria, P. K.; Hexel, C. R.; Shaw, T. J.; Murphy, C. J.; Wyatt, M. D. Cellular uptake and cytotoxicity of gold nanorods: molecular origin of cytotoxicity and surface effects. *Small (Weinheim an der Bergstrasse, Germany)* **2009**, *5* (6), 701-708. DOI: 10.1002/smll.200801546 From NLM.

(5) Wang, N.; Yao, B. D.; Chan, Y. F.; Zhang, X. Y. Enhanced Photothermal Effect in Si Nanowires. *Nano Letters* **2003**, *3* (4), 475-477. DOI: 10.1021/nl034019m.

(6) Lee, C.; Kim, H.; Hong, C.; Kim, M.; Hong, S. S.; Lee, D. H.; Lee, W. I. Porous silicon as an agent for cancer thermotherapy based on near-infrared light irradiation. *Journal of Materials Chemistry* **2008**, *18* (40), 4790-4795, 10.1039/B808500E. DOI: 10.1039/B808500E.

(7) Hessel, C. M.; Pattani, V. P.; Rasch, M.; Panthani, M. G.; Koo, B.; Tunnell, J. W.; Korgel, B. A. Copper Selenide Nanocrystals for Photothermal Therapy. *Nano Letters* **2011**, *11* (6), 2560-2566. DOI: 10.1021/nl201400z.

(8) Gärtner, W. W. Photothermal Effect in Semiconductors. *Physical Review* **1961**, *122* (2), 419-424. DOI: 10.1103/PhysRev.122.419.

(9) Özbilgin, İ. N. G.; Ghosh, B.; Yamada, H.; Shirahata, N. Size-Dependent Photothermal Performance of Silicon Quantum Dots. *The Journal of Physical Chemistry C* **2021**, *125* (6), 3421-3431. DOI: 10.1021/acs.jpcc.0c10027.

(10) Xu, W.; Tamarov, K.; Fan, L.; Granroth, S.; Rantanen, J.; Nissinen, T.; Peräniemi, S.; Uski, O.; Hirvonen, M.-R.; Lehto, V.-P. Scalable Synthesis of Biodegradable Black Mesoporous Silicon Nanoparticles for Highly Efficient Photothermal Therapy. *ACS Applied Materials & Interfaces* **2018**, *10* (28), 23529-23538. DOI: 10.1021/acsami.8b04557.

(11) Zhou, Z.; Sun, Y.; Shen, J.; Wei, J.; Yu, C.; Kong, B.; Liu, W.; Yang, H.; Yang, S.; Wang, W. Iron/iron oxide core/shell nanoparticles for magnetic targeting MRI and near-infrared photothermal therapy. *Biomaterials* **2014**, *35* (26), 7470-7478. DOI: https://doi.org/10.1016/j.biomaterials.2014.04.063.

(12) Sun, Z.; Xie, H.; Tang, S.; Yu, X. F.; Guo, Z.; Shao, J.; Zhang, H.; Huang, H.; Wang, H.; Chu, P. K. Ultrasmall Black Phosphorus Quantum Dots: Synthesis and Use as Photothermal Agents. *Angewandte Chemie (International ed. in English)* **2015**, *54* (39), 11526-11530. DOI: 10.1002/anie.201506154 From NLM.

(13) Liu, J.; Zheng, X.; Yan, L.; Zhou, L.; Tian, G.; Yin, W.; Wang, L.; Liu, Y.; Hu, Z.; Gu, Z.; et al. Bismuth Sulfide Nanorods as a Precision Nanomedicine for in Vivo Multimodal Imaging-Guided Photothermal Therapy of Tumor. *ACS Nano* **2015**, *9* (1), 696-707. DOI: 10.1021/nn506137n.

(14) Chu, M.; Pan, X.; Zhang, D.; Wu, Q.; Peng, J.; Hai, W. The therapeutic efficacy of CdTe and CdSe quantum dots for photothermal cancer therapy. *Biomaterials* **2012**, *33* (29), 7071-7083. DOI: https://doi.org/10.1016/j.biomaterials.2012.06.062.

(15) Regli, S.; Kelly, J. A.; Shukaliak, A. M.; Veinot, J. G. C. Photothermal Response of Photoluminescent Silicon Nanocrystals. *The Journal of Physical Chemistry Letters* **2012**, *3* (13), 1793-1797. DOI: 10.1021/jz3004766.

(16) Kim, M.; Lee, J.-H.; Nam, J.-M. Plasmonic Photothermal Nanoparticles for Biomedical Applications. *Advanced Science* **2019**, *6* (17), 1900471. DOI: https://doi.org/10.1002/advs.201900471.

(17) Estelrich, J.; Busquets, M. A. Iron Oxide Nanoparticles in Photothermal Therapy. *Molecules* **2018**, *23* (7), 1567.

(18) Vines, J. B.; Yoon, J.-H.; Ryu, N.-E.; Lim, D.-J.; Park, H. Gold Nanoparticles for Photothermal Cancer Therapy. *Frontiers in Chemistry* **2019**, *7* (167), Review. DOI: 10.3389/fchem.2019.00167.

(19) Moustaoui, H.; Saber, J.; Djeddi, I.; Liu, Q.; Diallo, A. T.; Spadavecchia, J.; Lamy de la Chapelle, M.; Djaker, N. Shape and Size Effect on Photothermal Heat Elevation of Gold Nanoparticles: Absorption Coefficient Experimental Measurement of Spherical and Urchin-Shaped Gold Nanoparticles. *The Journal of Physical Chemistry C* **2019**, *123* (28), 17548-17554. DOI: 10.1021/acs.jpcc.9b03122.

(20) Wang, X.; Li, G.; Ding, Y.; Sun, S. Understanding the photothermal effect of gold nanostars and nanorods for biomedical applications. *RSC Advances* **2014**, *4* (57), 30375-30383, 10.1039/C4RA02978J. DOI: 10.1039/C4RA02978J.

(21) Su, Y.; Wei, X.; Peng, F.; Zhong, Y.; Lu, Y.; Su, S.; Xu, T.; Lee, S.-T.; He, Y. Gold Nanoparticles-Decorated Silicon Nanowires as Highly Efficient Near-Infrared Hyperthermia Agents for Cancer Cells Destruction. *Nano Letters* **2012**, *12* (4), 1845-1850. DOI: 10.1021/nl204203t.

(22) Shen, H.; You, J.; Zhang, G.; Ziemys, A.; Li, Q.; Bai, L.; Deng, X.; Erm, D. R.; Liu, X.; Li, C.; et al. Cooperative, nanoparticle-enabled thermal therapy of breast cancer. *Advanced healthcare materials* **2012**, *1* (1), 84-89. DOI: 10.1002/adhm.201100005 From NLM.

(23) Park, G.-S.; Kwon, H.; Kwak, D. W.; Park, S. Y.; Kim, M.; Lee, J.-H.; Han, H.; Heo, S.; Li, X. S.; Lee, J. H.; et al. Full Surface Embedding of Gold Clusters on Silicon Nanowires for Efficient Capture and Photothermal Therapy of Circulating Tumor Cells. *Nano Letters* **2012**, *12* (3), 1638-1642. DOI: 10.1021/nl2045759.

Chapter 5: Investigation of Silicon Quantum Dots for Bioimaging

5.1. Introduction

Si based nanomaterials can easily degrade into renal clearable molecules and be removed from the body without any toxic effect[1, 2] which is the biggest concern for counterparts. Together with this, ultra-small size Si (3-10 nm) has already been approved by Food and Drug Administration (FDA) as an investigational drug for clinical trials.[3] Therefore, the studies on bioapplications of SiQDs become more popular. Investigation of toxic effects of SiQDs may enable us to monitor tumor growth as well as tracking the therapeutic effect.[4-6] It may also provide photothermal therapy with minimum requirement of SiQD intake in the treatment sessions. SiQDs have been shown to have very good photostability[7, 8], for instance, no change in fluorescence intensity observed after 60 min irradiation by 488 nm confocal microscopy laser to 2.2 nm Si nanoparticles (Si NPs) inside HeLa cells.[9] In the same work, Cd containing counterparts were shown to lose fluorescence after 180 min UV irradiation while SiNPs were still stable. Whereas, it is unknown how toxic they become in the long term staying in physiological environment.

In this chapter, performance of synthesized SiQDs for bioimaging is observed. Cell uptake and toxicity studies are performed. Stability of SiQDs in HeLa cervical cancer cells and toxic effects in the long term was observed.

5.2. Experimental procedure

UA:SiQDs were prepared as described in Chapter 3. MEM-UA:SiQD samples were prepared by gradual solvent changing from ethanol to MEM. Optical properties of MEM-UA:SiQDs were observed by absorption, PL and PLQY measurements. Cell uptake and time dependent stability studies were analyzed by confocal microscopy and cytotoxicity tests were carried out up to 14 days. In this section, details of characterization techniques different than that of Chapter 2 is explained.

5.2.1. Characterization

The UA:SiQDs dispersed in water or MEM were prepared for characterization of optical properties. Optical absorption properties of water-UA:SiQD and MEM-UA:SiQD solutions were examined in visible range by using JASCO V-650 UV-Visible spectrometer.

Interaction of UA:SiQDs with live cells was observed using HeLa cell. Hela cells were cultured in MEM supplemented with 10% fatal bovine serum (FBS), 100 U/mL penicillin/100 μg/mL streptomycin in a humidified incubator with 5% CO_2 at 37 ˚C.

For photostability and cellular uptake was examined by confocal microscopy (Leica TCS SP5, Germany), 500 μL of HeLa cells in MEM solution at a cell density of 35,000 cells/mL were seeded into 4-chamber 35 mm glass bottom dishes. After 24 hours incubation, cell culture media was changed to new culture medium containing 100 μg/mL of SiQD-MEM solution. After 24 hours incubation, cells were washed thrice with phosphate buffered saline (PBS) and then fixed in 3.7% paraformaldehyde solution. For the DAPI-stained samples, fixed cells were incubated with 1 ng/mL DAPI solution for 15 minutes at room temperaure in the dark. After incubation, cells were washed with PBS. Prepared dishes were examined under confocal microscope (TS\CS SO5 II, Leica, Germany) at the days between 1^{st} - 18^{th} days under same imaging conditions (excitation at 380 nm in UV laser, detection between 600-700 nm range). Control cells without SiQDs treatment were also observed to eliminate the errors by autofluorescence.

Cell viability of HeLa cells in SiQD solutions were analyzed by Cell Counting Kit-8 (CCK-8, Dojin, Kumamoto, Japan). HeLa cells were seeded into 96 well plates at a cell density 15,000 cells/well (150,000 cells/ml, 100 μL) and incubated for 24 hours. Six identical wells were prepared for each concentration. Cell media was replaced with a new medium containing SiQD with different concentrations from 12 μg/mL to 500 μg/mL. After 24 hours of incubation, 10 μL of CCK-8 solution was added into wells and then absorbance of 450 nm was measured by microplate reader (MTP-880, Corona, Japan). Long term effect of SiQDs on HeLa cells were also investigated using Mytomicyn C treated cells. For Mitomicyn C treatment, growth medium of prepared HeLa culture was renewed and Mitomicyn C solution was added to final concentration of 10 μg/mL and incubated at 37 °C with 5% CO_2 incubator

for 4 hours. MEM with Mitomicyn C was removed and cells were washed with PBS for 3 times to remove excess Mitomicyn C. New MEM was added to the cells and cells were incubated for one day. Thereafter, cells were incubated in medium containing SiQD at concentrations from 12.5 µg/mL to 400 µg/mL, then cell viability was observed for 1, 7 and 14 days. Calculation of cell viability was done by using 3 absorbance values from same concentration. Absorption by SiQDs during the measurement was also considered and cell viability, CV, was calculated by using Equation 5:

$$CV\% = \frac{Abs_{(media+SiQD+HeLa)} - Abs_{(media+SiQD)}}{Abs_{(media+HeLa)} - Abs_{(media)}} \qquad 5.1$$

where Abs stands for absorbance value for indicated sample sets.

5.3. Results and discussion

Optical absorption and emission properties of UA:SiQD-water and UA:SiQD-MEM solutions were observed. Absorption due to color originated from phenol red of MEM which is essential to detect any contamination during cell culture experiments was presented in the spectra as well as appearance of a second peak in UV region (Figure 5.1a). PL spectra of both solutions show similar behavior (Figure 5..1b). UA:SiQD-MEM solution shows the characteristic of UA:SiQD-water solutions. Obtained PL peaks have Gaussian-like spectral shape positioned at 680 nm. Under 350 nm excitation, PLQY of UA:SiQD-water, UA:SiQD-MEM and only MEM is 22, 12 and 0.1%, respectively. Due to the low PLQY value of MEM, PL behaviour of UA:SiQD solutions shows characteristics of UA:SiQDs. Decrease in the PLQY for UA:SiQD-MEM solutions is due to the fact that the MEM absorbs the excitation light but it does not emit which is evidenced by its PLQY value. PLQY of SiQDs change also depending on size and surface functionalization. Undecanoic acid functionalized SiQDs were reported to have 3.6%,[10] other hydrophilic SiQDs vary from 7 to 10% PLQY[11, 12,13, 14] in aqueous media. Despite the decrease in PLQY caused by MEM, it was observed that the obtained PLQY value was higher than that in the literature.

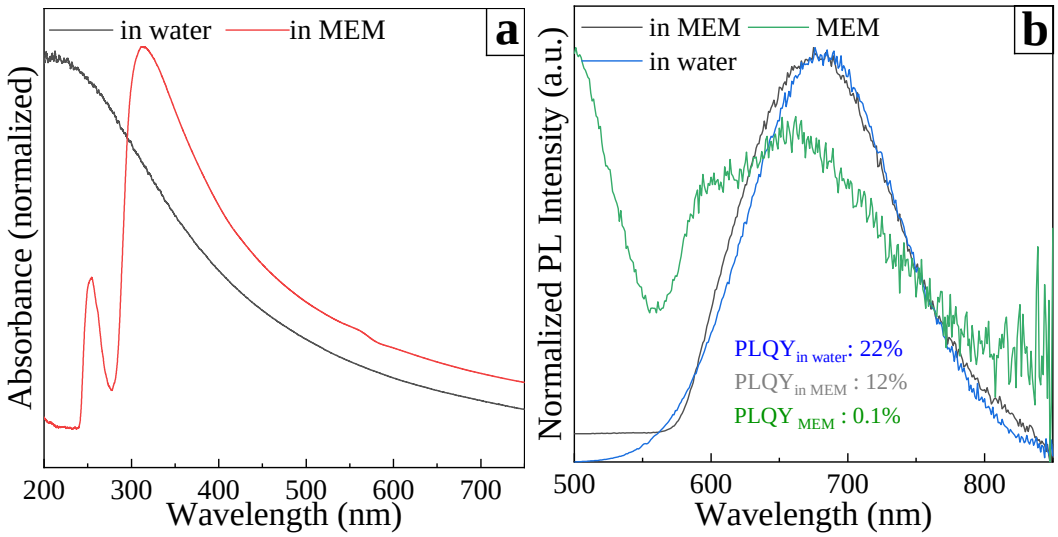

Figure 5.1. Optical characterization of UA:SiQDs; a) UV-visible absorption and b) PL spectra for the UA:SiQDs in water (in blue), in MEM (in grey) and MEM only (in green)

To observe the UA:SiQDs, cells were were excited at 405 nm and fluorescence at 600 to 700 nm was captured. DAPI staining studies enabled good quality bimodal imaging of HeLa cells. In Figure 5.2, nucleus of HeLa cells giving green fluorescence by DAPI implies that SiQDs are only distributed in the cytoplasm.

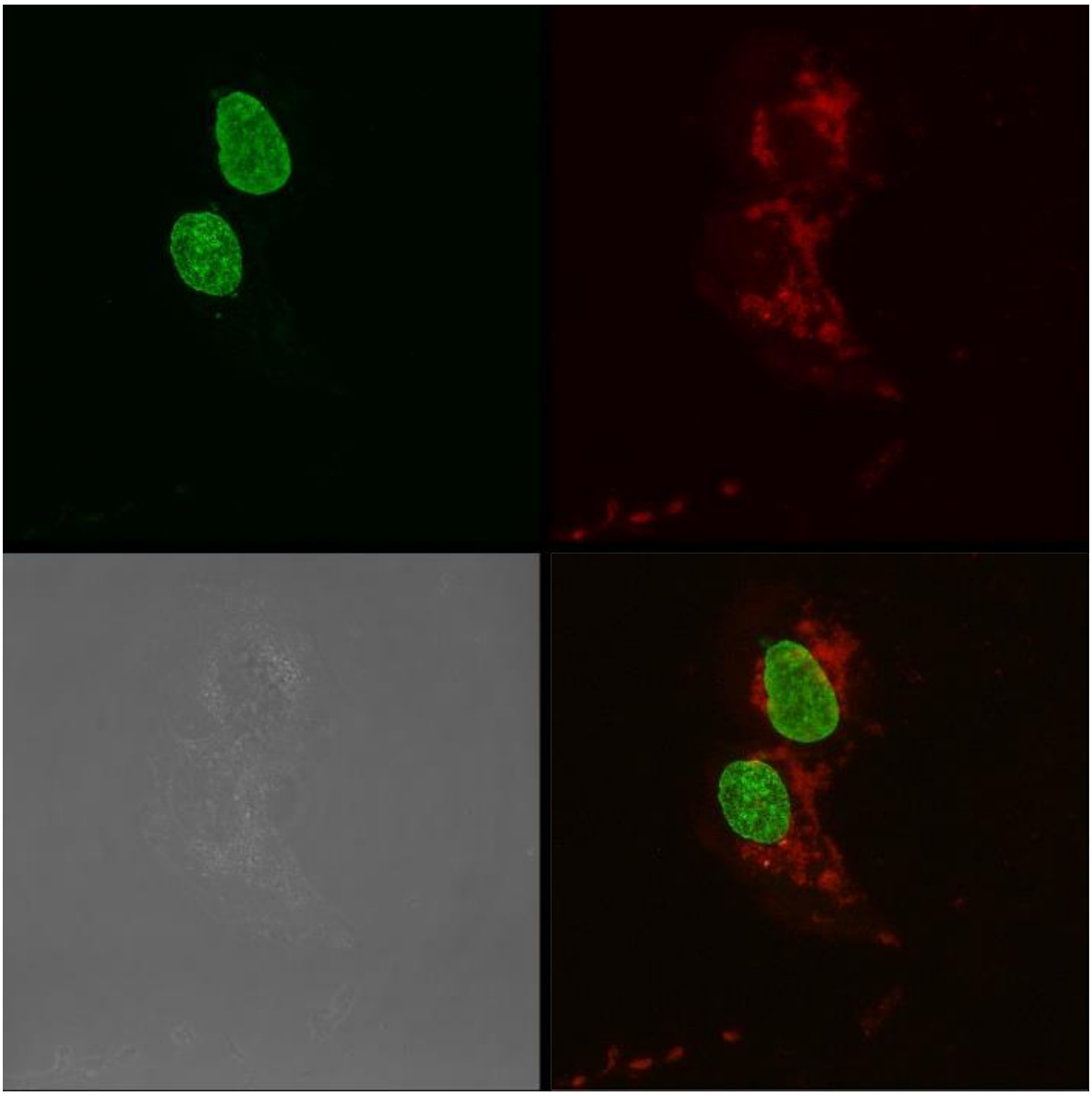

Figure 5.2. Confocal mıcroscopy images of UA:SiQDs together with DAPI staining

Temperature and concentration dependent uptake studies were performed to understand cellular uptake mechanism. In Figure 5.3, DIC and fluorescence images of HeLa cells incubated with SiQD solutions for 1 hour at room temperature and at 4 °C are shown. For both cases, cell uptake was observed in a similar manner. Comparision of uptake data at

low and regular temperatures provide elimination of cellular activities. Thus, it is shown that uptake of SiQDs is energy independent process.

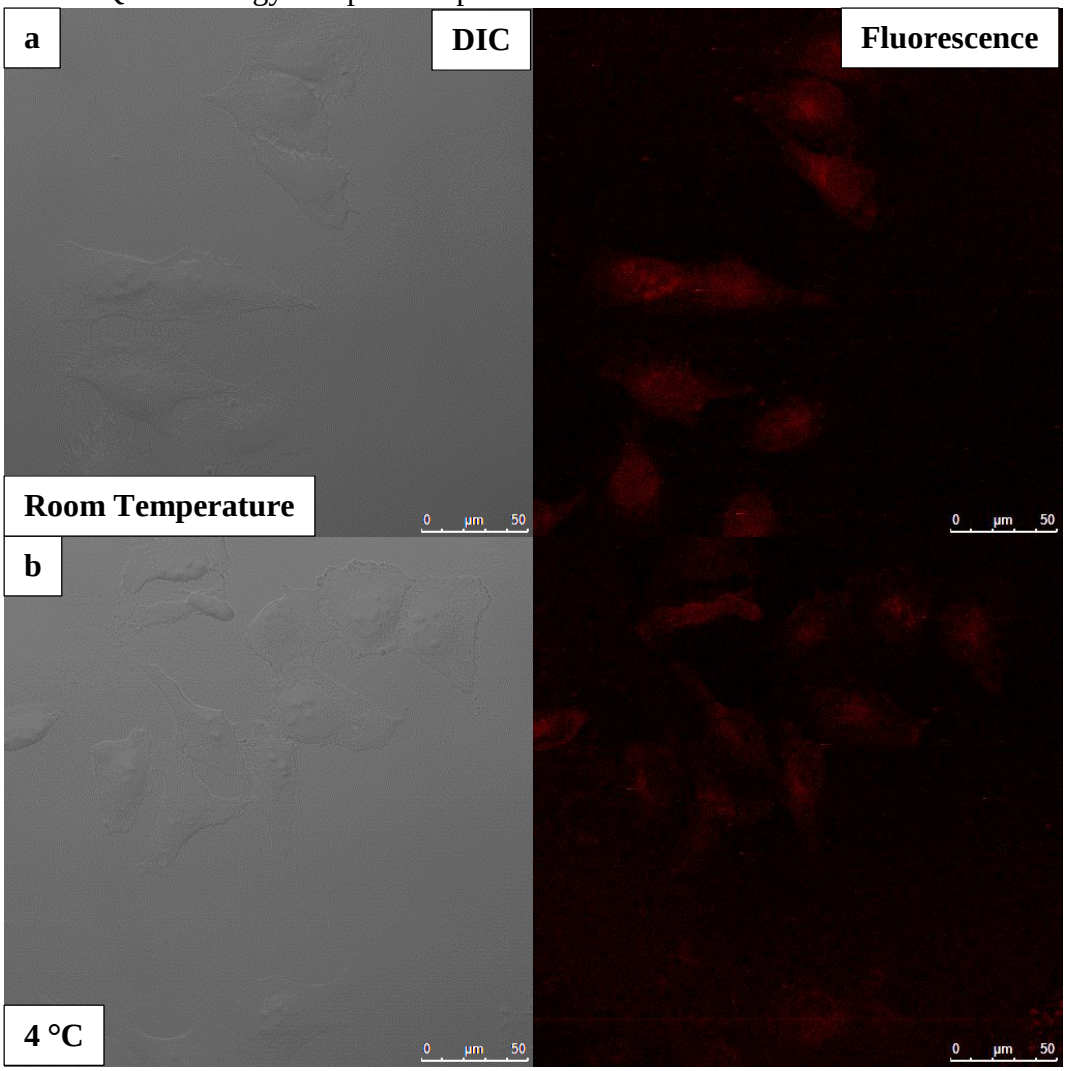

Figure 5.3. DIC and fluorescence images of HeLa cells incubated with SiQD solutions for 1 hour at a) room temperature and at b) 4 °C

Uptake of HeLa cells incubated for 1 hour at 37 °C in different concentrations of UA:SiQDs (Figure 5.4) has shown different fluorescence intensity. It is thought that energy independent uptake of the cells is provided by diffusion of SiQDs through the membranes of HeLa cells.

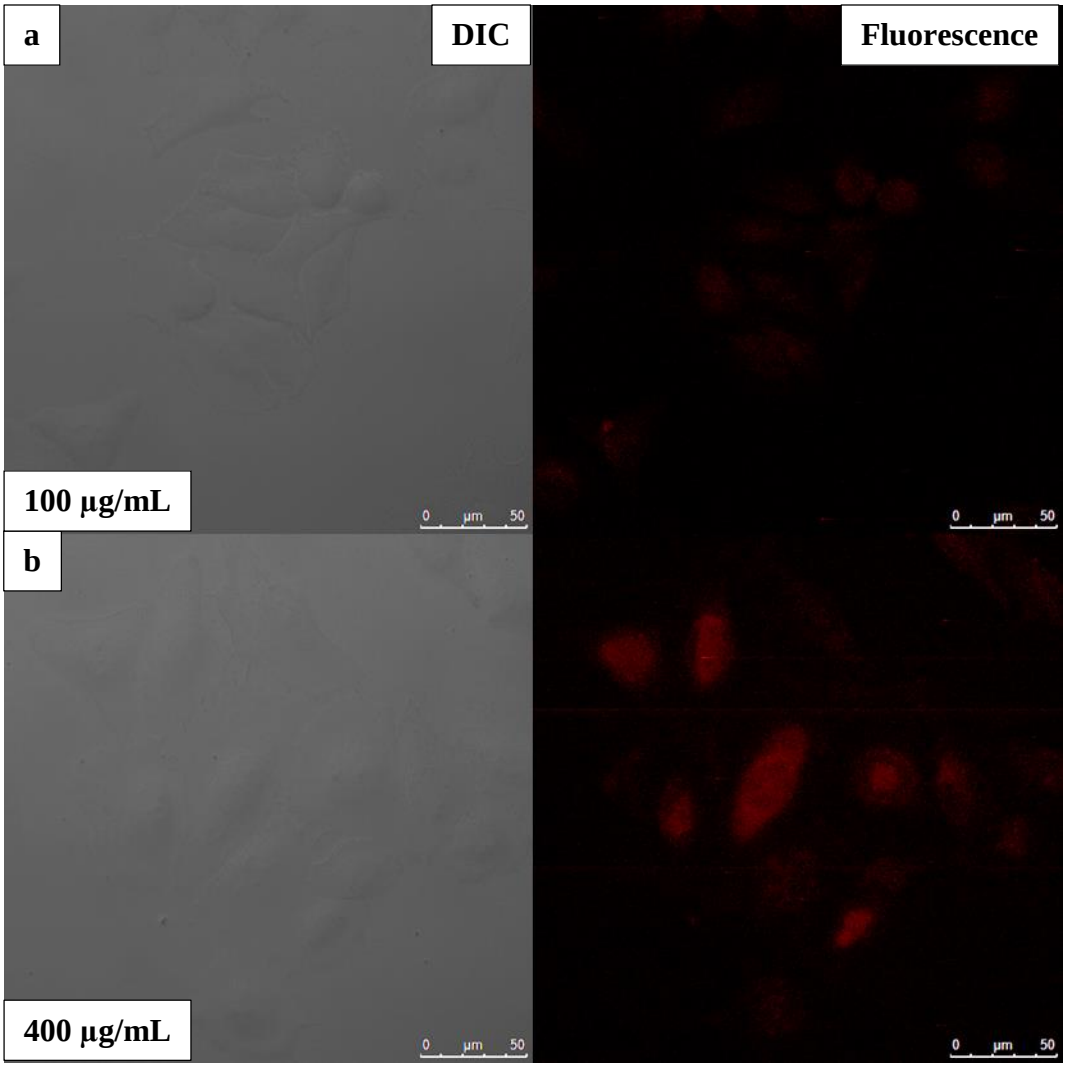

Figure 5.4. DIC and fluorescence images of HeLa cells incubated with SiQD solutions with a) 100 µg/mL and b) 400 µg/mL concentration

Figure 5.5 (a-c) shows differential interference contrast (DIC) and fluorescence images of HeLa cells with UA:SiQDs at 4 degrees at 1st, 5th and 18th days after uptake. UA:SiQDs could be observed even after 18 days that implies UA:SiQDs are photostable in cell media.

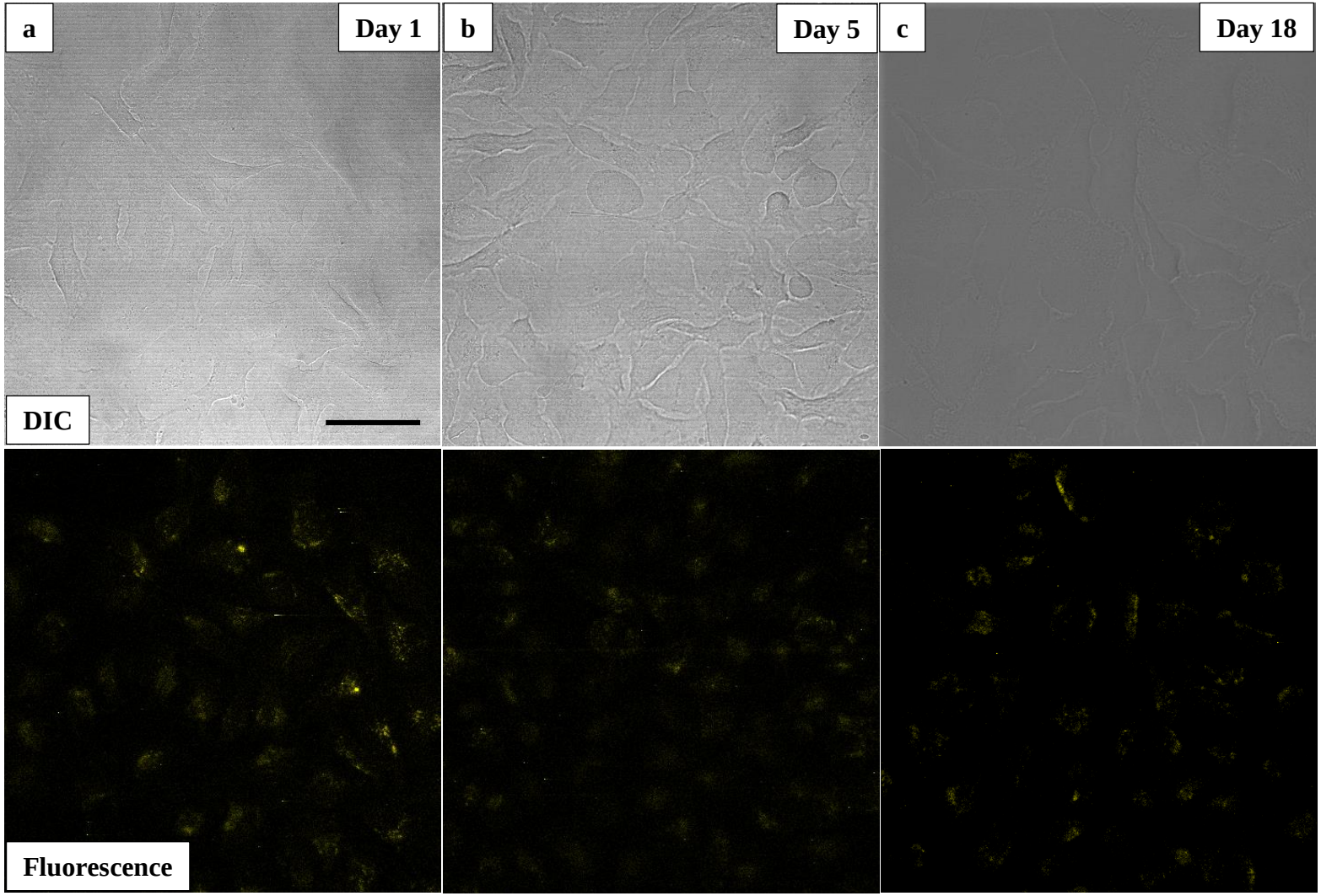

Figure 5.5. Confocal microscopy image of Hela cells treatd with UA:SiQDs in HeLa cells: DIC (left) and fluorescence (right) images of 1, 5 and 18 days after UA:SiQDs uptake. Scale bar is same and 50 μm for each image

The intensity of the excitation laser and the sensitivity of the detector was optimized to avoid the detection of autofluorescence signal of cells by performing fluorescence observation of Hela cells that did not uptake the UA:SiQDs as a control. As shown in Figure 5.6, Figure 5.7 and Figure 5.8, no autofluorescence was observed from the control cellsfor all studies.

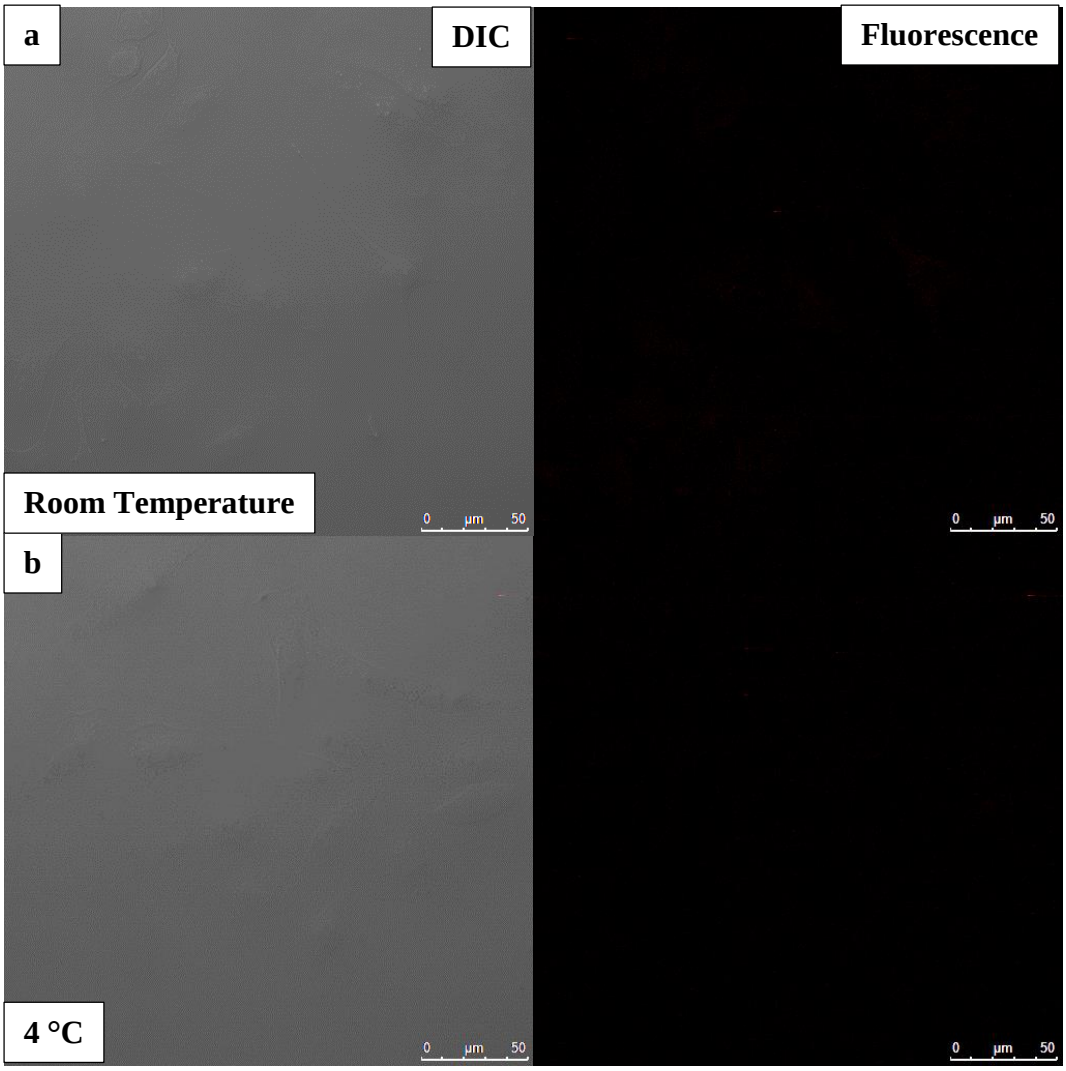

Figure 5.6. Confocal microscopy images of HeLa cells (control samples) incubated for 1 hour at a) room temperature and at b) 4 °C

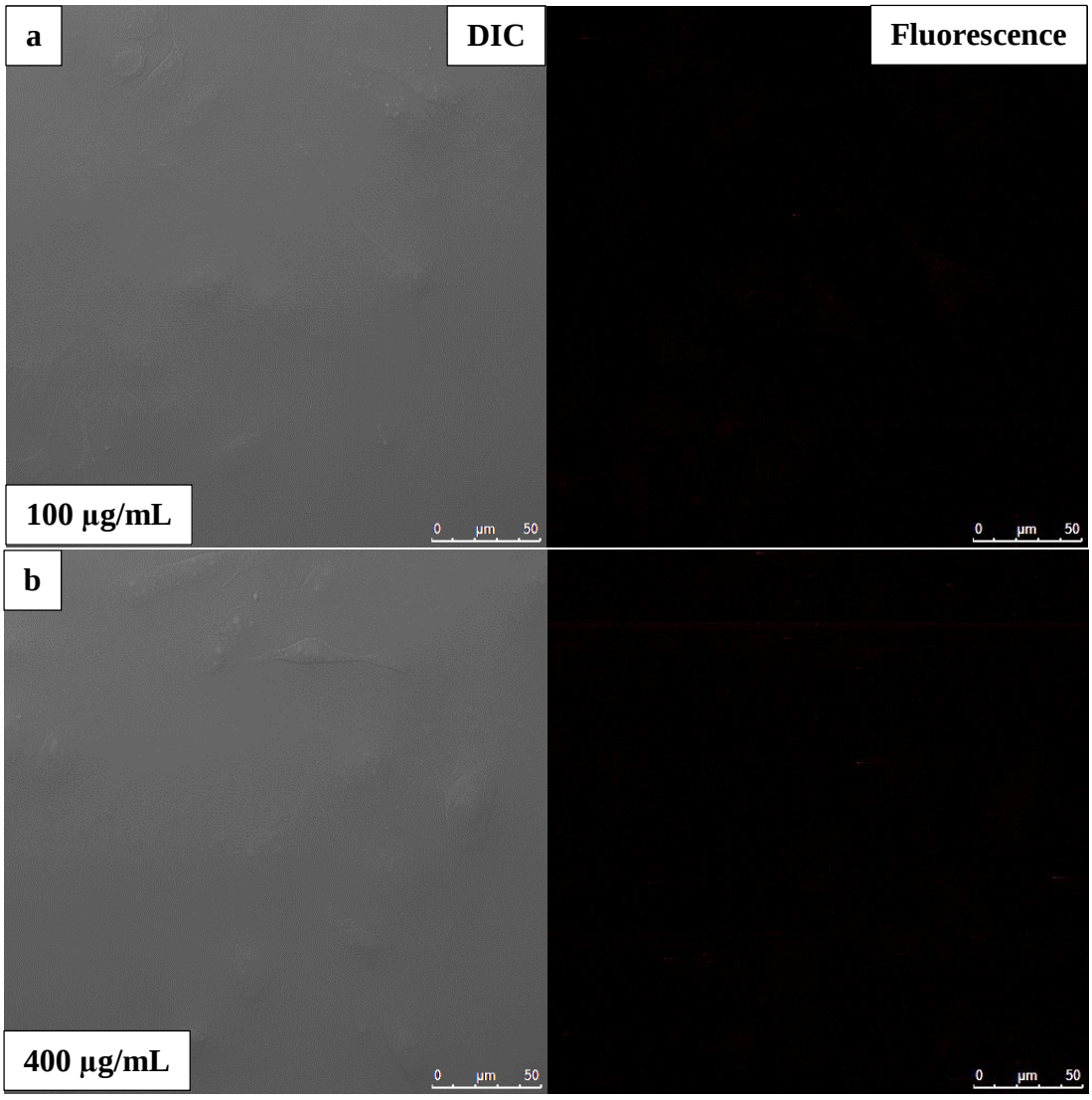

Figure 5.7. Confocal microscopy images of HeLa cells (control samples) incubated for 1 hour at 37 C with SiQDs having a) 100 and b) 400 µg/mL concentration

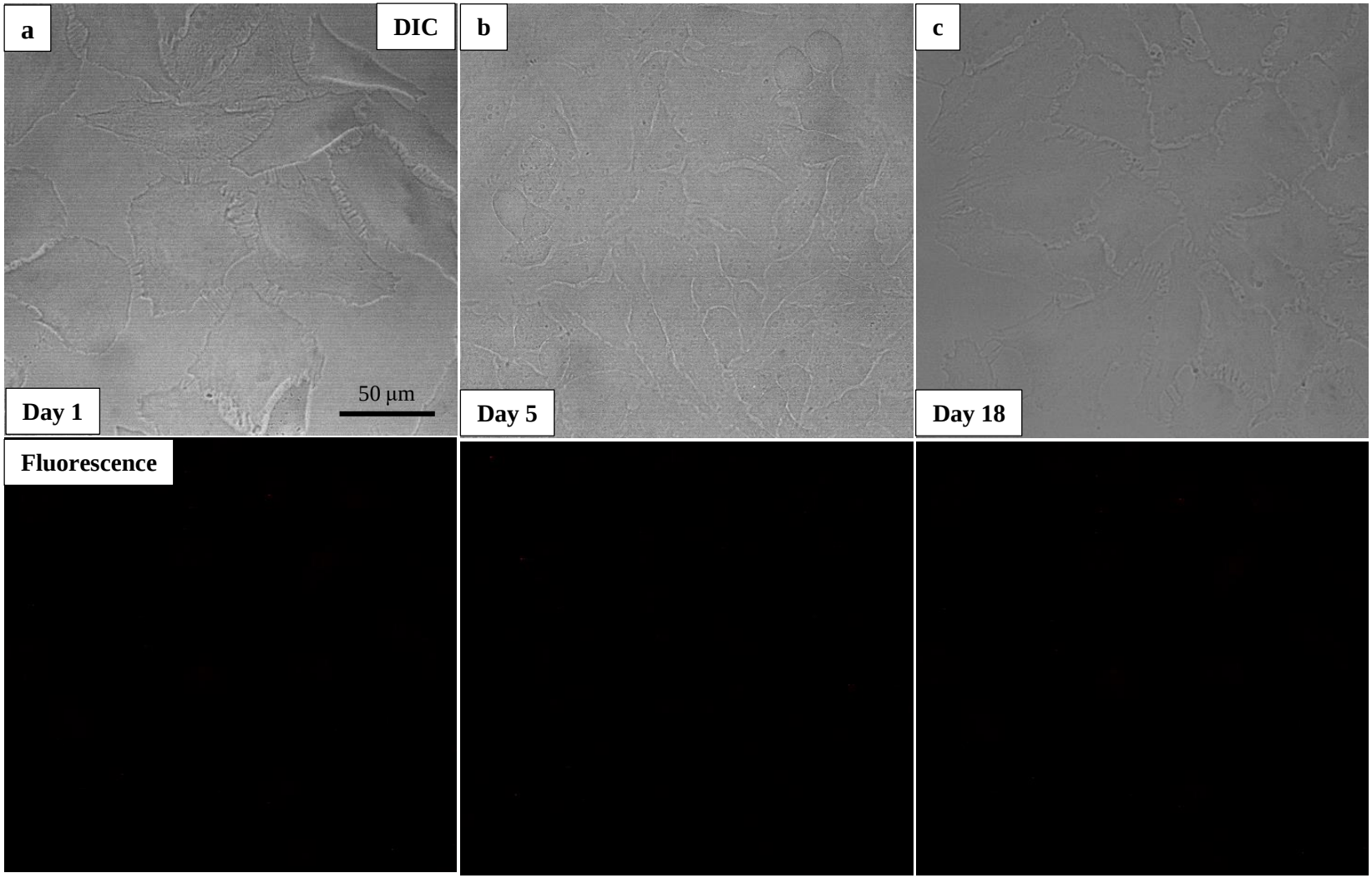

Figure 5.8. Control cells of time dependent photostability study at 1st, 5th and 18th day culture without UA:SiQDs treatment. Scale bar is same and 50 µm for each image

Hela cells incubated with UA:SiQDs show the bright fluorescence signal inside the cells (Figure 5.7). The UA:SiQDs appears to be vesicularly localized in the cell. There is no significant change in fluorescence emission and localization after 10 and also 18 days culture. Only difference is that cell morphology has changed for 18th day. This result is consistent with the similar works. Photostability of SiQDs with alkyl termination in CACO-2 cells has been previously reported.[15] Cells having alkyl SiQDs up to 50 μg/mL could still be detected after 14 days. Photostability of SiQDs could also be investigated by photobleaching studies.[16] It is comparatively shown that SiQDs are photostable after 120 minutes of exposure, intensity of SiQD in *C. elegans* digestive tract decreased no less than to its 85% while intensity of CdTe QDs decreased to 40%. Thus, SiQDs could be potential QDs for long term bioimaging due to their successful uptake properties and photostability.

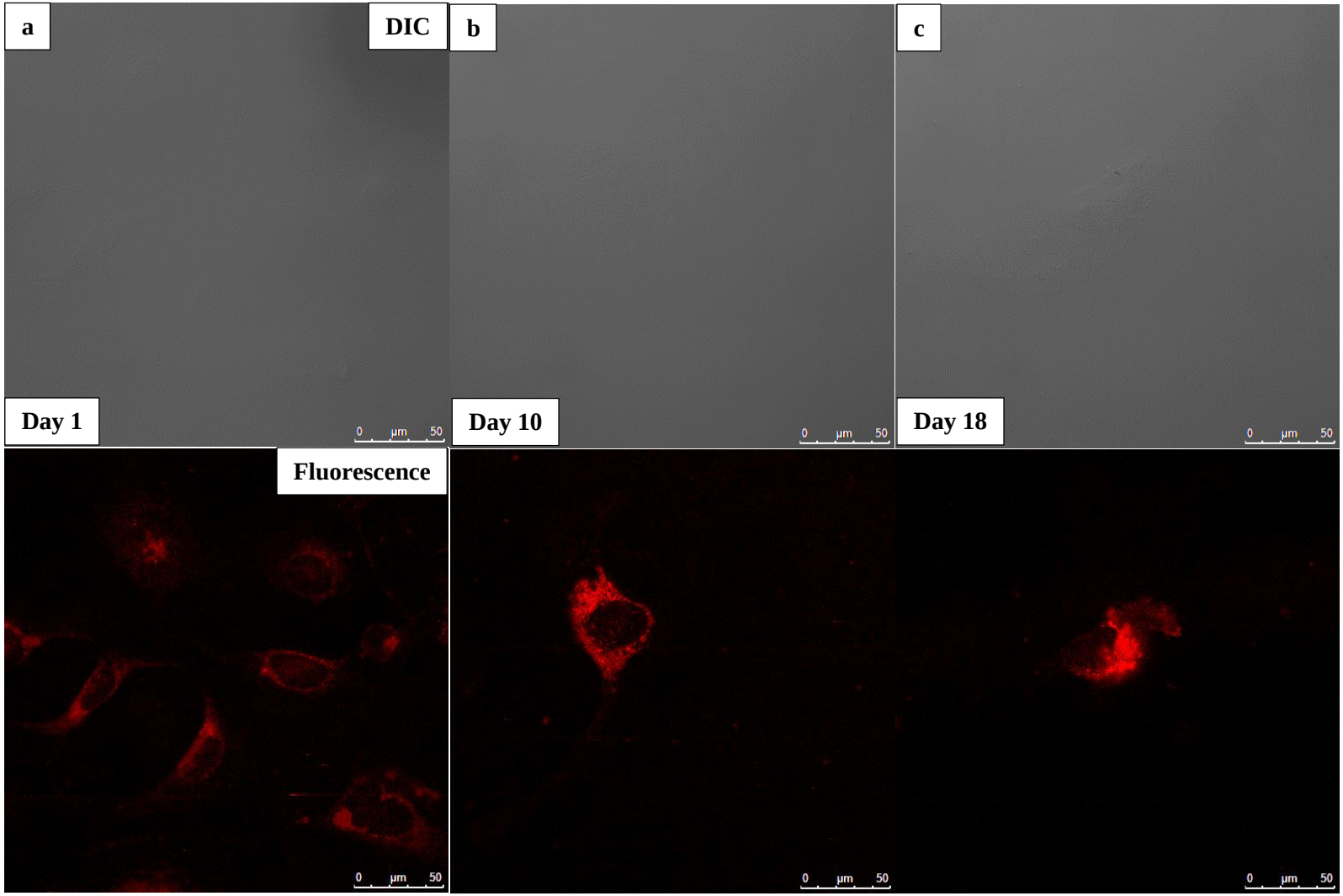

Figure 5.9. Time dependent uptake and photostability of UA:SiQDs in HeLa cells as a) 1st, b) 10th and c) 18th day

Concentration of QDs that interact with cells without causing toxicity is also crucial for bioapplications. High concentrations may allow us to make efficient bioimaging as well as the photothermal heating. Thus, we investigated short term and long term cytotoxicity of UA:SiQDs to HeLa cells. UA:SiQDs show no cytotoxic effect at concentration from 25 to 400 µg/mL after 24 hours of incubation. Carboxylic acid functionalized SiQDs with similar size to this study was reported to be non-toxic for CACO-2 cells up to 100 µg/mL.[17] Si nanostructures with hundreds of nanometer size were reported to show no toxicity up to 200 µg/mL.[1, 18, 19] Also, in a comparative study, it is reported that Cd containing QDs have shown toxic effects even at 1 µg/mL concentration[20]. Figure 5.8b shows long term toxic effect of SiQDs in Hela cells. Long-term exposure of cells to nanoparticles can induce cytotoxicity, however 50% viability was obtained even after 14 days exposure to 50 µg/mL of UA:SiQDs.

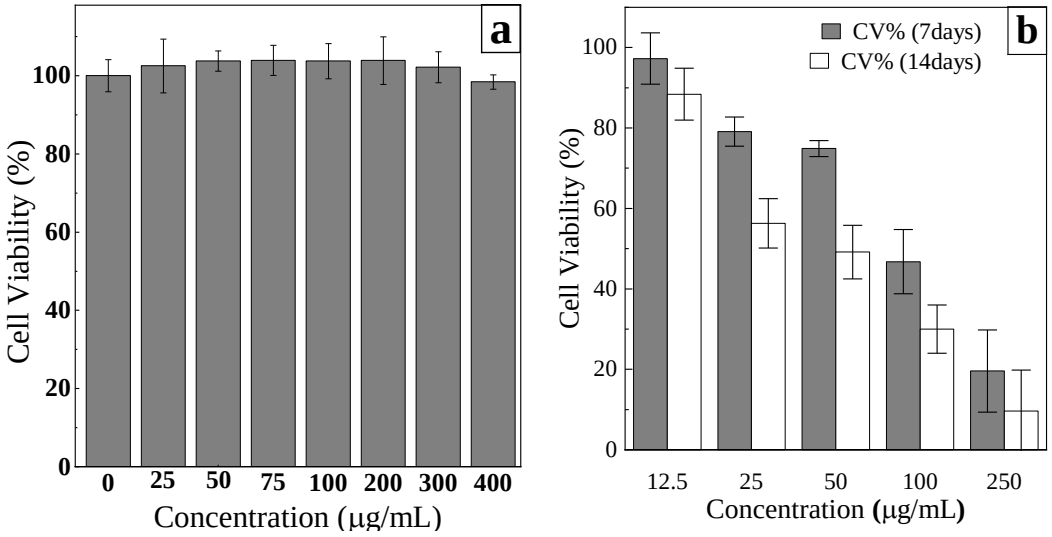

Figure 5.10. Cell viability of Hela cells treated with various concentration of UA: SiQDs for a) 1 day, b) 7 and 14 days. Data represent mean +/- SD (n=6)

5.4. Conclusions

In this chapter, synthesized water soluble SiQDs were investigated by means of cell uptake and long term stability. Successful uptake by HeLa cells was achieved. In HeLa cells, SiQDs remained stable up to at least 18 days Synthesized SiQDs showed no acute toxicity up to 400 ug/mL and 50% cell viability after 7 days at 100 ug/mL. Both findings imply the use of SiQDs as long term bioimaging agents.

5.5. References

(1) Scheres, L.; Rijksen, B.; Giesbers, M.; Zuilhof, H. Molecular Modeling of Alkyl and Alkenyl Monolayers on Hydrogen-Terminated Si(111). *Langmuir* **2011**, *27* (3), 972-980. DOI: 10.1021/la104705b.

(2) Niaz, S.; Zdetsis, A. D. Comprehensive Ab Initio Study of Electronic, Optical, and Cohesive Properties of Silicon Quantum Dots of Various Morphologies and Sizes up to Infinity. *The Journal of Physical Chemistry C* **2016**, *120* (20), 11288-11298. DOI: 10.1021/acs.jpcc.6b02955.

(3) Phatvej, W.; Datta, H. K.; Wilkinson, S. C.; Mutch, E.; Daly, A. K.; Horrocks, B. R. Endocytosis and Lack of Cytotoxicity of Alkyl-Capped Silicon Quantum Dots Prepared from Porous Silicon. *Materials (Basel)* **2019**, *12* (10), 1702. DOI: 10.3390/ma12101702 PubMed.

(4) Cheng, Y.; Sun, C.; Ou, X.; Liu, B.; Lou, X.; Xia, F. Dual-targeted peptide-conjugated multifunctional fluorescent probe with AIEgen for efficient nucleus-specific imaging and long-term tracing of cancer cells. *Chemical Science* **2017**, *8* (6), 4571-4578, 10.1039/C7SC00402H. DOI: 10.1039/C7SC00402H.

(5) Weissleder, R.; Pittet, M. J. Imaging in the era of molecular oncology. *Nature* **2008**, *452* (7187), 580-589. DOI: 10.1038/nature06917.

(6) Wang, Z.; Yong, T.-Y.; Wan, J.; Li, Z.-H.; Zhao, H.; Zhao, Y.; Gan, L.; Yang, X.-L.; Xu, H.-B.; Zhang, C. Temperature-Sensitive Fluorescent Organic Nanoparticles with Aggregation-Induced Emission for Long-Term Cellular Tracing. *ACS Applied Materials & Interfaces* **2015**, *7* (5), 3420-3425. DOI: 10.1021/am509161y.

(7) Wang, J.; Liu, Y.; Peng, F.; Chen, C.; He, Y.; Ma, H.; Cao, L.; Sun, S. A General Route to Efficient Functionalization of Silicon Quantum Dots for High-Performance Fluorescent Probes. *Small* **2012**, *8* (15), 2430-2435. DOI: https://doi.org/10.1002/smll.201102627.

(8) Zhong, Y.; Sun, X.; Wang, S.; Peng, F.; Bao, F.; Su, Y.; Li, Y.; Lee, S.-T.; He, Y. Facile, Large-Quantity Synthesis of Stable, Tunable-Color Silicon Nanoparticles and Their Application for Long-Term Cellular Imaging. *ACS Nano* **2015**, *9* (6), 5958-5967. DOI: 10.1021/acsnano.5b00683.

(9) Zhong, Y.; Peng, F.; Bao, F.; Wang, S.; Ji, X.; Yang, L.; Su, Y.; Lee, S.-T.; He, Y. Large-Scale Aqueous Synthesis of Fluorescent and Biocompatible Silicon Nanoparticles and Their Use as Highly Photostable Biological Probes. *Journal of the American Chemical Society* **2013**, *135* (22), 8350-8356. DOI: 10.1021/ja4026227.

(10) Clark, R. J.; Dang, M. K. M.; Veinot, J. G. C. Exploration of Organic Acid Chain Length on Water-Soluble Silicon Quantum Dot Surfaces. *Langmuir* **2010**, *26* (19), 15657-15664. DOI: 10.1021/la102983c.

(11) Yu, Y.; Hessel, C. M.; Bogart, T. D.; Panthani, M. G.; Rasch, M. R.; Korgel, B. A. Room Temperature Hydrosilylation of Silicon Nanocrystals with Bifunctional Terminal Alkenes. *Langmuir* **2013**, *29* (5), 1533-1540. DOI: 10.1021/la304874y.

(12) Hessel, C. M.; Rasch, M. R.; Hueso, J. L.; Goodfellow, B. W.; Akhavan, V. A.; Puvanakrishnan, P.; Tunnel, J. W.; Korgel, B. A. Alkyl passivation and amphiphilic polymer coating of silicon nanocrystals for diagnostic imaging. *Small (Weinheim an der Bergstrasse, Germany)* **2010**, *6* (18), 2026-2034. DOI: 10.1002/smll.201000825 From NLM.

(13) Warner, J. H.; Hoshino, A.; Yamamoto, K.; Tilley, R. D. Water-Soluble Photoluminescent Silicon Quantum Dots. *Angewandte Chemie International Edition* **2005**, *44* (29), 4550-4554. DOI: https://doi.org/10.1002/anie.200501256.

(14) Sato, S.; Swihart, M. T. Propionic-Acid-Terminated Silicon Nanoparticles: Synthesis and Optical Characterization. *Chemistry of Materials* **2006**, *18* (17), 4083-4088. DOI: 10.1021/cm060750t.

(15) Phatvej, W.; Datta, H. K.; Wilkinson, S. C.; Mutch, E.; Daly, A. K.; Horrocks, B. R. Endocytosis and Lack of Cytotoxicity of Alkyl-Capped Silicon Quantum Dots Prepared from Porous Silicon. *Materials (Basel, Switzerland)* **2019**, *12* (10). DOI: 10.3390/ma12101702 From NLM.

(16) Zhou, Y.; Zhang, Y.; Zhong, Y.; Fu, R.; Wu, S.; Wang, Q.; Wang, H.; Su, Y.; Zhang, H.; He, Y. The in vivo targeted molecular imaging of fluorescent silicon nanoparticles in Caenorhabditis elegans. *Nano Research* **2018**, *11* (5), 2336-2346. DOI: 10.1007/s12274-017-1677-1.

(17) Bhattacharjee, S.; Rietjens, I. M. C. M.; Singh, M. P.; Atkins, T. M.; Purkait, T. K.; Xu, Z.; Regli, S.; Shukaliak, A.; Clark, R. J.; Mitchell, B. S.; et al. Cytotoxicity of surface-functionalized silicon and germanium nanoparticles: the dominant role of surface charges. *Nanoscale* **2013**, *5* (11), 4870-4883, 10.1039/C3NR34266B. DOI: 10.1039/C3NR34266B.

(18) Hanada, S.; Fujioka, K.; Futamura, Y.; Manabe, N.; Hoshino, A.; Yamamoto, K. Evaluation of Anti-Inflammatory Drug-Conjugated Silicon Quantum Dots: Their Cytotoxicity and Biological Effect. *International Journal of Molecular Sciences* **2013**, *14* (1), 1323-1334.

(19) Ahire, J. H.; Wang, Q.; Coxon, P. R.; Malhotra, G.; Brydson, R.; Chen, R.; Chao, Y. Highly Luminescent and Nontoxic Amine-Capped Nanoparticles from Porous Silicon: Synthesis and Their Use in Biomedical Imaging. *ACS Applied Materials & Interfaces* **2012**, *4* (6), 3285-3292. DOI: 10.1021/am300642m.

(20) Erogbogbo, F.; Yong, K.-T.; Roy, I.; Hu, R.; Law, W.-C.; Zhao, W.; Ding, H.; Wu, F.; Kumar, R.; Swihart, M. T.; et al. In Vivo Targeted Cancer Imaging, Sentinel Lymph Node Mapping and Multi-Channel Imaging with Biocompatible Silicon Nanocrystals. *ACS Nano* **2011**, *5* (1), 413-423. DOI: 10.1021/nn1018945.

Chapter 6: Summary, Conclusions and Future Prospects

6.1. Summary

In this thesis, the main aim is to investigate SiQDs as a low toxic alternative to theranostics field. For this aim, stable, water soluble SiQDs were prepared with undecanoic acid termination (UA:SiQDs). Their performance as bioimaging agents were investigated by confocal microscopy and cytotoxicity tests. Long term cytotoxicity and photostability of UA:SiQDs were observed in cell media for the first time. Besides, photothermal response of SiQDs were detailly analyzed. Heating by photothermal effect was observed via Raman spectroscopy of bare SiQDs at three different sized under 5 nm. Reason for photothermal heating was investigated by temperature dependent PL spectroscopy in order to uncover the nonradiative incidents in the structure. Photothermal effect of UA:SiQDs were also investigated in aqueous media. To reveal the employability of photothermal effect of SiQDs to kill the living cells, in-vitro irradiation representing photothermal therapy was demonstrated.

6.2. Conclusions

- ➔ Synthesis of water soluble SiQDs that can be used for bioapplications was achieved by hydrosilylation with 10-undecenoic acid. It was seen that synthesized SiQDs are stable even at 37 °C for 15 days. 20% PLQY (in water) of SiQDs was achieved by optimization of Si-H forming and hydrosilylation parameters.
- ➔ Photothermal effect of SiQDs and photothermal heating mechanism was investigated by using H:SiQDs. Size depended photothermal heating by changing laser power was observed by Raman spectroscopy. It was seen that higher photothermal heating is provided by large particle size. The reason for such behavior was investigated by temperature depended PL spectroscopy. Increasing density of defect states with increasing size was considered as the reason for photothermal heating. Also, with enhanced heat dissipation, larger particles could be heated without damage up to higher temperatures.

- ➔ Photothermal response of UA:SiQDs in water was investigated. Size depended heating could be observed in a similar way with H:SiQDs. Calculated photothermal conversion efficiency was found to be comparable with the other candidate materials that could be used for photothermal therapy.
- ➔ Demonstration of photothermal therapy was carried out by using 532 nm laser which corresponds to 1064 nm when two-photon imaging is used. Cell death was observed SiQD with the concentration dependency.
- ➔ Bioimaging performance of SiQDs was detailly evaluated. Successful uptake was achieved for HeLa cells and imaging was observed to be possible even after 18 days. Mechanism of uptake is thought to be a diffusion based process. Cytotoxicity studies also showed low toxicity up to 14 days. It is concluded that SiQDs have potential use for long term bioimaging applications.
- ➔ Since low toxicity is a very important requirement for target application area, cytotoxicity of SiQDs to HeLa cells was investigated by concentration depended short and long term cytotoxicity investigations. It was seen that SiQDs show no toxicity for the first day. Long term cytotoxic effects are promising yet different than uppermost cytotoxicity results. In the long term use, concentration could be used for limited concentration like 50 μg/mL, which is still higher than most part of the reported counterparts.
- ➔ SiQDs would emerge as theranostic platform that enables fluorescent imaging and photothermal nanotherapy. With the relatively high PLQY values, SiQDs could be good biomarkers. Taming the photothermal response of SiQDs would allow us to provide very localized heating, thus, photothermal heating.

6.3. Future Prospects

With this thesis, very promising results implicating the theranostic use of SiQDs with good PLQY, photostability and low toxicity was achieved. Whereas, there should be future studies for their realization as theranostic agents:

- Obtained results for fluorescent imaging and photothermal heating is provided by irradiation with UV and visible laser. This may not be suitable for practical use. Therefore, their performance should be evaluated by the techniques with two-photon irradiation.
- Surface bioconjugation of SiQDs to gain targetability should be investigated.
- The use of photothermal SiQDs for other applications should be considered. For instance, using SiQDs as adjuvants by corresponding from their high surface to volume ratio may improve the efficiency of vaccines required for various diseases and allergies.

ACKNOWLEDGEMENTS

My PhD journey was so different than I imagined. I had many ups and downs, struggles, victories and failures. I learnt to deal with problems together with unexpected surprises of life, that being said, this work is not just a PhD but also representing to explore myself, my strengths, vulnerabilities. Thankfully, I was not alone.

I would like to thank to my supervisor, Dr. Naoto SHIRAHATA for his guidance for every aspect of my stay in Japan. He supervised me in a way that I can freely express myself, learn and also make my work-life balance in the most respectful and kindest way. Also, I would like to thank to my co-supervisors, Dr. Jinhua Ye and Dr. Tetsuo UCHIKOSHI for their continuous support.

I would like to thank to our collaborators Dr. Batu GHOSH, Dr. Tomohiko YAMAZAKI, Dr. Shanmugavel CHINNATHAMBI and Dr. Hong-Tao SUN. I would like to thank to all staff in Nano-bio Group Facility for enabling me to learn new techniques and making me not feel like a stranger in a completely different laboratory.

In a non-stop working laboratory, it is a big task to provide environment that help us work comfortably. In this respect, I would like to thank to Fumie TAKAZAWA for her efforts she put in our laboratory together with sharing everything she knows neatly and unassumingly.

I would like to thank to my colleagues, namely, Hiroyuki YAMADA, Kazuhiro NEMOTO, Junpei WATANABE, Huang XIAYOU, Subashri CHATTERJEE, Binbin ZHANG, Jiakai CHEN, for their support during my PhD work and accompanying.

Living in a country without understanding the language and procedures could be much more difficult if I didn't have the help from Keiko NISHIKAWA (JISTEC), Yuko YAMAGUCHI, Soga MASAMI and Eiko YOKOTA. Also, it would be a lot more difficult if I didn't meet with kind people. I would like to thank to Dr. Tohru SUZUKI, Dr. Tran Thi Hoai GIANG, Dr. Pelin TOZMAN KARANIKOLAS, Dr. Vasileios KARANIKOLAS, Dr. Esmaeil ADABIFIROOZJAEI, Dr. Esmail DOUSTKHAH, and all friends for their support.

I would like to thank to my family in Turkey for their emotional support.

Finally, I would like to thank to my husband, Dr. Cem Eren ÖZBİLGİN. the reason I came to Japan and the one who gave me all happiness I have in my life, who makes me forget all my sadness with his endless love. Not to forget my son, Atlas, for making even the simplest moments fun for us and teaching me how to be curious and unprejudiced.